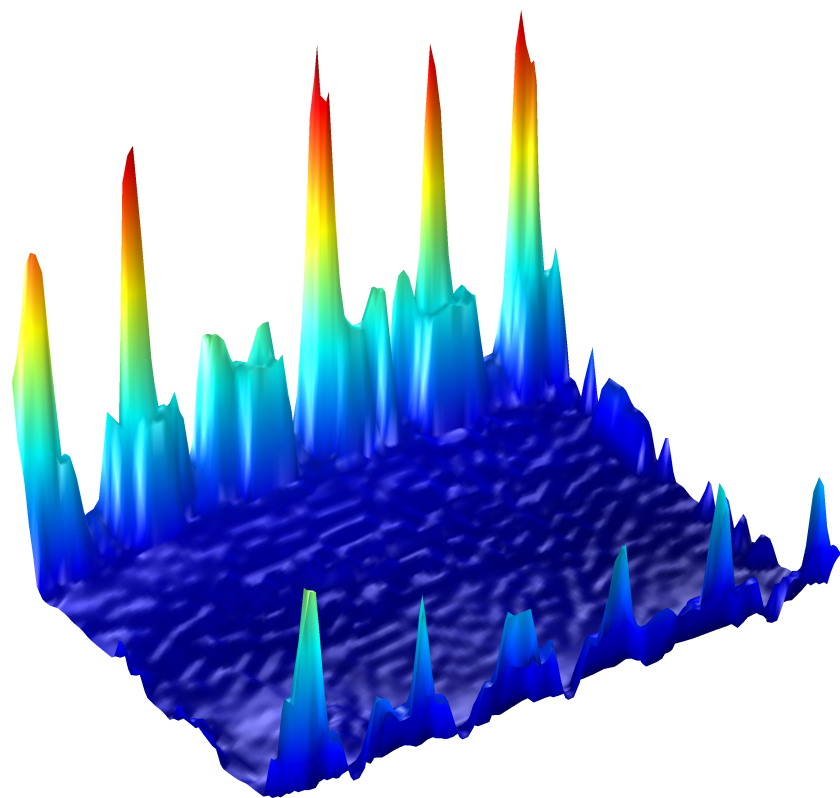


## Department of Precision and Microsystems Engineering

### A Practical Application of Topology Optimization for Heat Transfer and Fluid Dynamics

T.C. Scholten

Report number : EM 2017.014  
Coaches : Ir. M. van der Kolk , Ir. D. Braaksma  
Professor : Dr.ir. M. Langelaar  
Specialisation : Engineering mechanics  
Type of report : Master thesis  
Date : 27-02-2017





# **A PRACTICAL APPLICATION OF TOPOLOGY OPTIMIZATION FOR HEAT TRANSFER AND FLUID DYNAMICS**

## **Master Thesis**

by

**Thomas C. SCHOLTEN**

to obtain the degree of Master of Science  
at the Delft University of Technology,  
to be defended publicly on Monday February 27, 2017 at 13:45.

Student number: 4318331  
Project duration: February 8, 2016 – February 27, 2017  
Thesis committee: Dr. ir. M. Langelaar, TU Delft  
Dr. ir. R.A.J. van Ostayen, TU Delft  
Ir. M. van der Kolk, TU Delft  
Ir. D. Braaksma, ASML

An electronic version of this thesis is available at <http://repository.tudelft.nl/>.



# CONTENTS

|  |            |
|--|------------|
| <b>Summary</b>   | <b>v</b>   |
| <b>Preface</b>   | <b>vii</b> |
| <b>1 Introduction</b>  | <b>1</b>   |
| 1.1 Outline of thesis . . . . .                                    | 3          |
| <b>2 Lean E-box</b>  | <b>5</b>   |
| 2.1 Printed Circuits Assemblies in the E-box . . . . .             | 5          |
| 2.2 Stages Satellite Board . . . . .                               | 6          |
| 2.3 Lean E-box concept . . . . .                                   | 9          |
| 2.4 Specifications . . . . .                                       | 9          |
| 2.5 Concept Design . . . . .                                       | 10         |
| 2.6 Finite Element Model . . . . .                                 | 11         |
| 2.7 Results . . . . .  | 12         |
| 2.8 Prototype design . . . . .                                     | 14         |
| 2.9 Conclusion . . . . .   | 15         |
| <b>3 Measurements</b>  | <b>17</b>  |
| 3.1 Temperature . . . . .  | 17         |
| 3.2 Conclusion . . . . .   | 20         |
| <b>4 Topology optimization of heat transfer and fluid dynamics</b> | <b>25</b>  |
| 4.1 Fluid dynamics . . . . .                                       | 25         |
| 4.2 Heat transfer . . . . .  | 26         |
| 4.3 Literature review . . . . .                                    | 26         |
| 4.4 Topology optimization . . . . .                                | 28         |
| 4.5 Uniform heat load . . . . .                                    | 29         |
| 4.6 Non uniform heat load . . . . .                                | 35         |
| 4.7 Conclusion . . . . .   | 37         |
| <b>5 Topology optimization of the design load</b>                  | <b>39</b>  |
| 5.1 Setting up the optimization . . . . .                          | 39         |
| 5.2 Topology optimization . . . . .                                | 40         |
| 5.3 Variation of the water inlet and outlet . . . . .              | 43         |
| 5.4 The prototype and performance measurements . . . . .           | 43         |
| 5.5 The influence of the stokes flow assumption . . . . .          | 45         |
| 5.6 Conclusion . . . . .   | 48         |
| <b>6 Conclusion</b>  | <b>51</b>  |
| 6.1 Recommendations . . . . .                                      | 51         |
| <b>Bibliography</b>  | <b>54</b>  |
| <b>A Components</b>  | <b>55</b>  |
| <b>B Junction Resistance</b>                                       | <b>57</b>  |
| B.1 Implementation in the FEM model . . . . .                      | 57         |
| <b>C Design decisions of the lean E-box</b>                        | <b>59</b>  |
| <b>D Thermal contact model</b>                                     | <b>65</b>  |
| <b>E Measurements</b>  | <b>69</b>  |
| E.1 Power dissipation before potting . . . . .                     | 69         |

|          |  |           |
|----------|--|-----------|
| E.2      | Surface flatness before potting . . . . .            | 71        |
| E.3      | Power dissipation after potting . . . . .            | 72        |
| E.4      | Surface flatness after potting . . . . .             | 73        |
| <b>F</b> | <b>Sensitivity analysis</b>                          | <b>75</b> |
| <b>G</b> | <b>PDE filter</b>                                    | <b>77</b> |
| <b>H</b> | <b>Topology optimization of the vacuum load case</b> | <b>79</b> |

# SUMMARY

The vacuum environment of the most advanced lithography machines are no ideal circumstances for heat dissipation components. Active cooling elements are required since natural convection is excluded. One category of heat dissipation components are electronic circuit boards. In the current state of the art machine from ASML, some of the electronic boards are placed in a sealed box and cooled by means of an air flow. The air flow inside the vacuum environment induces a rather big load case, which results in a large and heavy box. This is the backbone of creating a new concept for the cooling of these electronics; the lean E-box. For which the cooling is solved without an airflow. Thereby resolving the big load case.

The lean E-box uses a conductive heat transfer from the electrical components to a water cooled plate. The conductive heat transfer is achieved by encapsulating the circuit board by a thermal conductive epoxy. A conceptual design of the lean E-box is created for the SSB, which is one of the circuits boards from the ASML machine. In this work a design is presented that applies the lean E-box concept such that all component temperatures are within the specification. The thermal behavior is predicted with a Finite Element analysis and verified by experimental measurements. From the analysis and the measurements the conclusion is made that the presented concept is feasible.

The heat load from the electronics board that reaches the cool plate is highly non uniform. For such a non uniform heat load an optimal layout of the cooling channels exist, such that the cooling is optimized. In this work topology optimization is applied to find an optimized cooling channel layout. This is done by applying a topology optimization on the fluid dynamics and the heat transfer physics that govern the thermal behavior of the lean E-box. Topology optimization is widely used in academic environments and mostly applied for arbitrary load cases. This research shows that it is also possible to apply such an optimization for an industrial design case. First an arbitrary load is optimized using different formulations of the optimization problem, a comment is given on the numerical difference. Next the optimization is applied to the lean E-box design load. Different designs are presented that use different positions of the water inlet and outlet, a comment is given on the performances of these designs.

The influence of the assumptions made in the flow equation are discussed. This is done by comparing the velocity field of the same design but using various flow equations. From the comparison the conclusion is made that the assumption on the thickness made in the two-dimensional model has the largest influence. Because of this assumption, more detailed models in two-dimensions show less accurate results.

An attempt is made to measure the performance increase by the optimized design with respect to the baseline design. The performance increase was however so small that it was not seen in the measurements.



# PREFACE

*"Everything must be made as simple as possible. But not simpler"*

— Albert Einstein

This quote by Albert Einstein describes perfectly what I have tried to do in thesis. Describing a year's worth of work in a 50 page thesis was not easy. Therefore it was necessary to describe every aspect as simple and as brief as possible, without losing valuable information.

I would like to thank ASML and the TU Delft for giving me the opportunity to do the research as part of my graduation project. My research topic was very diverse; including a design aspect, a prototyping and testing aspect and finally a topology optimization and verification part. For me it contained the perfect ratio of practical engineering and more theoretical research.

My gratitude goes to my daily supervisors; Dave Braaksma on behalf of ASML and Max van der Kolk on behalf of the TU Delft. Next to this I would like to thank Matthijs Langelaar for the feedback and useful insights. I would also like to thank all the colleagues at ASML that aided me with the design and the prototype.

*Thomas C. Scholten  
Delft, February 10, 2017*



# 1

## INTRODUCTION

ASML is a company founded in 1984 and created to develop lithography systems. The company is a result of a collaboration between Philips and Advanced Semiconductor Materials International (ASMI). Lithography machines fulfill an important step in the process of making chips. They print the 'blueprint' of the chips onto a wafer. The lithography step determines the smallest feature size of the chip, which is directly related to the computational power.

Figure 1.1 shows ASML's machines in historical order. The figure shows two values; the resolution and the overlay. The resolution is the smallest feature size that is possible to achieve with the corresponding machine. Overlay is the precision of two layers that are printed on top of each other. The resolution of a machine is highly dependent on the wavelength of the light that is used. The latest generation lithography machine uses Extreme UltraViolet (EUV) light with a wavelength of 13.5 nm.



Figure 1.1: Historical overview of the lithography machines made by ASML. Including the specifications per machine and the production year. [1]

One of the challenges that comes with using EUV, is the need to move towards a vacuum environment, as all photons are absorbed by air. An issue that occurs with the vacuum environment is the thermal behavior of heat dissipating components. In an atmospheric environment some of the heat is transferred by natural convection to the surrounding air. In a vacuum this is not the case, so other solutions to transfer the heat must be found.

To achieve the best resolution and overlay, the position of the wafer must be measured. This is done by using sensors to measure every relevant parameter. To process the data from the sensors; Printed Circuit Assemblies (PCAs) are used. The PCAs required to process the data are located on the waferstage, in the vacuum environment. The PCAs dissipate heat and contain temperature sensitive components and require active cooling. The PCAs are combined in a single E-box to provide the necessary cooling. An E-box is a titanium housing that is sealed from the vacuum. The cooling is provided in two parts; an air flow transfers the major-

ity of the heat, the remainder is transferred by the water cooled housing.

As one can imagine the use of an air flow to cool something in a vacuum environment is a bit contradictory. All the air is removed to create the vacuum, and on the other hand air is pumped into the E-box. Also all flow related components are leak tested at 10 bar(g), meaning the housing of the E-box must be constructed to withstand a 10 bar(g) load case. Which results in a rather large and heavy housing.

With all this in mind, the concept of a lean E-box was brought up. In this concept the air flow is completely removed and the PCAs are solely cooled by water. The heat transfer between the PCAs and the water should be done by a conductive path. To acquire the conductive solution the housing is filled with an epoxy like material; often referred to as 'potting'. The potting will fill the housing with the PCA inside and heat dissipated by the PCA will transfer via conduction through the potting to the water flow.

The first part of this work aims to provide a conceptual design for the lean E-box, which covers the basic working principles, such that the minimum specifications are met. The desired result is a conclusion on the thermal feasibility of the concept.

*Can the lean E-box concept be applied in a conceptual manner such that all thermal specifications are met?*

As part of this research we like to comment on how accurate the thermal behavior can be predicted by a mathematical model that uses a simplified geometry and contains a number of assumptions. The predicted performance will be verified by doing a series of measurements. The combination of results from the mathematical model and the measurements will conclude a verdict on the thermal feasibility.

*Is the predicted thermal behavior of the lean E-box also seen in an experimental measurement setup?*

A renowned optimization technique is topology optimization, which is a method to determine the optimized material distribution of a construction for certain load cases, or to achieve certain desired performance. For example, in structural mechanics this can result in a shape that minimizes compliance, i.e. maximizes stiffness. The difference between topology optimization and other kinds of optimization methods is that for topology optimization it is not required to know the shape of the design a priori. For this reason topology optimization is mostly applied in the early stages of the design process.

Most research on topology optimization focuses on arbitrary uniform heat loads. The lean E-box concept provides us with a highly non-uniform non arbitrary heat load. In this work we aim to research the possibility to do a topology optimization for an actual design case; the distribution of the water channels to cool the non-uniform heat load from the lean E-box. Since this research is done in cooperation with ASML - a public company - the optimization will be done with a commercial package that is widely used within ASML. We comment on the usability of topology optimization for an actual design load case.

*Can we apply a multiphysics topology optimization, describing heat transfer and fluid dynamics, for an actual design load case using a commercially available package?*

To simplify the underlining physics and reduce the computational cost of the optimization a few assumptions will be made. The main assumption that will be made is that the fluid dynamics can be described by a low Reynolds number flow. A comparison is made to investigate and verify this assumption.

*What is the effect of a low Reynolds number assumption on the topology optimization result and on the flow profile?*

Because the concept design for the lean E-box is part of this research, defining the design domain is also. Which opens up the possibility to research the influence of the position of the water inlet and outlet on the optimization result, and the performance of the resulting design. Implementing the inlet and outlet as a design variable in the optimization is not so straight forward. This will therefore not be discussed in this research, we will however address the influence by manually varying the positions. This way multiple results can be compared and a conclusion on the influence can be given.

*What is the influence of varying the inlet and outlet positions of the water flow on the result found for the topology optimization, and the performance of it?*

Just like the concept design of the lean E-box, the mathematically predicted performance increase by the optimized design will be verified by a series of measurements.

*Is the predicted performance increase by the topology optimization also seen in an experimental measurement setup?*

The final aspect of this work is a conclusion on the topology optimization for the lean E-box concept design. Topology optimization is a powerful tool in the design process, it is however not (yet) an easy applicable tool. It therefore takes a substantial amount of time to apply the topology optimization. If this time is a worthy investment, is for each design case different. We conclude this research with a discussion about the added value of the topology optimization for the lean E-box concept design.

*What is the added value of the topology optimization for the cooling channels of the lean E-box, and does it weight up to the time investment required for the optimization?*

## 1.1. OUTLINE OF THESIS

The outline of this thesis will be in the same order as the mentioned research questions. First the conceptual design of the lean E-box will be discussed, followed by the thermal calculations and the experimental setup. Next the topology optimization is discussed, first for an arbitrary uniform heat load which is extended by adding local hot spots. And concluding with the optimization for the cooling channels of the lean E-box. The disclosure of this thesis is done via a general conclusion.



# 2

## LEAN E-BOX

Inside the E-box, three different PCAs are placed. For the lean E-box concept the three PCAs will be placed in separate lean E-boxes. Which results in three lean E-boxes, all three using fundamentally the same concept. This means that if the concept is feasible for one of the PCAs, it almost certainly is also feasible for the other PCAs. Since the purpose of this research is only to verify the feasibility, and thus no detailed designs are required, it is sufficient to do the modeling and testing for only one PCA. The big question that remains is which PCA to use. To make a decision on this let us first look into the E-box and the PCAs in more detail.

The E-box is a rectangular box of approximately 200 mm by 100 mm by 60 mm. Two of the three PCAs are placed horizontally and the third is placed vertically, this setup is illustrated in Figure 2.1. The heat load of the E-box is at maximum dissipation 22.2 W, which is cooled by means of water cooling and air cooling. The heat load is not divided evenly over the PCAs, the individual heat load for each PCA will be derived in the next section.

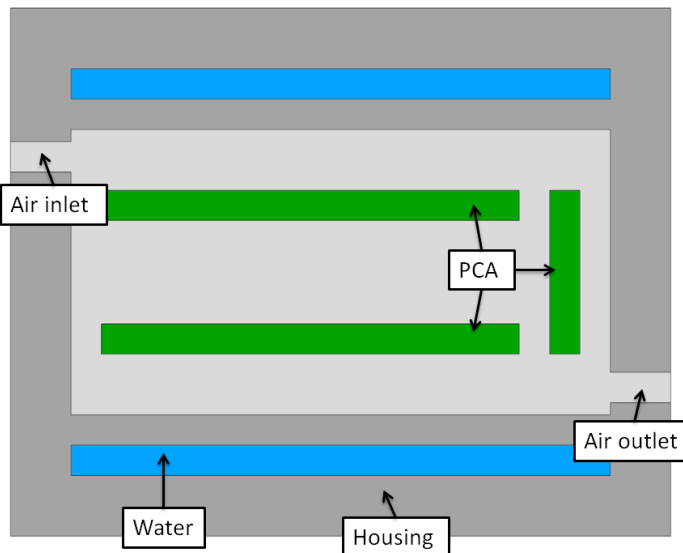


Figure 2.1: Schematic overview of the E-box layout; indicating the different materials and the layout of the PCAs.

### 2.1. PRINTED CIRCUITS ASSEMBLIES IN THE E-BOX

All three PCAs have fundamentally the same function; process data received from sensors located on the waferstage. For the convenience of the reader are the PCAs simply referred to as PCA 1, PCA 2 and PCA 3.

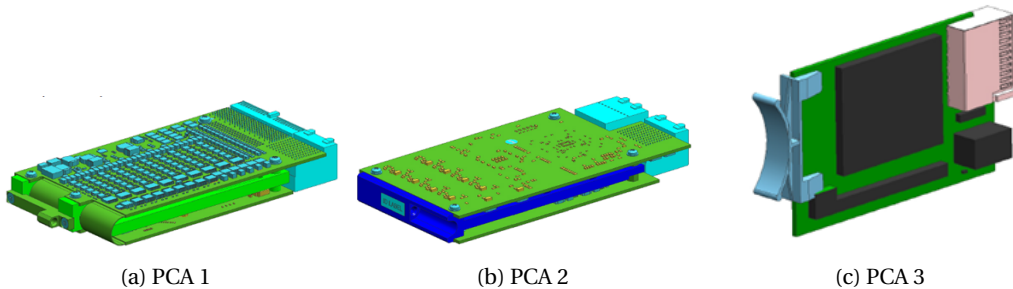


Figure 2.2: Illustrations of the three PCAs that are inside the E-box. PCA 1 and PCA 2 both have a sandwich like shaped. PCA 1 is however one print, while PCA 2 consists of two prints. PCA 3 is much smaller than PCA 1 and 2, the illustration may indicate differently.

### **2.1.1. PRINTED CIRCUIT ASSEMBLY NUMBER 1**

PCA 1 is approximately 150 mm by 80 mm by 20 mm. It consists of a single board that is folded in the middle, which results in a sandwich like shape, shown in Figure 2.2a. In total 241 components are located on PCA 1, with a total dissipation of 16W. The most critical temperature spec of a single component is 55 °C. An overview of the specifications is given in Table 2.1.

## **2.1.2. PRINTED CIRCUIT ASSEMBLY NUMBER 2**

PCA 2 is approximately 160 mm by 80 mm by 20 mm. It consists of two boards that are assembled into a single assembly. This results again in a sandwich like shape just as PCA 1, see Figure 2.2b. In total 221 components are located on PCA 2. The total dissipation of PCA 2 is 5 W. The most critical temperature spec of a single component is 60 °C. An overview of the specifications is given in Table 2.1.

### **2.1.3. PRINTED CIRCUIT ASSEMBLY NUMBER 3**

PCA 3 is approximately 85 mm by 50 mm by 10 mm. It only consists of one board. In total 76 components are located on PCA 3. The total dissipation of PCA 3 is 1.2 W. The most critical temperature spec of a single component is 60 °C. An overview of the specifications is given in Table 2.1. An illustration of PCA 3 is given in Figure 2.2c.

#### **2.1.4. CONCLUSIONS**

PCA 1 by far dissipates the most heat. Next to that it also has the most critical temperature spec. The combination of these two, results in the most critical load case. If the concept appears to be feasible for PCA 1, it most certainly is feasible for PCA 2 and 3. Therefore the decision is made to continue this research only for PCA 1. A follow up assignment / project can be done to implement the design of the PCA 1 lean E-box for PCA 2 and PCA 3. The principles of the design can be the same but the dimensions must be scaled to fit PCA 2 and PCA 3.

Table 2.1: Overview of the specification of the three PCAs inside the E-box

| Specification        | PCA 1                     | PCA 2                     | PCA 3                    |
|----------------------|---------------------------|---------------------------|--------------------------|
| Size [mm]            | $150 \times 80 \times 20$ | $160 \times 80 \times 20$ | $85 \times 50 \times 10$ |
| Number of components | 241                       | 221                       | 76                       |
| Power dissipation    | 16 W                      | 5 W                       | 1.2 W                    |
| Temperature spec     | 55 °C                     | 60 °C                     | 60 °C                    |

## **2.2. STAGES SATELLITE BOARD**

Instead of referring in the remainder of this work to PCA 1, the official name will be introduced. This is somewhat contradictory with what is stated in the previous section. But since there is only one PCA left, and thus no confusion on the reference can be made, I feel that it is more convenient to refer to the official name, which is Stages Satellite Board (SSB). In order to set up the Finite Element Method (FEM) model, the 16W dissipation needs to be divided over all the individual components on the SSB. Also the maximum allowed

temperature of each component needs to be derived.

There are 42 unique components on the SSB. For each unique component the dissipation is listed in Table A.1, found in Appendix A. In Figure 2.3 the SSB is shown together with a color scale of the power dissipation. The figure gives a good indication of the location of the heat loads.

In Table A.1 also the maximum temperature per component is listed. These temperatures are defined as the temperature at which the component does not function with the required accuracy anymore. In Figure 2.4 a similar image as Figure 2.3 is shown but instead of power dissipation the maximum allowed temperature is shown. This gives the reader a more clear view of the location of the components with a more critical temperature spec. Note that the temperature specs are given as a junction temperature. The junction temperature is the temperature of the core of the component.

A common way to describe the temperature difference between the junction and the outside of the component is with junction resistances. The junction resistance is explained in more detail in Appendix B. The junction resistances are also shown in Table A.1. Note that not all components have a junction resistance, if the component does not have a housing no junction resistance is required.

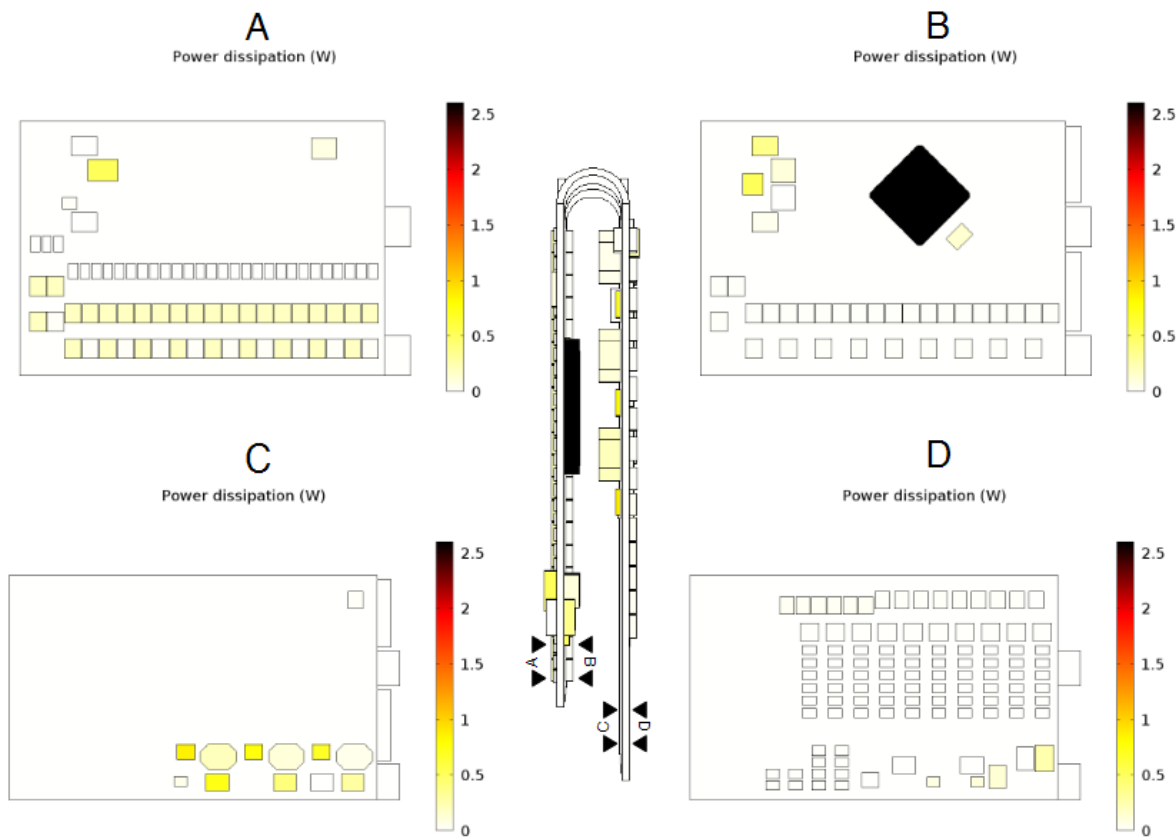


Figure 2.3: The spread of the heat dissipating components on the SSB. The darker the component, the higher the power dissipating. The maximum dissipation of 2.6 W is found in view B.

2

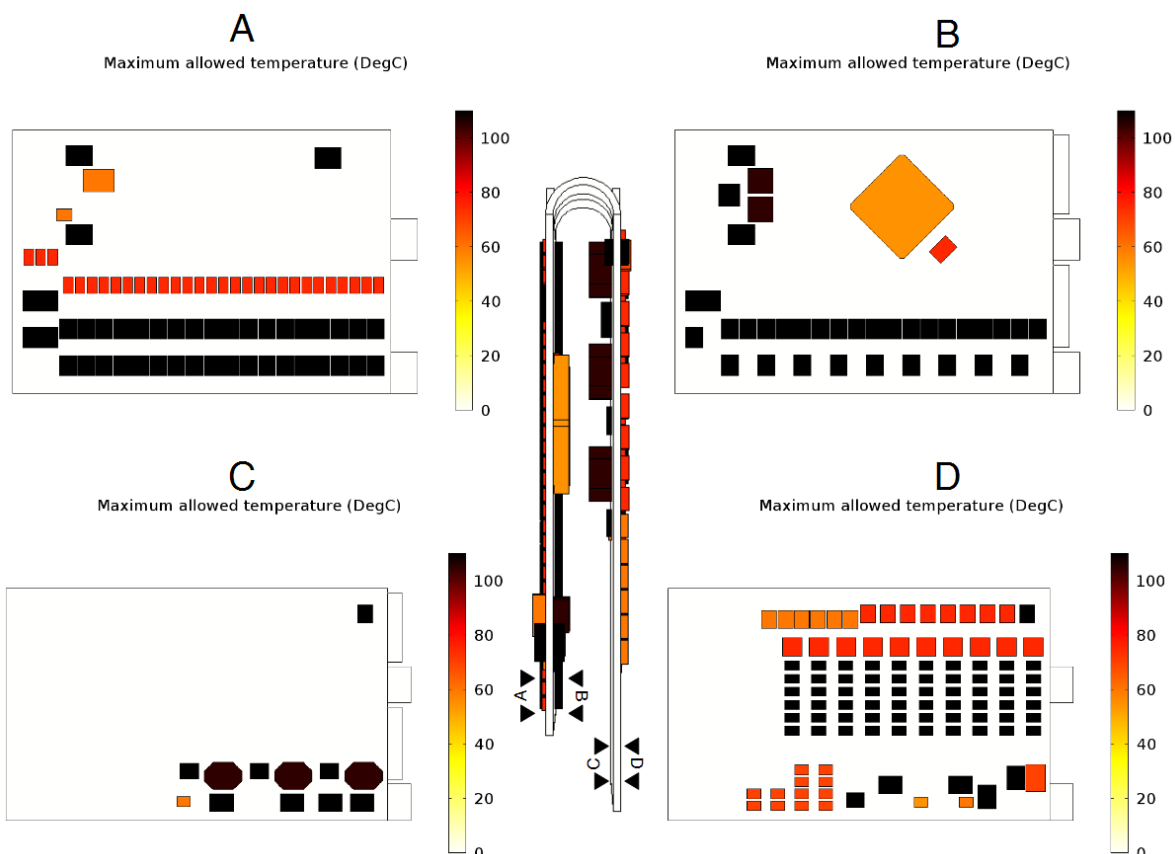


Figure 2.4: An overview of the maximum allowed temperatures. The darkness of the components indicates the maximum allowed temperature, the darker the component the higher the allowed temperature.

### 2.3. LEAN E-BOX CONCEPT

A layout of the lean E-box concept is given in Figure 2.5. The layout looks on first hand very similar to the one shown in Figure 2.1, only there is just one PCA left and the air is replaced with potting. There is however a big difference in load cases between the two. This is the removal of the 10 bar(g) load case.

The lean E-box concept has some big advantages compared to the original E-box concept but also some disadvantages. The two biggest advantages are: less mass and a more flexible volume. Because the housing does not have to be constructed for a 10 bar(g) load case anymore it can be much thinner. This will lead to a lower mass. And since there are now three separate boxes instead of one big box, the volume is much more flexible; instead of one big volume we now have three smaller volumes. The increase in flexibility of the volume can also increase the dynamic performance of the waferstage.

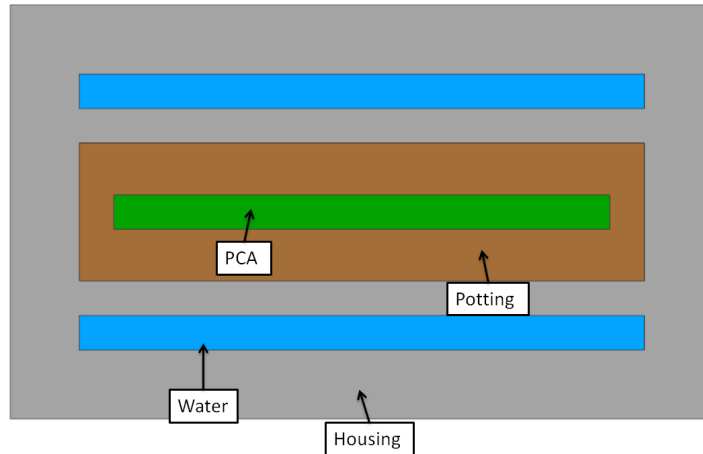


Figure 2.5: Schematic overview of the lean E-box concept layout indicating the different materials and the position of the PCA. Compared to Figure 2.1 the air is replaced by potting and there is only one PCA instead of three, this however means that three lean E-boxes are required to store all the PCAs.

Another advantage is the removal of the air flow. The E-box is the only component on the waferstage that requires an air flow. So if the air flow in the E-box is removed the air flow to the waferstage is also removed. Which results in fewer hoses and manifolds.

One of the big disadvantages is that the PCA can not be reused or repaired anymore. The PCAs inside the E-box are spare parts. For the lean E-box not only the PCA needs to be replaced but the complete lean E-box. Also more water manifolds are needed. The E-box only has one water manifold, but for the lean E-box three water manifolds are needed. A recommendation will be made on whether the advantages weigh up to the disadvantages.

### 2.4. SPECIFICATIONS

As part of this research, we aim to verify the feasibility of the lean E-box concept. It is important to have a clear overview of the specifications required for the final design. This is especially important for the concept design, if the specifications are not respected in the concept design then, from a practical perspective, the results from this research are useless.

All of the specifications are determined by ASML and are based on either ASML regulations or followed from previous design choices. The author of this work had no participation whatsoever in defining the specifications.

Most of the specifications are not relevant to determine the feasibility of the concept but are more detailed design related specs, therefore it is unnecessary to mention them in this thesis. They are however listed in an internal ASML document[30]. The main specifications that are important for the feasibility are listed in Table 2.2.

Table 2.2: The main specifications of the lean E-box.

2

| Requirement  | Value                  |
|--|------------------------|
| Maximum pressure drop available for the cool water of all three lean E-boxes | 1 bar                  |
| Maximum cool water flow available for all three lean E-boxes                 | $1 \text{ l min}^{-1}$ |
| The potting can not decrease the performance of the PCA                      | -                      |
| Maximum heat load to environment   | 5 W                    |

## 2.5. CONCEPT DESIGN

During the design process a couple iterations of the design were made, we will focus mainly on the final iteration of the design. The focus of this research is not on the design part but on the feasibility and optimization, therefore some decisions made during the design process will not be elaborated. In Appendix C a description is found of the three main design decisions.

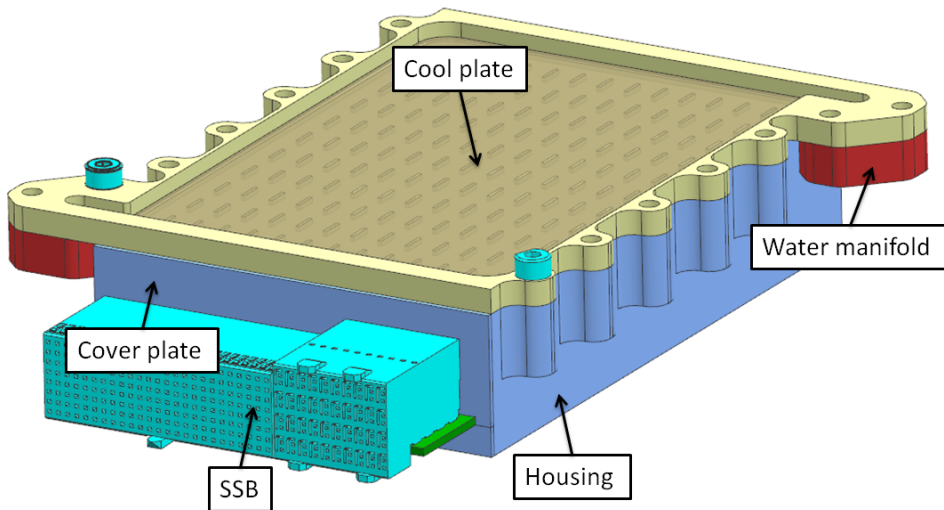


Figure 2.6: A CAD model of the final design of the lean E-box. The turquoise parts are the connectors of the SSB and the bolts, the blue part is the housing, the yellow part is the cool plate and the red parts are the water manifolds. For simplicity only one bolt of each size is used in the CAD model.

In Figure 2.6 the concept design is shown. The upper part is the cool plate, the cool plate is bolted to the housing. On both sides next to the bolts a water manifold is attached to the cool plate. On the water manifold the water supply and the water drain is attached. On the other side of the manifold an O-ring is mounted, the O-ring ensures a leak tight connection.

The cool plate is a two part piece, one thick part where the channels are milled out of and a second part which is a thin plate that is welded on top. The cooling channel structure is a structure with multiple small islands. By applying a welded connection between the thin plate and the islands a stiff connection is created, which is important because it is leak tested at 10 bar(g). The island structure is chosen because of its simplicity, the optimization of the cooling channels is still to be done.

The outer edges of the plate are slightly thicker than the middle. A structure like this adds fairly little mass but still provides an increase in clamping length. Which is required for the bolted connection. It also results in a larger contact pressure area between the cool plate and the housing. Fernlund described the pressure distribution between two plates by a cone shaped model [14]. An increase of the clamping length means an increase of the pressure area. The pressure area between the cool plate and the housing is important for the heat transfer, which is introduced in Appendix C and derived in Appendix D. An addition to the concept can be; to add a gap filler pad between the cool plate and the housing. This will increase the heat transfer between the two. A comment will be given when discussing the FEM results on the necessity of the gap filler pad.

The potting of choose is the *Epotek T7109-19*, which is chosen after some initial research and consulting with an adhesive expert. The material properties are shown in Table 2.3. The maximum allowed temperature is 200 °C which is far higher than the maximum allowed component temperature for the SSB. The downfall of the Epotek potting is the relatively high viscosity. However with the use of proper potting techniques this will not cause problems. By using a pressure difference between a potting inlet and outlet, the potting is forced to fill the volume and the air to leave the volume. The result is a potted volume with little to no air voids.

Table 2.3: Material properties Epotek T7109-19.

| Base material | Thermal conductivity                  | Density                 | Viscosity    | Volume resistivity        |
|---------------|---------------------------------------|-------------------------|--------------|---------------------------|
| Epoxy         | 1.3 W K <sup>-1</sup> m <sup>-1</sup> | 1300 kg m <sup>-3</sup> | 55 000 mPa s | 5 × 10 <sup>12</sup> Ω cm |

The mass of the lean E-box is approximately 0.6 kg. If we assume that the mass of the lean E-box for PCA 2 is equal to this, and that of PCA 3 only half. A total mass of 1.5 kg is found. This is a 1.3 kg reduction compared to the 2.8 kg mass of the E-box.

## 2.6. FINITE ELEMENT MODEL

The FEM model is made with Comsol® multiphysics software. The starting point of the model is the SSB; a simplified model is created that contains all the heat dissipating components, listed in Table A.1. All other parts on the SSB are removed. This will be the geometry of the model. Each component is modeled as a rectangle, which is taken as a heat source with the corresponding dissipation.

The junction resistances are added by modeling them as a thin layer with the corresponding thermal resistance. A simple calculation is done to verify this implementation, as presented in Appendix B. This same method is used to model the contact resistance between the housing and the cool plate. The model of Yovanovich [20] is used to determine the contact resistance. And the model of Fernlund [14] [29] is used to determine the area of the contact pressure. On this area the thermal resistance is applied. The remaining contact area between the cool plate and the housing has a negligible heat transfer coefficient. See Appendix D for the complete derivation of the values.

The gap filler pad is modeled as a material layer between the cool plate and the housing. The layer has the material properties of the gap pad. The same is done for the glued surfaces, where a thickness of 0.1 mm is assumed. For the gap pad model the contact resistances are removed.

### 2.6.1. PHYSICS

The fluid dynamics are modeled with an incompressible non-isothermal flow which is governed by the Navier-Stokes equations, which are formulated in the most general form by the conservation of mass, momentum and energy:

$$\frac{\partial \rho}{\partial t} \nabla \cdot (\rho \mathbf{u}) = 0 \quad (2.1)$$

$$\rho \frac{\partial \mathbf{u}}{\partial t} + \rho (\mathbf{u} \cdot \nabla) \mathbf{u} = \nabla \cdot [-p \mathbf{I} + \boldsymbol{\tau}] + \mathbf{F} \quad (2.2)$$

$$\rho C_p \left( \frac{\partial T}{\partial t} + (\mathbf{u} \cdot \nabla) T \right) = -(\nabla \cdot \mathbf{q}) + \boldsymbol{\tau} : \mathbf{S} - \frac{T}{\rho} \frac{\partial \rho}{\partial T} \Big|_p \left( \frac{\partial p}{\partial t} + (\mathbf{u} \cdot \nabla) p \right) + \mathbf{Q} \quad (2.3)$$

Where  $\rho$  is the density,  $\mathbf{u}$  is the velocity vector,  $p$  is the pressure,  $\boldsymbol{\tau}$  is the viscous stress tensor,  $\mathbf{F}$  is the volume force vector,  $C_p$  the specific heat capacity at constant pressure,  $T$  is the absolute temperature,  $\mathbf{q}$  is the heat flux vector,  $\mathbf{Q}$  the heat source and  $\mathbf{S}$  the strain-rate tensor given by  $\mathbf{S} = \frac{1}{2}(\nabla \mathbf{u} + (\nabla \mathbf{u})^T)$ . The operator ':' is a double dot product defined as:

$$\mathbf{A} : \mathbf{B} = \sum_n \sum_m a_{nm} b_{nm} \quad (2.4)$$

For the fluid we use water, which is a Newtonian fluid and therefore the viscous stresses are described by:

2

$$\boldsymbol{\tau} = 2\mu \mathbf{S} - \frac{2}{3}\mu(\nabla \cdot \mathbf{u})\mathbf{I} \quad (2.5)$$

Where  $\mu$  is the dynamic viscosity. The heat transfer part of the fluid is described by the heat equation:

$$\rho c_p \frac{\partial T}{\partial t} + \rho C_p \mathbf{u} \cdot \nabla T + \nabla \cdot \mathbf{q} = \mathbf{Q} \quad (2.6)$$

Where  $\mathbf{q} = -k\nabla T$  with  $k$  is the thermal conductivity. For the non fluid part of the model the heat equation is also used, with  $\mathbf{u} = \mathbf{0}$ . For more information on how Comsol handles the physics see the Comsol reference manual [2].

## 2.7. RESULTS

In Figure 2.7 four cut planes of the lean E-box are shown. The cut planes are the four PCA sides where the components are mounted on. The temperature scale of all four planes is set equal with the upper limit of the temperature corresponding with the maximum found temperature of 48.3 °C. This maximum temperature is found on side 4 shown in Figure 2.7d. The component with the maximum temperature is component C5, which has a maximum allowed temperature of 110 °C.

Table 2.4: Temperatures of the most critical components calculated with the FEM.

| Component | Specification | Temperature FEM result |
|-----------|---------------|------------------------|
| C2        | 55 °C         | 37.3 °C                |
| C8        | 60 °C         | 30.8 °C                |
| C12       | 60 °C         | 34.5 °C                |
| C28       | 55 °C         | 36.9 °C                |
| C29       | 60 °C         | 35.4 °C                |
| C23       | 60 °C         | 37.3 °C                |

In Table 2.4 the temperatures of the components with the most critical temperature specs are shown. It is seen that all components are within spec, with still a significant margin. All the temperature results are for an inlet velocity of  $0.21\text{min}^{-1}$ . The total amount of available flow for all three lean E-boxes is  $1\text{lmin}^{-1}$ . This means that  $0.21\text{min}^{-1}$  is a realistic amount of flow for the SSB. The corresponding pressure drop according to the FEM model is 0.019 bar. This is also a good amount within the 1 bar spec.

In Figure 2.8 one can see the temperature distribution of the top side of the cool plate. The bottom left side is less cooled than the top right corner. Because of the -by choose- poor design of the channels, the water does not distribute evenly over the channel. But as mentioned before not much time is spent on the design of the cooling layout. A simple way to increase the water distribution is to make a groove along the y-direction on the outsides of the cooling channels. In the groove the pressure will be lower than in the channel. Because of this the water will first distribute over the groove and then over the channels.

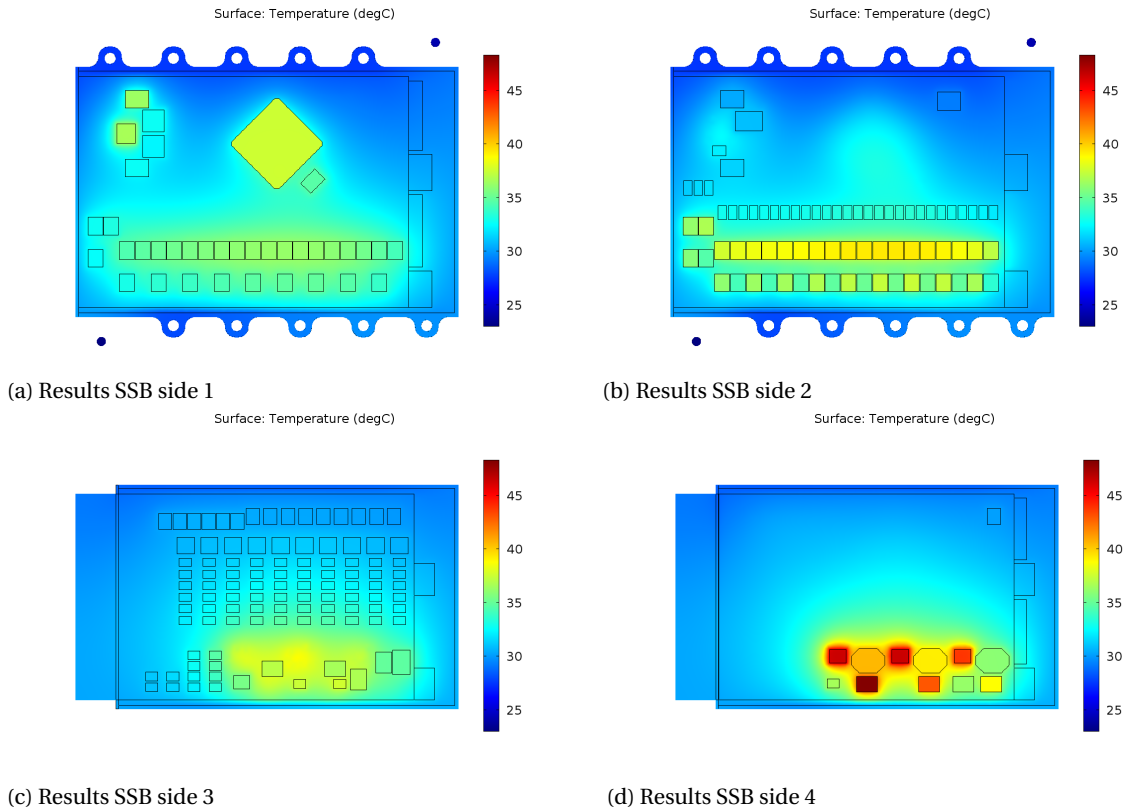


Figure 2.7: Temperature plots of the components of the SSB for  $0.21\text{min}^{-1}$  water flow. The maximum temperature of  $48.3^\circ\text{C}$  is found in 2.7d for component C5.

Table 2.5: Temperatures of the most critical components for the model with the gap pad.

| Component | Temperature FEM result | Temperature gap pad  | Difference          |
|-----------|------------------------|----------------------|---------------------|
| C2        | $37.3^\circ\text{C}$   | $29.5^\circ\text{C}$ | $7.8^\circ\text{C}$ |
| C8        | $30.8^\circ\text{C}$   | $26.3^\circ\text{C}$ | $4.5^\circ\text{C}$ |
| C12       | $34.5^\circ\text{C}$   | $30.8^\circ\text{C}$ | $3.7^\circ\text{C}$ |
| C28       | $36.9^\circ\text{C}$   | $33.7^\circ\text{C}$ | $3.2^\circ\text{C}$ |
| C29       | $35.4^\circ\text{C}$   | $32.6^\circ\text{C}$ | $2.8^\circ\text{C}$ |
| C23       | $37.3^\circ\text{C}$   | $33.8^\circ\text{C}$ | $3.5^\circ\text{C}$ |

The average outside temperature of the lean E-box is  $27.9^\circ\text{C}$ . The heat flux to the environment is  $0.45\text{W}$ . An ASML accepted assumption for the vacuum is a  $2\text{Wm}^{-2}\text{K}^{-1}$  heat transfer coefficient. This  $2\text{Wm}^{-2}\text{K}^{-1}$  induces the  $0.45\text{W}$  heat flux.

The FEM simulation is also done with the gap filler pad. The gap filler pad should increase the heat transfer between the cool plate and the housing. In Figure 2.9 the same cut planes are plotted as in Figure 2.7. The same color scale is used in both figures, which makes it clear that the temperatures for the model with the gap filler pad are lower. The maximum temperature is still found for component C5 and is  $44.3^\circ\text{C}$ . In Table 2.5 the temperatures for the most critical components are shown for the model with and without the gap filler pad. Also the difference in temperature is shown. All critical components show a lower temperature for the model with the gap filler pad. The maximum difference found is  $7.8^\circ\text{C}$  for component C2. The average outside temperature for the gap filler model is  $25.3^\circ\text{C}$  and the heat load to the environment is  $0.21\text{W}$ . From this we can conclude that the use of a gap filler pad results in an overall lower temperature. The necessity of the gap filler pad is however debatable since the temperatures without the gap filler pad are already within spec.

2

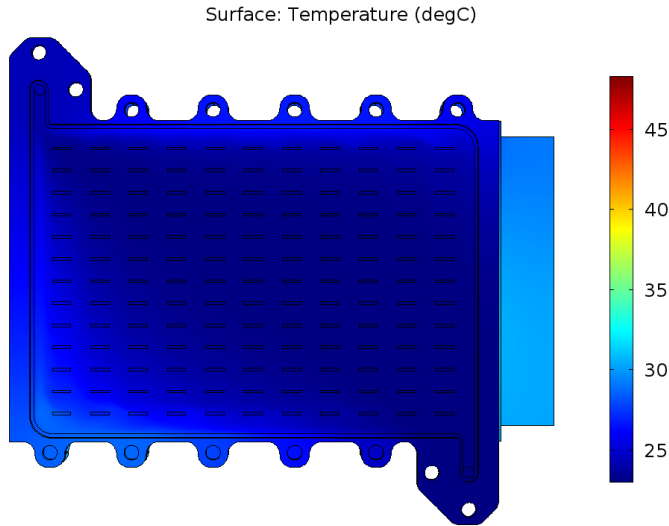


Figure 2.8: Temperature plot of the cool plate as a results of the FEM simulation. The image gives an indication of the temperature distribution of the cool water, the top left side is the water inlet and the bottom right is the water outlet.

The main contributor for the heat transfer to the environment is not taken into account in this model; heat conduction via the connection with the waferstage. The reason for not implementing this is because the connection is not known. The heat conduction to the waferstage can increase the heat load to the environment significantly. And by using a small addition in the form of a gap filler pad the average outside temperature can be reduced by 2.6 °C. Which also results in a decrease in heat conducted to the waferstage. If the heat load to the environment becomes a problem when designing the connection to the waferstage, the use of a gap filler pad can be considered.

## 2.8. PROTOTYPE DESIGN

To verify the results from the FEM model a prototype is made. The prototype design is in some ways different from the design mentioned in Section 2.5. The main reason for this is to cut costs.

The first difference is the removal of the water manifolds. In the lithography machine this is how the water inlet and outlet are connected to the cool plate. The water manifolds have to be leak tight and are therefore designed with an O-ring. For the prototype this is not necessary. Instead of the water manifolds, a quick connector is used that has on one side a connection interface for a hose and on the other side a threaded head. Two connectors of this type are connected on the top side of the cool plate.

This brings us to the next thing that differs from the concept design, which is the cool plate. In the concept design the cool plate consists of two parts that are welded together. The welding is however an expensive and time consuming process. Therefore the decision is made to connect the two parts of the cool plate via a bolted connection. One downfall that comes with this decision is that an O-ring is required to make sure the plate is leak tight. In the concept design of the cool plate there is no space for the O-ring. Therefore the cool plate is made bigger, 10 mm wider, 14 mm longer and 3 mm thicker. The increase in thickness is because of the threaded holes in the bottom side of the cool plate, and the threaded hole for the water connector in the top side.

Another big differentiation from the concept design is the insertion of the SSB. One of the design decisions was to slightly elongate the SSB in order to fit a cover plate to seal the potting from the vacuum. This is discussed in Appendix C. However the SSB we have at hand for testing purposes is not elongated. This concept can thus not be used. The risk of damaging the components is not one we want to take. For this reason we can not attach the cover plate to the SSB. The solution we came up for this is to not use a cover plate. If this was to be implemented in the real machine it will not qualify because of the outgassing properties of the potting material. But since this is only a prototype it is not a big deal that the potting is exposed.

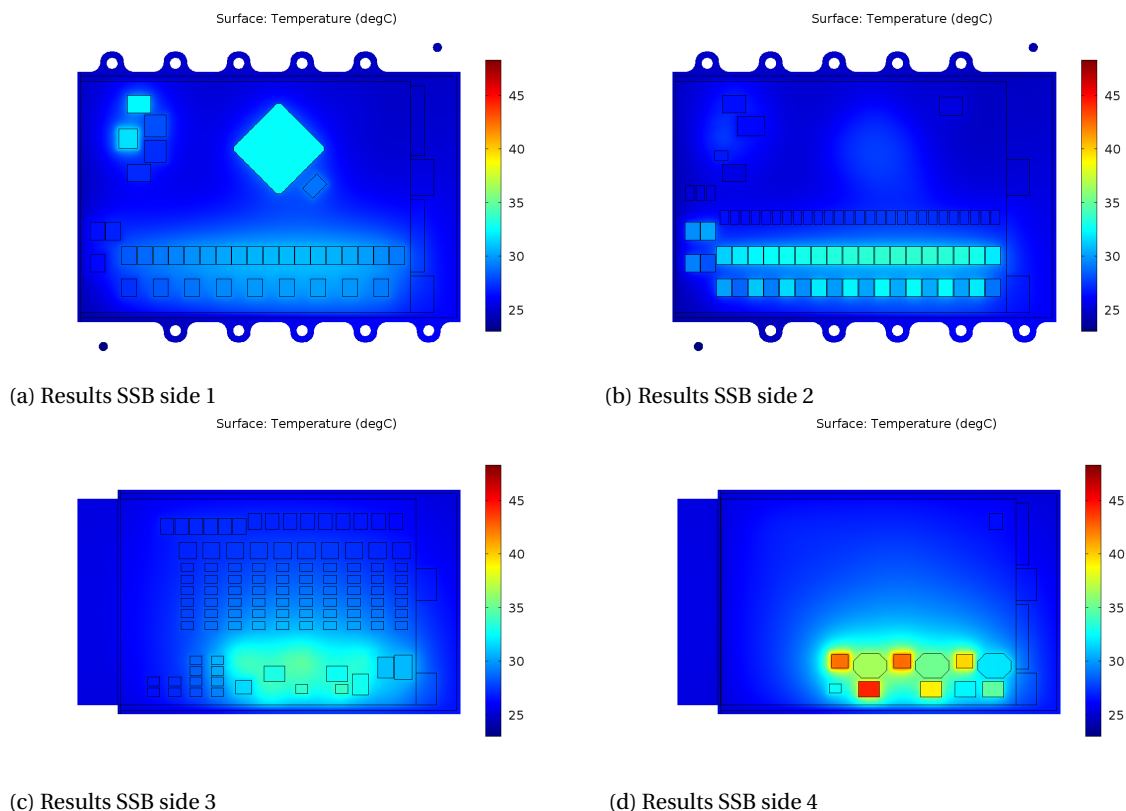


Figure 2.9: Temperature plots of the components of the SSB with the gap pad for  $0.21\text{ min}^{-1}$  water flow. When comparing the results with Figure 2.7 an overall lower temperature is found. The maximum temperature is still found for component C5, shown in 2.9d.

Table 2.6: Material properties Rhenatech EP 5470 FR and Epotek T7109-19.

| Material name | Thermal conductivity                  | Density                 | Viscosity   | Volume resistivity                     |
|---------------|---------------------------------------|-------------------------|-------------|--|
| Rhenatech     | $0.96 \text{ WK}^{-1} \text{ m}^{-1}$ | $1620 \text{ kgm}^{-3}$ | 3000 mPas   | $5.6 \times 10^{14} \Omega \text{ cm}$ |
| Epotek        | $1.3 \text{ WK}^{-1} \text{ m}^{-1}$  | $1300 \text{ kgm}^{-3}$ | 55 000 mPas | $5 \times 10^{12} \Omega \text{ cm}$   |

There is a big catch for not using a cover plate, the previously mentioned potting method can not be used anymore. The consequence of this is that also the Epotek potting is not suited anymore. Because of the high viscosity it must be potted with the previously mentioned technique in order to fill the complete volume. Therefore it is decided to use a different potting for the prototype. This potting has a much lower viscosity, because of this it can be potted by just pouring the potting in the housing. When the housing is filled it can be placed in a vacuum chamber. This way the remaining air voids will be removed. The potting that will be used for the prototype is the *Rhenatech EP 5470 FR*. Of which the material properties are shown in Table 2.6.

The thermal conductivity of the Rhenatech is slightly lower than that of the Epotek. This means that the component temperatures will be a little higher with respect to the Epotek.

The total design is shown in Figure 2.10. The prototype design will be used during testing. To verify the results of the FEM model, the model is adjusted to match the design changes applied to the prototype design. Unfortunately it was not possible to perform the measurements in a vacuum environment due to time restrictions. This has an effect on the thermal contact between the coolplate and the housing, see Appendix D.

## 2.9. CONCLUSION

*Can the lean E-box concept be applied in a conceptual manner such that all thermal specifications are met?*

This chapter presents the background of the lean E-box concept, including a list of specifications that need to

2

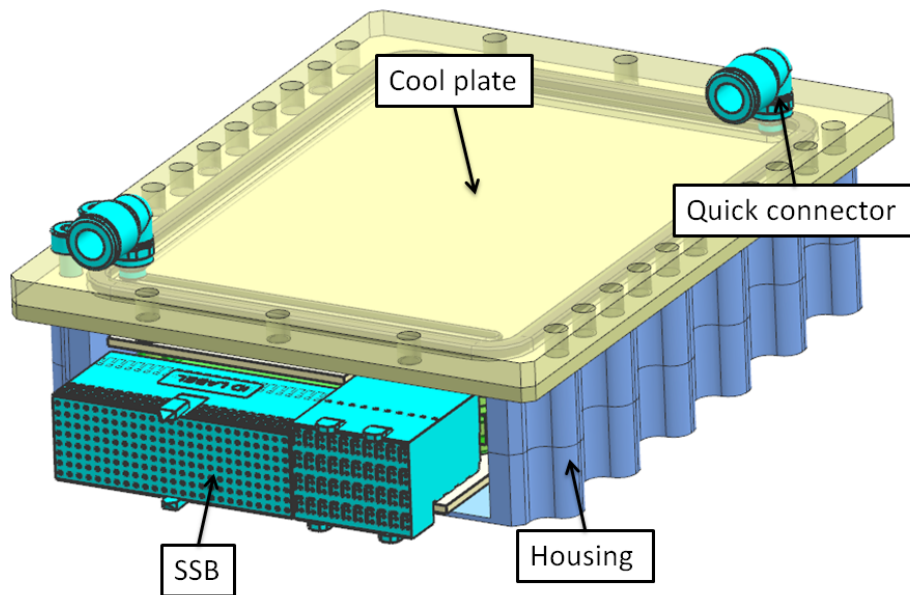


Figure 2.10: The CAD model of the prototype design of the lean E-box. The turquoise parts are the connectors, the bolts and the water connectors, the yellow part is the cool plate and the blue part is the housing.

be met. A concept design is created according to these specifications aiming to answer the research question.

The results from the FEM simulation show that all the component temperatures stay below the maximum allowed temperatures. Also the maximum allowed flow rate and pressure drop are not exceeded. From this we can conclude that the concept is thermally feasible. We however need to first verify the FEM results by means of a measurement setup to give a final answer to the research question.

# 3

## MEASUREMENTS

To verify the results from the FEM simulation a series of measurements are performed. The results of these measurements will be sufficient to verify the results from the FEM simulation. The results will also tell something about the performance of the potted SSB in comparison to the non-potted SSB. The following measurements are done; power dissipation before and after potting, surface flatness before and potting and temperature measurements.

This chapter will only focus on the temperature measurements, the remaining four measurements are discussed in Appendix E.

### 3.1. TEMPERATURE

The FEM results concluded that the lean E-box concept is feasible. This will be verified with the temperature measurements. The measurements give both a validation on the feasibility and the FEM model. If the FEM model of the prototype is verified, it is assumed that the model of the actual design is also verified.

#### 3.1.1. MEASUREMENT SETUP

For the temperature measurement two additional components are needed. First the so called SSB Q-tool, Figure 3.1. The Q-tool is a test interface board, designed to do measurements on the SSB. It consists of many connectors, however only two will be used; the power supply and the connector that connects the SSB to the Q-tool.

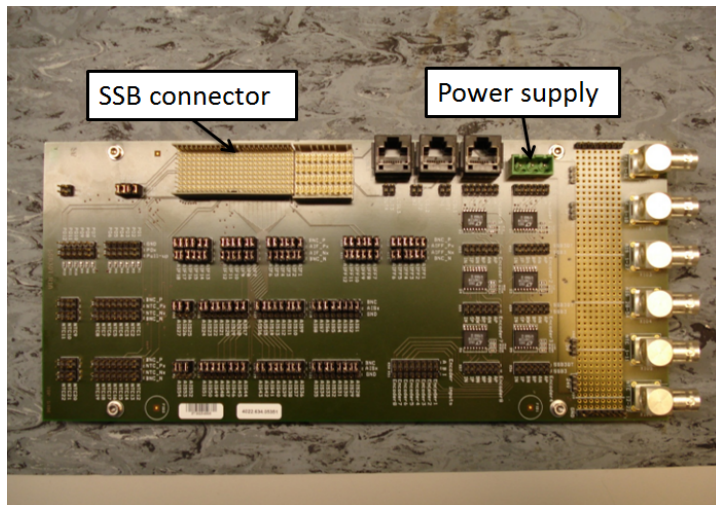


Figure 3.1: A picture of the SSB Q-tool that is used to do the measurements. The Q-tool has a connector for the SSB and a power supply input, next to a variety of ports that are connected to different components on the SSB. The latter will not be used for this measurement.

Table 3.1: The resistance values attached to the output to make the SSB dissipate maximum.

| Output     | Resistance [Ω] |
|------------|----------------|
| $V_{out1}$ | 6.66           |
| $V_{out2}$ | 10.66          |
| $V_{out3}$ | 13.33          |

### 3

The second additional component that will be used is a resistor board. The resistors are needed for the SSB to achieve maximum dissipation. They are attached to different outputs of the SSB, the outputs and the resistances are shown in Table 3.1. A breadboard is used to connect the resistors, see Figure 3.2.

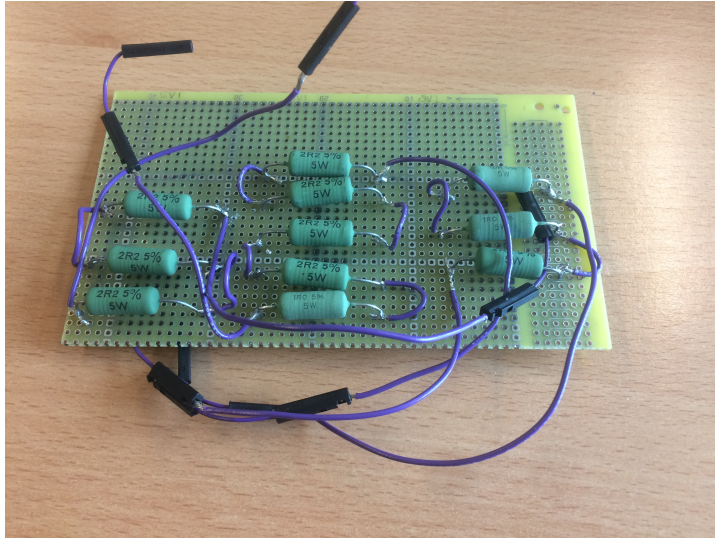


Figure 3.2: A picture of the resistors board that will be attached to the Q-tool.

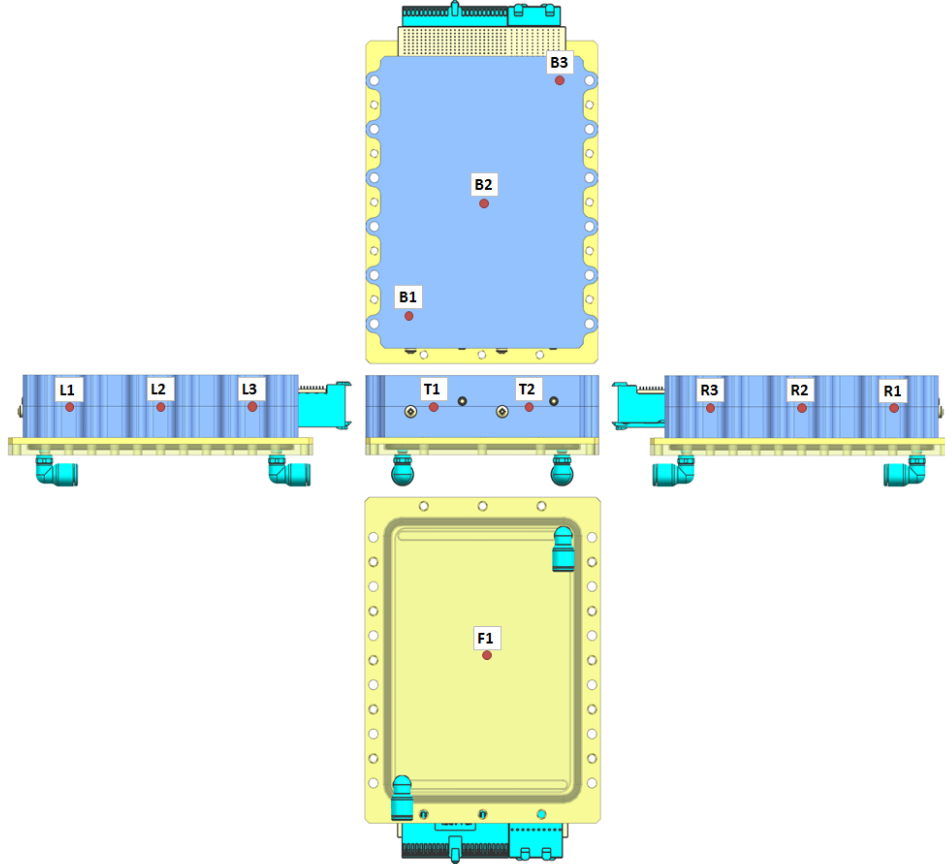
The temperatures will be measured via thermocouples and a logger. In total there will be nineteen thermocouples. Seven are glued on the components of the SSB and twelve are attached to the outside of the lean E-box. The locations of the thermocouples on the outside are shown in Figure 3.3. A selection is made of the most critical components and components that are less critical but in areas with higher temperatures. The following components, listed in Table A.1, are chosen to be measured; C2, C28, C8, C12, C29, C1, C29.

For the water supply a thermal control unit is used. This is a pump with a temperature controlled water reservoir. The downside of this instrument is that it is not possible to control the amount of water flow. This means that the flow must be controlled manually by using a valve. To make the temperature measurement repeatable multiple valves are used; each valve preset to allow a certain amount of flow. In Figure 3.4 the test setup is shown.

#### 3.1.2. MEASUREMENT PROCEDURE

In total twenty different measurements are done. Five different connections between the coolplate and the lean E-box, each measured for four different flow rates. The different connections are; bolted with 4,6,8 and 12 bolts and with 4 bolts and a gap filler pad. The flow rates are respectively; 0.1, 0.3, 0.4 and  $0.5 \text{ l min}^{-1}$ .

The thermocouples are attached to a logger. The temperatures will be denoted when the temperature of a single component has not changed for 15 min.



3

Figure 3.3: The thermocouple locations on the outside of the lean E-box. The red dots represent a thermocouple and their name.

### 3.1.3. RESULTS

In Figure 3.6 the measurement results of the components are plotted. All setups show approximately the same relation between flow and temperature.

The number of bolts and the gap pad don't have a large impact on the component temperatures. The main reason for this is that the measurements are done in an atmospheric environment. As explained in Appendix D; the gas conductance is dominant in areas where the contact pressure is low i.e. everywhere except near the bolts. This means that removing a bolt in an atmospheric environment has a much lower impact than removing a bolt in a vacuum environment.

The same holds for the gap filler pad; not much performance difference is seen. In a vacuum environment the difference will probably be much higher. However the problems with the detachment of the gap filler pad are of such significance that the conclusion can be made that a gap filler pad is not preferred. The material of the gap pad makes it impossible to detach it without damaging the pad. In Figure 3.5 a picture is shown where the gap pad is being removed. As one can see the material crumbles and breaks. This can cause issues during servicing of the lean E-box.

With the results from the measurements known we can now compare the results with the FEM results. In Figure 3.7 the results from the measurements and the FEM are plotted in a bar graph, the results are for a flow of  $0.5 \text{ l min}^{-1}$ . The measured temperatures of all components are well below spec. Also the temperatures of the measurements and the FEM are approximately the same.

We see that components C8, C12, C1 and C9 are approximately the same for the measurements and the FEM. There is still a marginal error, but this can be accounted for by the measurement error. Component C2 is the only component where the measured temperature is significantly lower than the FEM temperature. Com-

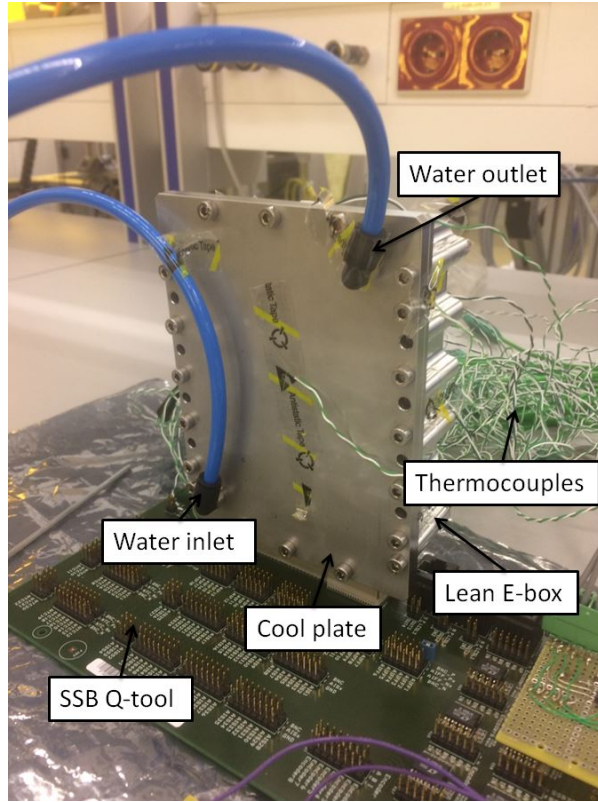


Figure 3.4: A photograph of the measurement setup used for the temperature measurements. The bottom hose is the water inlet and the top is the outlet. The green/white wires are the thermocouples.

ponent C2 is a component where the power dissipation is dependent on the temperature of the component. This relation is not implemented in the FEM model. Since the measured temperature ( $26.3^{\circ}\text{C}$ ) is quite low it is most likely that the power dissipation stated in the data sheet is for a higher temperature. The remaining errors can be accounted for by the assumptions made in the FEM model.

In Figure 3.8 the results for all measurement points are shown, including the outside temperatures. The predicted temperature from the FEM model corresponds in general very well with the measured temperature. This shows that the general temperature distribution of the FEM model is accurate.

### 3.2. CONCLUSION

*Is the predicted thermal behavior of the lean E-box also seen in an experimental measurement setup?*  
The temperature measurement, including the measurement setup and the measurement procedure is presented in this chapter. By means of a measurement setup the FEM results are verified.

*Can the lean E-box concept be applied in a conceptual manner such that all thermal specifications are met?*  
The thermal behavior of the FEM model and the prototype is, to a certain extend, similar. The deviations between the two can be explained by the measurement error and the assumptions made in the FEM model. By verifying the FEM results an approving conclusion is made on the thermal feasibility of the lean E-box concept.

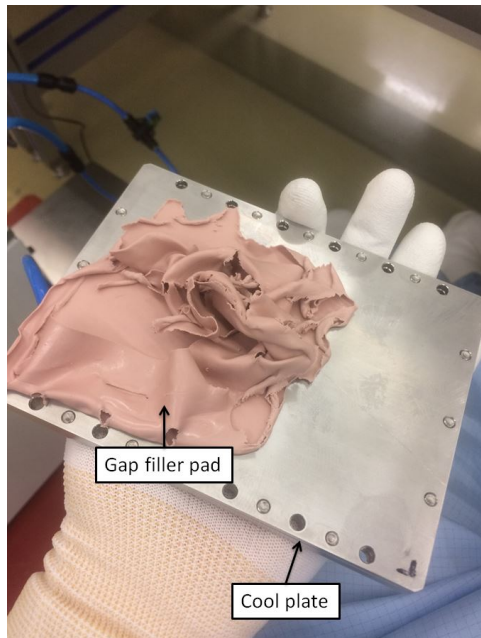


Figure 3.5: A picture of the gap pad when trying to remove the gap pad from the cool plate. As one can see the gap pad is not easily removed without damaging it. The material crumbles and breaks when detaching it.

3

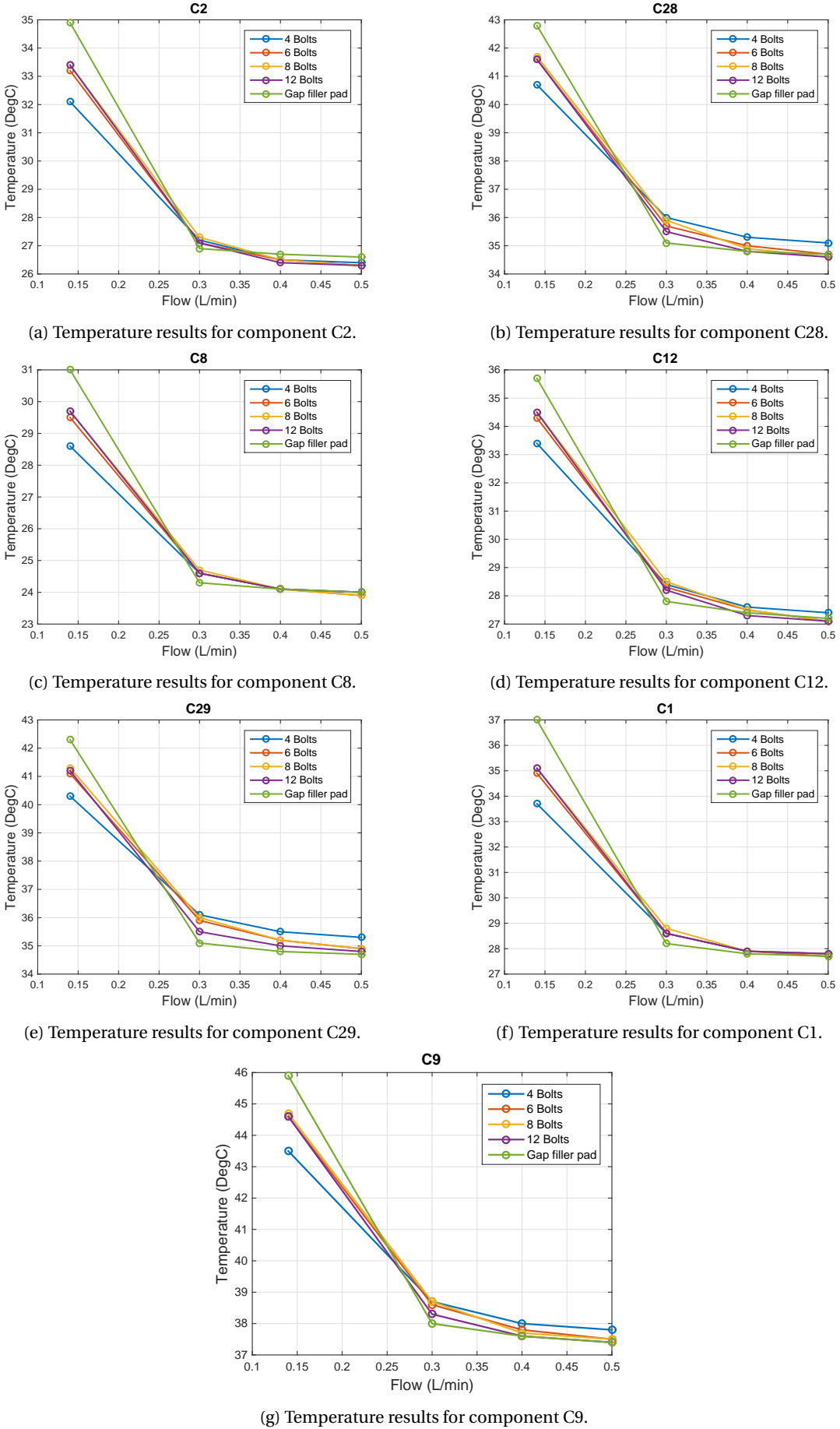


Figure 3.6: The results of the temperature measurements. Only the temperatures of the components are shown, the temperatures of the outside will be discussed later. The figure shows the measured temperature against the flow for five different connections between the cool plate and the lean E-box.

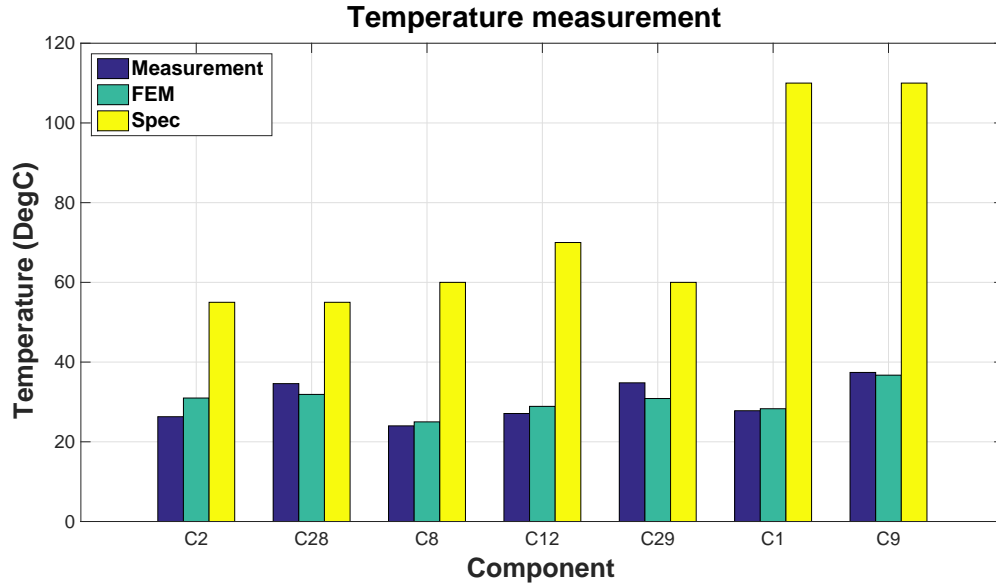


Figure 3.7: The results of the temperature measurements of the components of the SSB together with the FEM results and the spec. The component names correspond to the ones given in Table A.1.

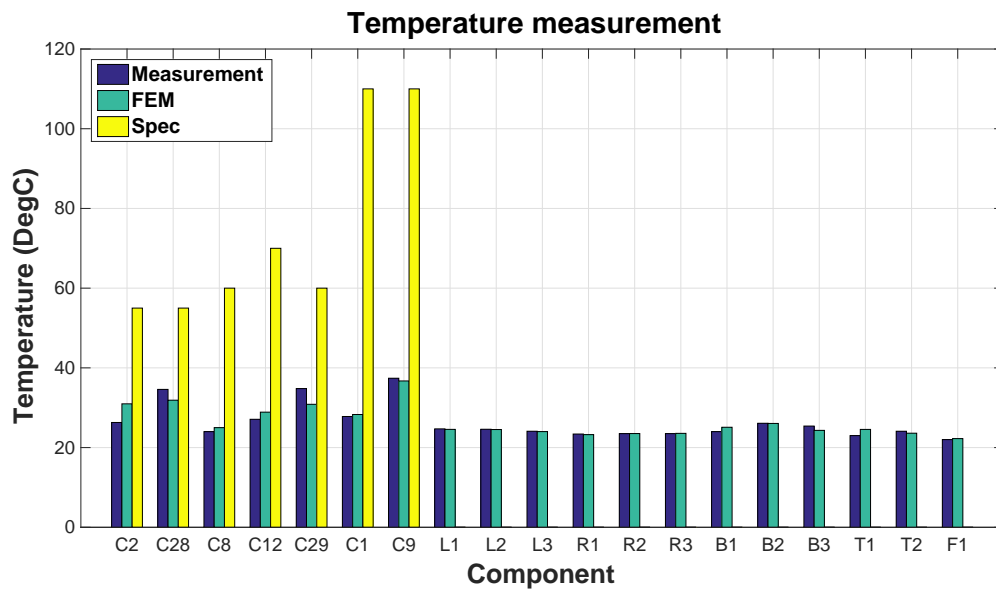


Figure 3.8: The results of the temperature measurements of the components of the SSB and the outside of the lean E-box together with the FEM results and the spec. The component names correspond to the ones given in Table A.1. And the outside thermocouple locations to the ones stated in Figure 3.3. For the measured locations on the outside there are no direct specifications since they are not directly coupled to a component.



# 4

## TOPOLOGY OPTIMIZATION OF HEAT TRANSFER AND FLUID DYNAMICS

This chapter describes an introduction to topology optimization. The theory will be explained, and two arbitrary load cases will be optimized.

Topology optimization uses a mathematical formulation to optimize the material distribution in a given design domain for given loads and boundary conditions. The mathematical formulation consists of a physics part and an optimization part. The physics is most of the times represented by the Finite Element Method. For the optimization part there are two categories; gradient based and non-gradient based approaches. For non-gradient see the work of Sigmund [32]; this work discusses most of the non-gradient based approaches. Some of the gradient based approaches are; level-set method [43][15], density based approach [8] and homogenization approach [7]. For more information on topology optimization see the book of Bendsoe and Sigmund [21].

Topology optimization is used for a wide range of applications. On going research attempts to extend the range of applications. One of the applications that currently receives a lot of attention is multiphysics topology optimization, which is also the focus of this research. The physics involved for this work are heat transfer and fluid dynamics. Unlike most research on thermal-fluid topology optimization an actual -industrial- design heat load will be used rather than the often presented uniform heat loads.

### 4.1. FLUID DYNAMICS

The main equations that model the fluid dynamics are the Navier-Stokes equations. The Navier-Stokes equations are given by:

$$\rho \left( \frac{\partial \mathbf{u}}{\partial t} + \mathbf{u} \cdot \nabla \mathbf{u} \right) - \mu \nabla^2 \mathbf{u} = -\nabla p + \mathbf{f} \quad (4.1)$$

$$\frac{\partial \rho}{\partial t} + \nabla \cdot (\rho \mathbf{u}) = 0 \quad (4.2)$$

Where  $\mu$  is the dynamic viscosity,  $\mathbf{u}$  is the velocity field,  $\rho$  is the material density,  $p$  is the pressure field and  $\mathbf{f}$  is the body force. The first term ( $\frac{\partial \mathbf{u}}{\partial t}$ ) describes the transient behavior, the second term ( $\mathbf{u} \cdot \nabla \mathbf{u}$ ) describes the inertial forces and the third term ( $\mu \nabla^2 \mathbf{u}$ ) describes the viscous forces.

The first assumption that is made is that the advective inertial forces are small compared to the viscous forces. This means that the Navier-Stokes equations can be linearized. Also we assume a steady flow. Therefore, the first two terms of Equation 4.1 drop out. Combined with the assumption of an incompressible flow this results in the Stokes equations:

$$-\mu \nabla^2 \mathbf{u} + \nabla p = \mathbf{f} \quad (4.3)$$

$$\nabla \cdot \mathbf{u} = 0$$

To model the solid and fluid domains a porous media flow model is used. This is done via the Darcy equations [16]:

$$\alpha \mathbf{u} = (\nabla p - \mathbf{f}) \quad (4.4)$$

$$\nabla \cdot \mathbf{u} = 0$$

Where  $\alpha$  is the inverse permeability. The Darcy equations are combined with the Stokes equations by using the Brinkman equations:

$$\mu \nabla^2 \mathbf{u} + \alpha \mathbf{u} = \nabla p - \mathbf{f} \quad (4.5)$$

$$\nabla \cdot \mathbf{u} = 0$$

This leaves us with one set of equations that can be used to model both fluid domains and solid domains.

## 4

### 4.2. HEAT TRANSFER

The heat transfer consists of two parts; conduction and convection. The conduction part is not related to the fluid dynamics. While the convection part is directly related to the flow. The combination of conduction and convection is given by the energy equation:

$$\rho C_p \frac{\partial T}{\partial t} + \rho(C_p \mathbf{u}) \cdot \nabla T + f_T = k \nabla^2 T \quad (4.6)$$

Where  $\rho$  is the material density,  $C_p$  is the specific heat,  $T$  is the temperature,  $k$  is the thermal conductivity and  $f_T$  is a heat source term. The first term in this equation drops out because of the assumption of steady state heat transfer ( $\frac{\partial T}{\partial t} = 0$ ). This assumption will leave us with the following equation:

$$\rho(C_p \mathbf{u}) \cdot \nabla T + f_T = k \nabla^2 T \quad (4.7)$$

### 4.3. LITERATURE REVIEW

The work of relevant research is reviewed, starting with topology optimization of the single physics. And concluding with research done on similar multiphysics problems.

In the work of Gersborg-Hansen [3] et al. a Finite Volume Method (FVM) is used to optimize heat conduction problems. which is a follow up on the work of Bendsoe and Sigmund [21]. In the work of Gersborg-Hansen et al. a Solid Isotropic Material with Penalization (SIMP) rule is used together with the Method of Moving Asymptotes (MMA) to formulate the optimization part. The SIMP rule is applied to the thermal conductivity and is formulated as follows:

$$\check{\mathbf{k}} = \mathbf{s}(\gamma), \quad s_i(\gamma) = \gamma_{\min} + (1 - \gamma_{\min}) \gamma_i^p \quad (4.8)$$

Where  $\check{\mathbf{k}}$  is a vector with nodal conductivity values,  $\gamma$  is the design variable,  $\gamma_{\min}$  is a minimum value for the design variable and  $p$  is a penalization factor. The SIMP rule describes the relation between the thermal conductive material ( $\gamma = 1$ ) and the void material ( $\gamma = 0$ ). Gersborg-Hansen et al. uses two different objective functions that are minimized:

$$\Psi_1 = \int_{\Omega} f_T T, \quad \Psi_2 = \int_{\Omega} \nabla T \cdot (k \nabla T) \quad (4.9)$$

Where  $\Psi_2$  still has to be rewritten in order for the FVM to handle the gradients, for this derivation see the paper of Gersborg-Hansen et al. The approach used by Gersborg-Hansen et al. is similar to the one used in this research; the SIMP rule and the MMA solver will be used, the FVM will however not.

The MMA optimizer was first introduced by Svanberg [33] and is since then a widely used solver for topology optimization. The MMA optimizer generates an approximated subproblem for each iteration. The subproblem is mainly based on gradient information but also on the 'moving asymptotes', a set of parameters which are updated for each iteration. The unique optimal solution of the subproblem will be the next iteration point. This is repeated until the maximum allowed iterations are reached or until the solution is converged.

The work of Zhuang et al.[10] focuses on the topology optimization of heat conduction problems using a

level-set method. Zhuang et al. also uses different load cases, considering a design domain with different local temperatures. The objective minimized by Zhuang et al. is a summation of the different load cases:

$$\Psi = \sum_{k=1}^N w^k \int_{\Omega} |\nabla T^k(x)|^2 dx \quad (4.10)$$

Where  $k = 1, \dots, N$  represents the load case number,  $w^k$  is the weighting factor for the load case with  $\sum_{k=1}^N w^k = 1$  and  $0 \leq w^k \leq 1$  and  $T^k$  is the temperature for load case  $k$ . The big difference between the work of Zhuang et al. and Gersborg-Hansen et al. is the use of the level-set method instead of the MMA.

The level-set method was first introduced by Osher and Sethian [28]. The level-set method is used in topology optimization by representing an optimal boundary and changing the boundary under an appropriate velocity field. The level-set function  $\phi(x, t)$  is defined different for each region:

$$\begin{cases} \phi(x, t) > 0 & x \in \Omega, \\ \phi(x, t) < 0 & x \notin \Omega, \\ \phi(x, t) = 0 & x \in \partial\Omega = S(t), \end{cases} \quad (4.11)$$

With  $x \in \mathbb{R}^2$  and  $t \geq 0$ . This formulation represents the material properties of the design domain. with  $\phi(x, t) > 0$  representing conductive material,  $\phi(x, t) < 0$  representing void material and  $\phi(x, t) = 0$  representing the boundary. In Figure 4.1 an illustrative material region is shown. The shape sensitivities are used to update the level-set model,  $F_n(x)$  in the figure. The optimal solution is found when  $F_n(x)$  approximates zero.

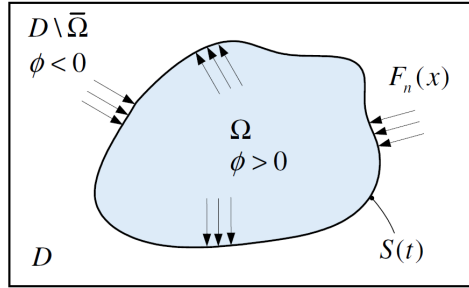


Figure 4.1: An illustration of an arbitrary material region represented by the level-set method, illustration from Zhuang et al. [10].

The level-set method does not require a SIMP formulation and therefore finds more discrete solutions than the MMA optimizer. It is however decided to not use the level-set method, the MMA solver is available within the commercial package used for this research.

The work of Gao et al.[35] focuses on design dependent heat loads. Gao et al. uses the the same objective as Gersborg-Hansen used,  $\Psi = \int_{\Omega} VT \cdot (k\nabla T)$ . In addition they added a SIMP rule for the heat load, which results in no heat load in the void material regions. Gao et al. uses a Bidirectional Evolutionary Structural Optimization (BESO) method as the optimizer. Which is based on the Evolutionary Structural Optimization (ESO) method introduced by Xie and Steven [41], extended to bidirectional (BESO) by Querin and Young [27] and Yang et al. [40][39]. The BESO method removes elements with high sensitivity values and replaces them with low sensitivity elements. The ESO/BESO methods are however difficult to use for multiphysics and multiple constraints problems. This makes the optimizer not preferred for this research.

Finally the work of Lohan et al.[19] uses a non-uniform heat load based on a PCA design. They use a MMA optimizer together with the SIMP rule to minimize different objectives. The additional aspect that Lohan et al. takes into account is a load case with multiple different local heat sources. The heat sources are based on components from a PCA, which is essentially the same as in this research. Lohan et al. also applies temperature constraints to the local heat sources while minimizing the thermal compliance ( $\Psi_1$  from Equation 4.9).

Borrvall and Petersson[34] first introduced topology optimization for fluid dynamics. They minimized the

power dissipation of a Stokes flow. They derived a generalized Stokes problem from a plane flow assumption (Coulette flow). A three-dimensional flow is reduced to a two-dimensional by assuming a flow between two plates. The distance between the two plates is a function of the design variable. This is implemented by introducing a damping term  $\alpha$  named the inverse permeability. The damping term is close to zero for fluid elements; the flow is represented by Stokes flow. And is large for solid elements; highly reducing the flow velocities. An interpolation scheme is suggested for the inverse permeability:

$$\alpha(\gamma) = \alpha_U + (\alpha_L - \alpha_U)\gamma \frac{1+q}{\gamma+q} \quad (4.12)$$

Where  $\gamma$  is the pseudo density,  $q$  is a penalization factor and  $\{\alpha_L, \alpha_U\}$  are respectively the lower and upper bounds. The same interpolation scheme for  $\alpha$  is used in this research, as described in section 4.1.

## 4

The work of Gersborg-Hansen et al.[4] extended the work of Borrvall and Petersson to nonlinear flow and higher Reynolds numbers. Gersborg-Hansen et al. showed the influence of the inertia term on the results found.

Guest and Prevost [16] described an alternative formulation for topology optimization of fluids, based on the one presented by Borvall and Petersson. Guest and Prevost suggested modeling the solid domains as a porous medium governed by Darcy's law. The flow equations are resembled by Brinkman's equation. Again using an interpolated inverse permeability to define a relation of the flow such that; for fluid domains the Stokes flow governs and for solid domains the Darcy flow governs. Allowing the velocities to be highly reduced in the solid domains. The formulation presented by Guest and Prevost will be used for this research.

Duan et al.[37] described a level-set method based topology optimization of a Navier-Stokes problem. Evgrafov's research [13] covered a topology optimization of compressible fluids. And Aege et al.[26] extended the application to large scale three-dimensional stoke flow problems. These works do not have a large relevance with this research.

There is also some research done on coupled thermal-fluid topology optimization. First the work of Dede[12] describes a multiphysics topology optimization for thermal-fluid systems using a COMSOL / MATLAB script. However the paper lacks details on the implementation and therefore it is hard to recreate. The work of Yoon[42] describes an optimization in which a convective heat transfer is used. Yoon minimizes the thermal compliance of the domain. The work of Koga et al. [18] describes the development of a heat sink using coupled thermal-fluid topology optimization. Koga uses a Stokes flow formulation together with the inverse permeability formulation stated in Equation 4.12. The objective function used in the work of Koga is a combination of temperature minimization and pressure drop minimization. The two are coupled by using weight coefficients and is formulated as follows:

$$\Psi = \nu \log(\Phi) + w \log(\Gamma) \quad (4.13)$$

The combined objective  $\Psi$  will be minimized. Where  $\Phi$  is the pressure drop objective,  $\Gamma$  is the heat dissipation objective and  $(\nu, w)$  are the weighted coefficients. A downside of using a formulation like this is that it is hard to determine which part of the objective is making the optimizer perform in a certain way. An alternative to this method is to introduce one of the objectives as a constraint. Next, the work of Yaji et al.[17] uses a level-set method to optimize the steady state Navier-Stokes and energy equations. The only research on non-uniform heat loads is the work of Qian and Dede[38]. They use heat dissipating tubes and use a tangential thermal gradient constraint on the boundaries of the tube. The same approach as in the work of Koga is used to formulate the objective function. For this research the coupled objective formulated by Koga will be used, also single objectives in combination with a temperature or pressure drop constraint will be evaluated.

### 4.4. TOPOLOGY OPTIMIZATION

It is decided to do the topology optimization with the commercially available software Comsol. The FEM model, described in Chapter 2, is also made in Comsol. The optimization will be described by a two dimensional analysis. A full three-dimensional optimization would be possible, however the third dimension adds a lot of computation time. Which makes it not feasible within the time-span of this research.

For this research a MMA solver will be used. The MMA solver is available within the optimization environment of Comsol. The optimization environment calculates the shape-sensitivities automatically, Comsol uses the adjoint method for this which is described in Appendix F.

For the formulation of the topology optimization a pseudo density,  $\gamma$ , is used to model the fluid and solid domain. This is approximated by allowing  $\gamma$  to take any value between  $\gamma = 0$  (solid) and  $\gamma = 1$  (fluid). The optimizer tries to find a distribution of  $\gamma$  for which the objective function is minimized. To prevent the optimizer from using 'grey values' the SIMP formulation is used. Grey values are intermediate values of  $\gamma$ . Mathematically this may be the best solution, however physically this makes no sense; it is neither solid nor fluid. SIMP is used for the following material parameters; thermal conductivity  $k$ , specific heat  $C_p$  and the density  $\rho$ . The following formulation is used:

$$\phi(\gamma) = \gamma^p \phi_{\text{fluid}} + (1 - \gamma^p) \phi_{\text{solid}} \quad (4.14)$$

Where  $\phi$  represents the material properties;  $k, C_p$  or  $\rho$ . The subscript solid and fluid indicates the material property of either solid or fluid domains. The term  $p$  is the penalization factor. For higher terms of  $p$  the relation between solid and fluid domains becomes more non linear. The differentiation between fluid and solid for the fluid dynamics is implemented in the physics by the using the inverse permeability to scale the flow between Darcy and Stokes flow. To prevent mesh dependent results and checkerboard patterns a PDE filter is used. The PDE filter is described in Appendix G.

4

## 4.5. UNIFORM HEAT LOAD

The first load case that will be investigated is a uniform heat load. An illustration of the design domain is given in Figure 4.2. On the inlet a parabolic velocity profile is subscribed with a maximum velocity of  $v_{\max} = 0.25 \text{ m s}^{-1}$ . A uniform heat load  $q = 175 \text{ kW m}^{-2}$  is present on the entire design domain. These values and the shape of the domain are taken from the work of Koga. The material properties for both fluid and solid are given in Table 4.1. Together with the corresponding values of the SIMP interpolation. Note that the relation for the density is linear. This is because both the specific heat and the density are in the first term of Equation 4.7. Picking a higher order relation for the density will cause the first term to be penalized twice.

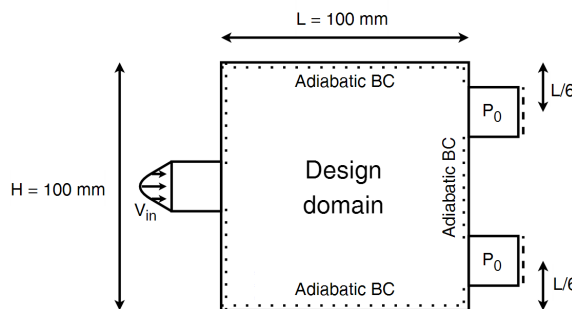


Figure 4.2: The design domain of the uniform heat load topology optimization. The dotted lines have an adiabatic boundary condition, on the dashed line a zero pressure boundary condition is present.

Table 4.1: The material properties that are used for the uniform heat load problem.

| Material | $k [\text{W m}^{-1} \text{K}^{-1}]$ | $C_p [\text{J kg}^{-1} \text{K}^{-1}]$ | $\rho [\text{kg m}^{-3}]$ | $\mu [\text{N s m}^{-2}]$ |
|----------|-------------------------------------|--|---------------------------|---------------------------|
| Water    | 0.61                                | 4180                                   | 1000                      | 0.001                     |
| Steel    | 15                                  | 500                                    | 7900                      | -                         |
| $p$      | 4                                   | 4                                      | 1                         | -                         |

### 4.5.1. MULTI OBJECTIVE MINIMIZATION

The first objective function that will be used for the optimization is the multi-objective from Equation 4.13. Within Comsol it is possible to take the average or integral on either a domain or a boundary as an objective function. For the temperature the average temperature of the design domain is taken. For the pressure drop, the integral of the pressure on the inlet minus the pressure on the outlet is taken. Which results in:

$$\Phi_c = \int_{\Omega_{in}} P d\Omega_{in} - \int_{\Omega_{out}} P d\Omega_{out} \quad (4.15)$$

$$\Gamma_c = \frac{1}{nm} \left( \sum_{i=1}^n \sum_{j=1}^m T_{ij} \right) \quad (4.16)$$

Where  $\Phi_c$  is the Comsol pressure drop objective and  $\Gamma_c$  is the Comsol temperature objective, if we insert these in Equation 4.13 the multi objective becomes:

$$\Psi_c = v \log(\Phi_c) + w \log(\Gamma_c) \quad (4.17)$$

The complete optimization can be formulated as follows:

$$\begin{aligned} & \underset{\gamma}{\text{minimize}} \quad \Psi_c(\gamma) \\ & \text{subject to} \quad \rho(C_p \mathbf{u}) \cdot \nabla T + f_T = k \nabla^2 T \\ & \quad \mu \nabla^2 \mathbf{u} + \alpha \mathbf{u} = \nabla p - \mathbf{f} \\ & \quad \nabla \cdot \mathbf{u} = 0 \\ & \quad 0 \leq \gamma \leq 1 \\ & \quad \int_{\Omega} \gamma d\Omega \leq V \end{aligned} \quad (4.18)$$

Where  $V$  is a volume constraint, defined as  $V = 0.4$ . With  $v$  and  $w$  the ratio between pressure drop and temperature minimization can be adjusted. For  $v \gg w$  the multi-objective becomes approximately a pressure drop minimization, while for  $w \gg v$  a temperature minimization. The results for different values of  $v$  and  $w$  are shown in Figure 4.3, where red corresponds with water ( $\gamma = 1$ ) and blue with steel ( $\gamma = 0$ ). For combinations where  $\frac{v}{w}$  is high, the emphasis is on the pressure drop minimization; few smaller channels are shown. And where  $\frac{v}{w}$  is lower the emphasis is on the temperature minimization; smaller channels are shown. The asymmetric designs are most likely a result of the asymmetry in the used, non regular mesh of triangular elements.

In Figure 4.4 the velocity and the temperature plots of the result for  $v = 1$  and  $w = 5$  are shown. Both results corresponds with what we would expect. The temperature is lower on the fluid areas and the velocity follows the channels.

### 4.5.2. PRESSURE DROP MINIMIZATION

Instead of implementing both the pressure drop and the temperature in a single objective we can also set one as a constraint and the other as objective. First a constraint is set on the temperature and the pressure drop is minimized. The temperature constraint is set to 450 K, this value is based on the result found for the multi objective with  $v = 1$  and  $w = 5$ .

The result for this optimization problem is shown in Figure 4.5. The result is similar to the  $v = 1$  and  $w = 5$  result, which is expected since the constraint is derived from it. The pressure drop minimization shows however a more converged result with less grey values.

The big difference is the convergence of the objectives. The pressure drop plotted against the iteration number is shown in Figure 4.6a and 4.6b for respectively the pressure drop minimization and the multi objective. There is a clear difference between the two; the convergence of the multi objective is quite smooth, while the convergence of the pressure drop minimization first goes down but then goes up again. This is because the solver first tries to satisfy the temperature constraint and when the constraint is satisfied the solver minimizes the objective. This is also seen in the temperature convergence shown in the figures 4.6c and 4.6d. One

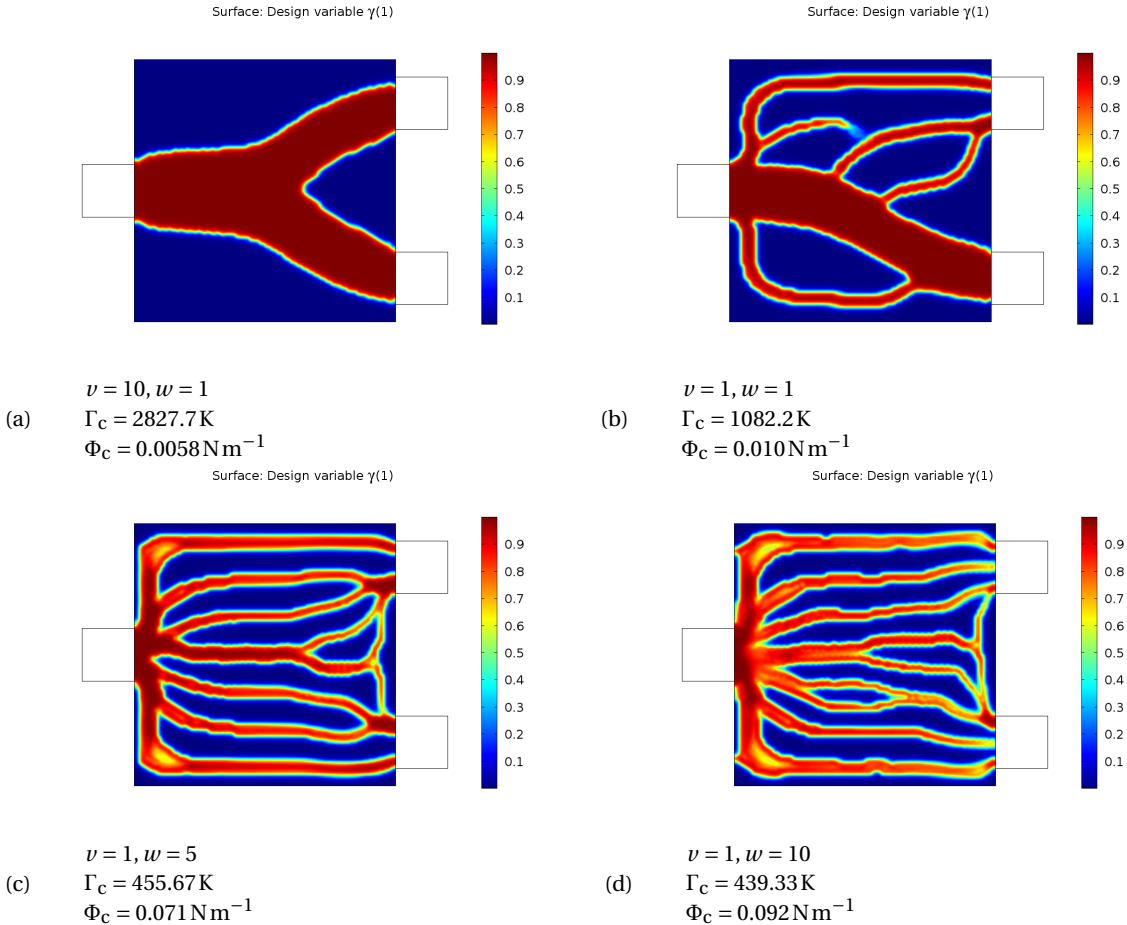


Figure 4.3: Results of the topology optimization for the multi objective. The value of  $\gamma$  is shown, the red area represents  $\gamma = 1$  which corresponds to water and the blue areas represent  $\gamma = 0$  which corresponds to steel.

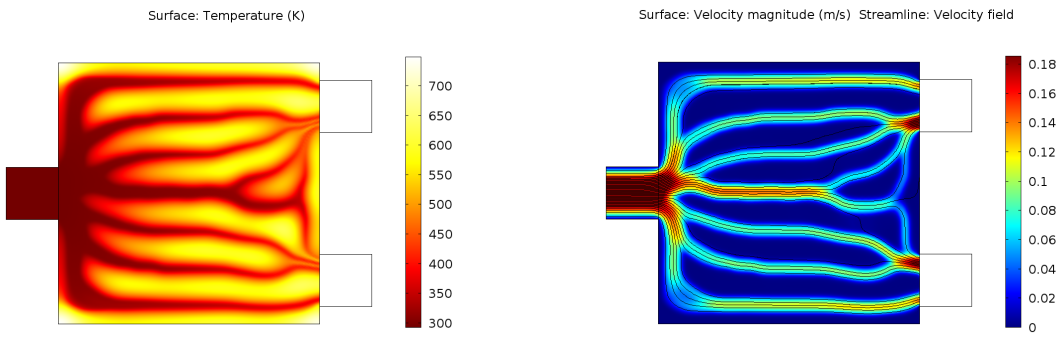


Figure 4.4: The temperature and velocity field for the optimized result with  $v = 1$  and  $w = 5$ . Figure 4.4a shows the temperature field and 4.4b shows the velocity field.

can see that the temperature goes down to 450 K after only a few iterations, after that the temperature stays approximately constant around 450 K.

The convergence of the volume fraction  $V$  is seen in Figure 4.6e. The volume fraction was constraint at  $V \leq 0.4$ , however this constraint is never satisfied during the optimization. Which indicates that the temperature constraint is probably too strict for the allowed water volume.

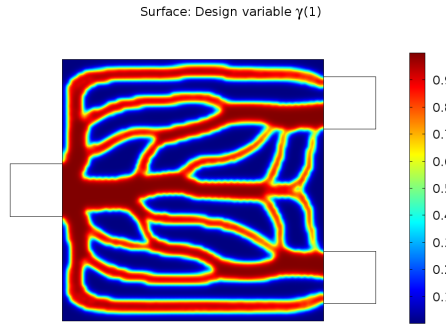


Figure 4.5: The result of the topology optimization for pressure drop minimization with a constraint on the temperature ( $\Gamma_c \leq 450\text{ K}$ ). The pseudo density  $\gamma$  is shown, red is  $\gamma = 1$  which corresponds with water and blue is  $\gamma = 0$  which corresponds with steel.

4

#### 4.5.3. TEMPERATURE MINIMIZATION

For the temperature minimization formulation the pressure drop is set as a constraint. The maximum allowed pressure drop is  $\Phi_c \leq 0.05\text{ N m}^{-1}$ . In Figure 4.7 the result is shown for the temperature minimization. The result is very similar to that of the pressure drop minimization, which is expected since the pressure drop constraint is the same as the previously found pressure drop. The main difference is again in the way the solver gets to the solution. The convergence plots, shown in Figure 4.8, show a weird behavior; the temperature and the pressure both go down in the first iterations but then, the temperature only increases. This while the temperature is minimized. The reason for this is the volume constraint, the convergence of the volume constraint shows that for the first iterations the used volume increases heavily and then goes down gradually. The increase in temperature is because the solver keeps using less water volume. Just like the pressure drop minimization the volume constraint is not satisfied, this indicates that this constraint is also too strict.

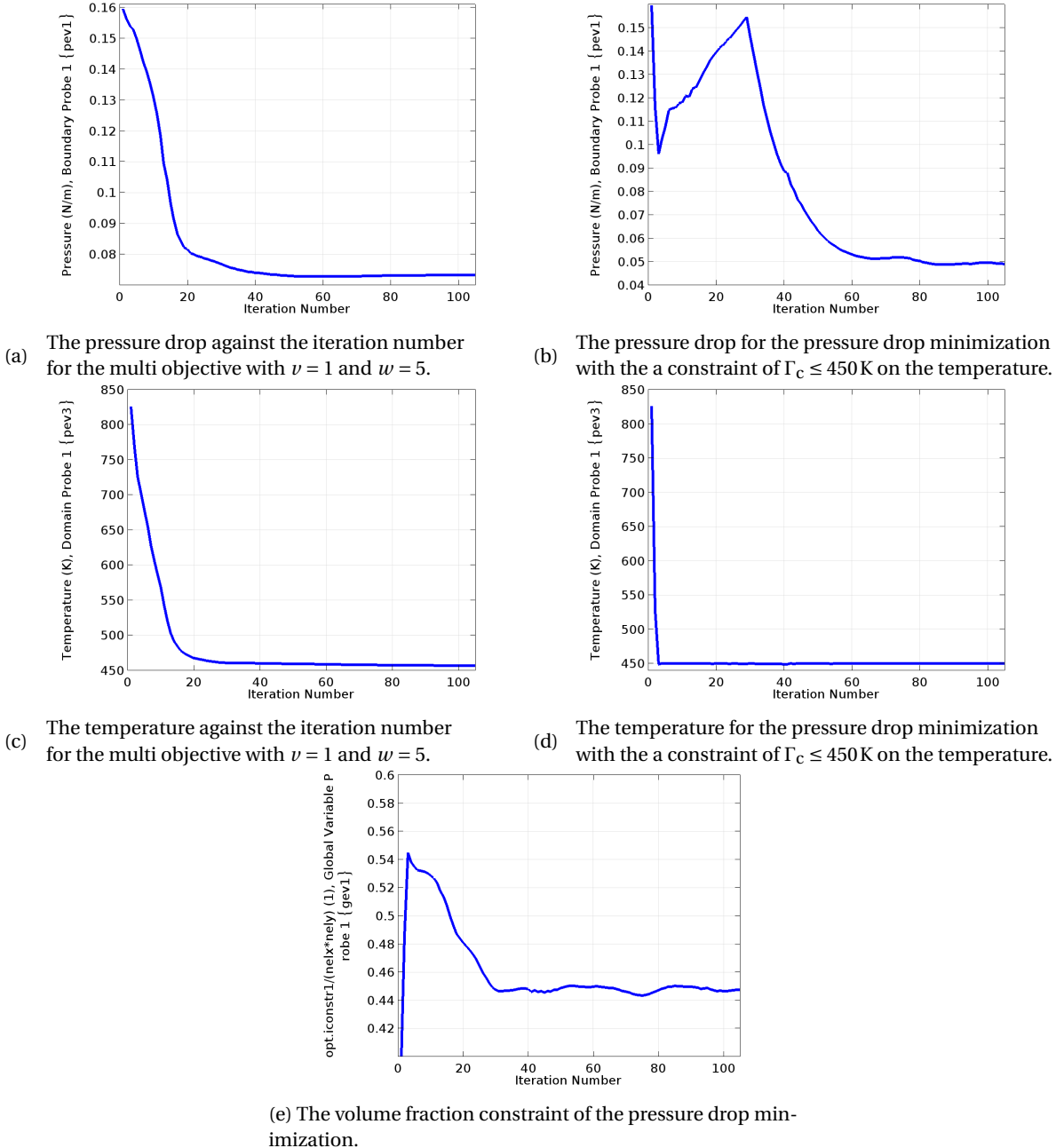


Figure 4.6: The convergence plots of the multi objective and the pressure drop minimization.

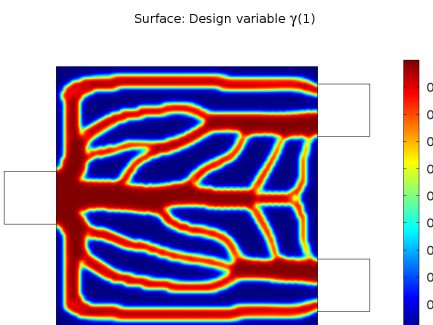


Figure 4.7: The optimized pseudo density  $\gamma$  layout for the temperature minimization with a constraint on the pressure drop.

4

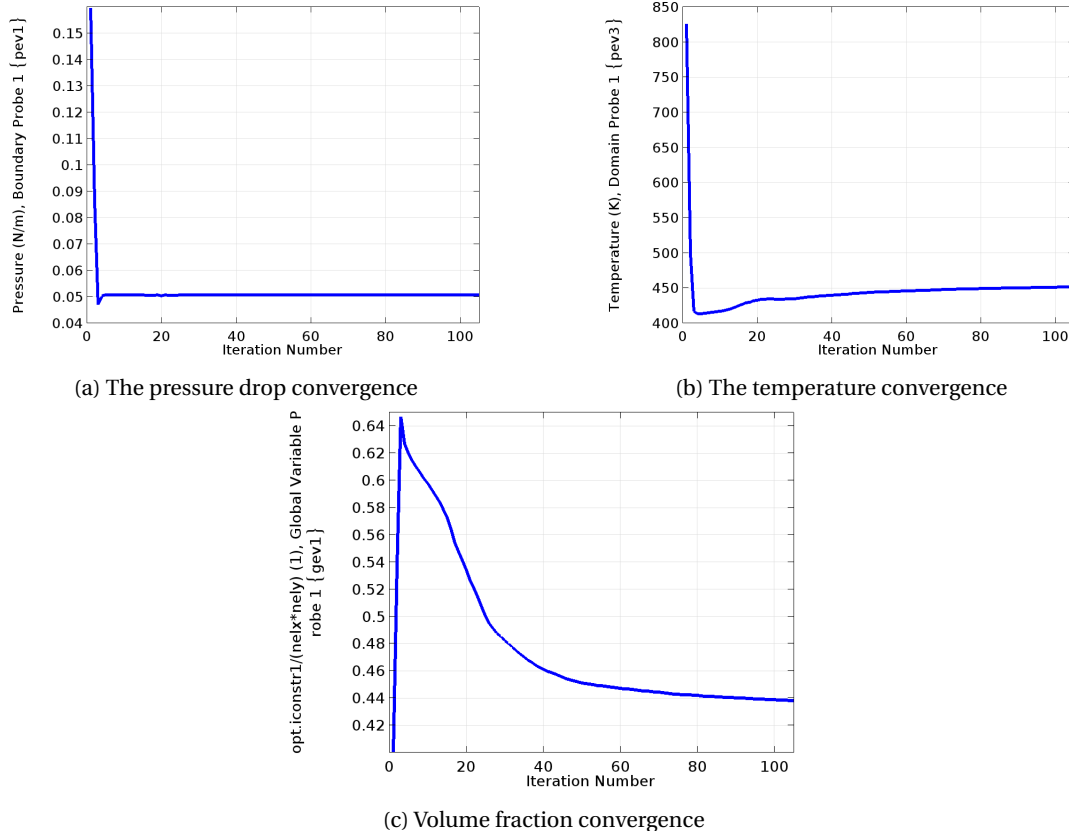
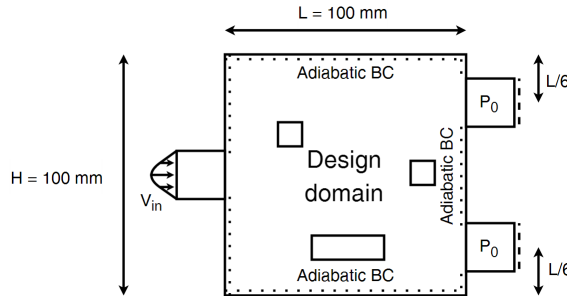


Figure 4.8: The convergence plots of the temperature minimization with a constraint of  $\Phi_c \leq 0.05 \text{ N m}^{-1}$  on the pressure drop.

## 4.6. NON UNIFORM HEAT LOAD

The same design domain as used for the uniform heat load is used for the non uniform heat load. In the design domain three local hot spots areas are added, the main area of the design domain has a heat load  $q^*$  and the local hot spot areas have a heat load  $q$ . Where  $q$  is the heat load used in the uniform case and  $q^* = \frac{1}{10}q$ . All other parameters are kept the same as in the uniform heat load case. The design domain including the local hot spots is shown in Figure 4.9.

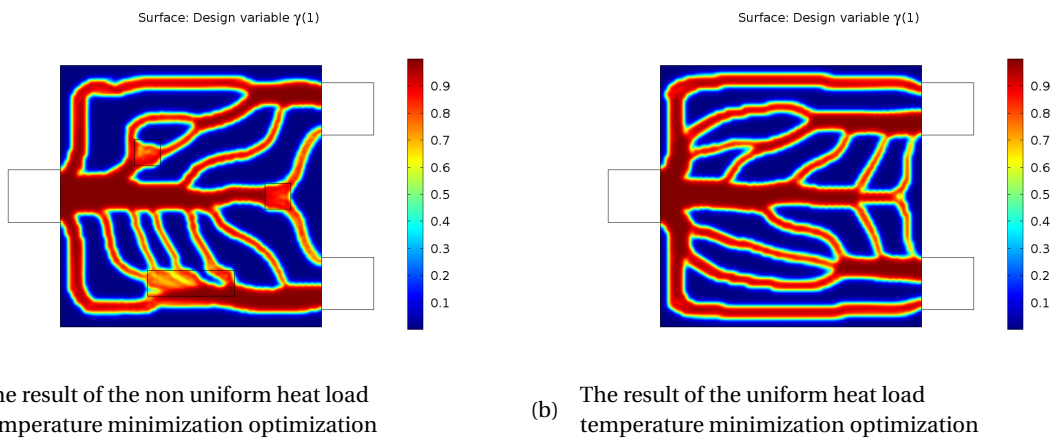


4

Figure 4.9: The design domain of the non uniform heat load topology optimization. The dotted lines have an adiabatic boundary condition, on the dashed line a zero pressure boundary condition is present.

For the temperature minimization the same constraint on the pressure drop as for the uniform heat load is used;  $\Phi_c \leq 0.05 \text{ Nm}^{-1}$ . The result is shown in Figure 4.10 together with the result of the uniform heat load. A clear difference is seen; the non uniform heat load shows more channels towards the hot spots, but also channels on the non hot spot area. To see the effect of the heat load on the non hot spot area the optimization is also done with only a heat load on the hot spots. This result is shown in Figure 4.11. We see that for this result the channels only cover the hot spot area and no other channels are formed. The two results give a good indication that the model works as expected.

The multi objective and pressure drop minimization can also be used to optimize the non uniform heat load. For the multi objective it is figuring out which combination of  $v$  and  $w$  yields the best result. This is the same approach as for the uniform heat load. More interesting is however the pressure drop minimization. The temperature constraint can now be set on four different domains; each hot spot and the remaining domain. By using this formulation a higher priority can be given to a certain hot spot. Or a maximum allowed temperature from a design load case can be given to a hot spot. In Figure 4.12 the results for different temperature constraints are shown together with the used constraints. One can see that different constraints yield different results, by setting one of the constraint sharper; the emphasis can be set on that hot spot. The constraints



(a) The result of the non uniform heat load temperature minimization optimization

(b) The result of the uniform heat load temperature minimization optimization

Figure 4.10: The optimization results of both the uniform and non uniform heat load cases. For the non uniform load more channels go over and towards the local hot spots.

in Figure 4.12a are approximately the same as the temperatures found for the temperature minimization. A similar result is found for the two optimization problems. Figure 4.12b shows the result for a load case where only the constraint on the right hot spot is strict, the other domains are allowed to have a high temperature. The result is a large flow over the right component and some small channels over the other hot spots. The same is done for Figure 4.12d but for the bottom hot spot. The optimization problem corresponding to Figure 4.12c has overall more stricter constraints, but the top hot spot is constraint rather strict. The result is a larger channel over the top hot spot but also multiple channels over the remaining domain. The result is however less converged than the other results.

4

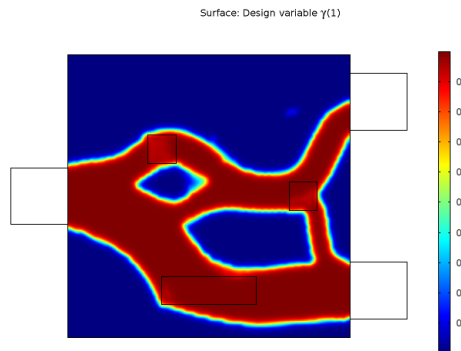


Figure 4.11: The result of the optimization for temperature minimization with only a heat load on the hot spots.

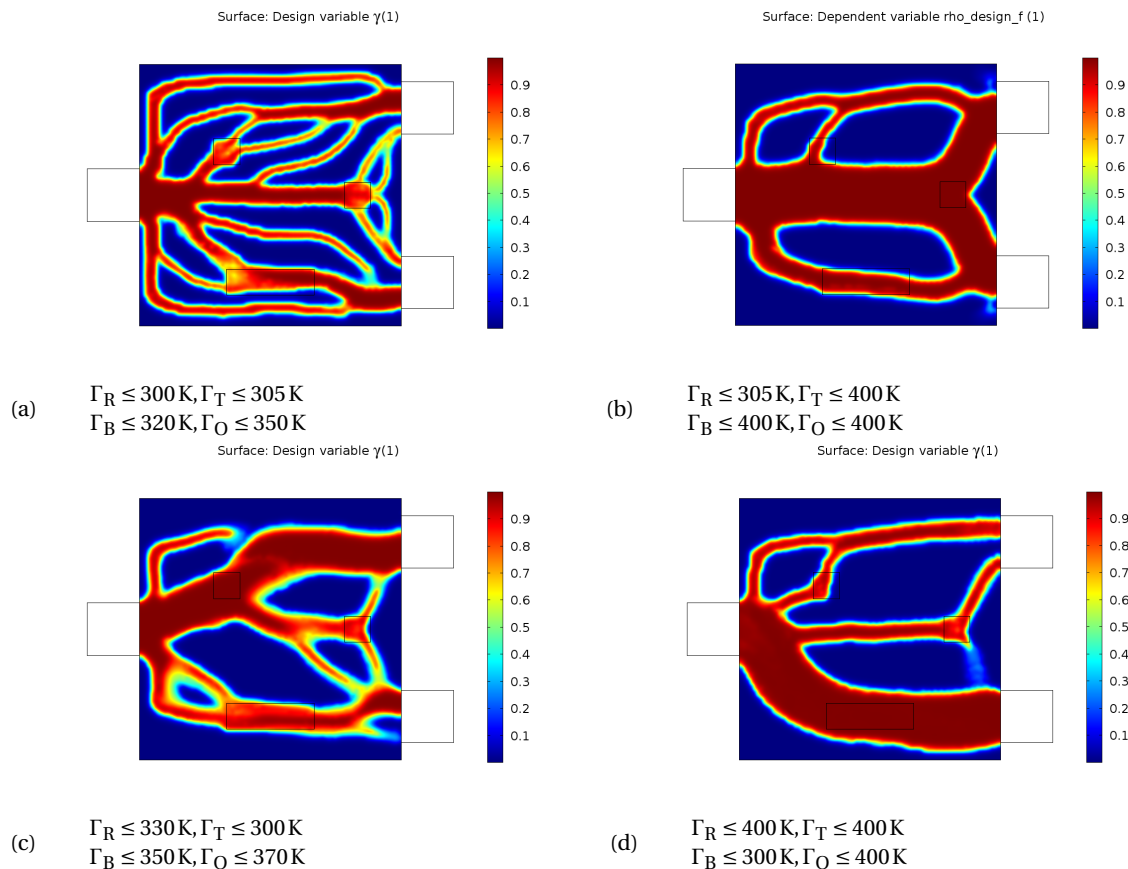


Figure 4.12: The results of the topology optimization for pressure drop minimization with different constraints on the hot spots and the non hot spot area.  $\Gamma_R$  represents the average temperature of the hot spot on the right side,  $\Gamma_T$  for the hot spot on the top side,  $\Gamma_B$  for the hot spot on the bottom and  $\Gamma_O$  for the non hot spot area.

## 4.7. CONCLUSION

This chapter describes a formulation of a topology optimization for heat transfer and fluid dynamics. The formulation that is described will be used for the optimization of the design load from the lean E-box. A comment is given on the difference in convergence between three objective functions. From which we concluded that the multi objective converges more gradually than the single objectives. But results found by the single objectives are more converged.

The influence of local hot spots is also presented. The results found for the optimization of the design domain with the hot spots included indicate that the optimizer behaves as expected.



# 5

## TOPOLOGY OPTIMIZATION OF THE DESIGN LOAD

In Chapter 4 topology optimization is applied for an arbitrary non-uniform heat load. In this chapter the arbitrary heat load will be replaced with the heat load of the lean E-box.

### 5.1. SETTING UP THE OPTIMIZATION

The heat load from the lean E-box is derived from the three-dimensional FEM model, where the temperature of total water domain is set constant at  $T = 22^\circ\text{C}$ , this results in the most ideal situation. At the water interface a continues heat load is derived by using an interpolation function, shown in Figure 5.1. Where 5.1a is derived from the prototype and 5.1b from the concept design. Since the measurement facilities do not allow measuring in a vacuum, the atmospheric heat load is optimized. A comment is given on the optimization of the vacuum heat load in Appendix H.

A two-dimensional design domain is considered, with the same size as the water interface that is used in the baseline design discussed in Chapter 2.5. The design domain is illustrated in Figure 5.2. The prescribed flow on the inlet is  $0.11\text{min}^{-1}$  and the outlet is preset with  $P = 0\text{Pa}$ . A low flow rate is chosen because for lower flow rates the water channel position has the largest influence on the heat transfer. For high flow rates the water has much more cooling power and therefore the position of the water channel may show a smaller influence on the objective, because it is already cooled heavily.

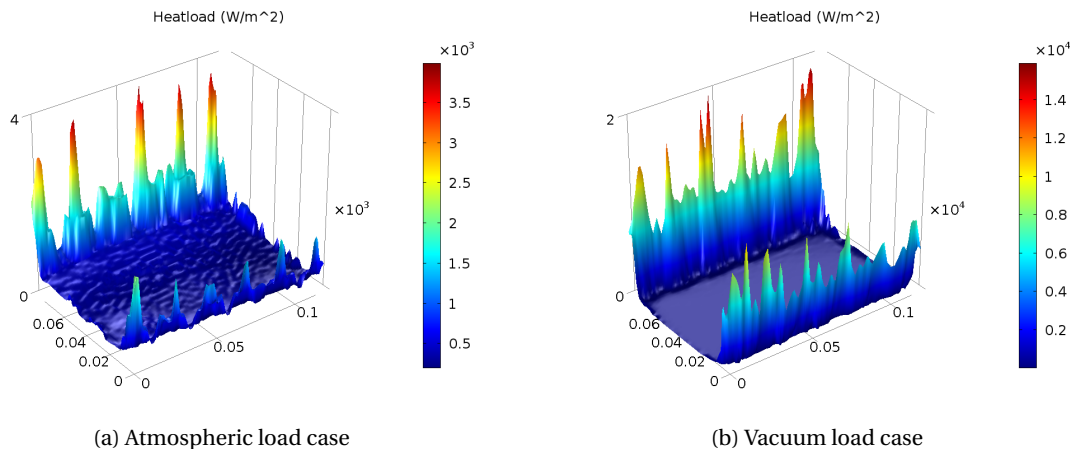


Figure 5.1: The heat loads derived for the two different load cases of the lean E-box. The horizontal axes indicate the dimensions of the domain in m and the vertical axis indicates the heat load in  $\text{Wm}^{-2}$ .

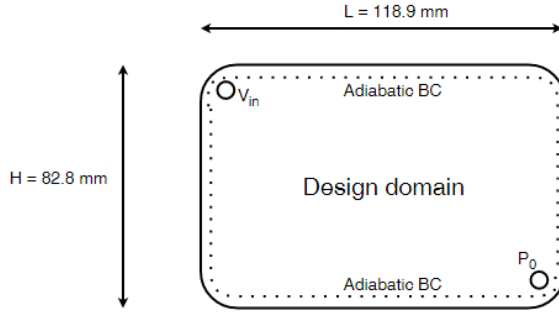


Figure 5.2: The design domain of the lean E-box optimization. The dotted line represent an adiabatic boundary condition, the circle on the top left is the water inlet and the one on the bottom right is the outlet. On the inlet a prescribed flow of  $0.11 \text{ min}^{-1}$  is present and the outlet has a zero pressure boundary condition

## 5

### 5.2. TOPOLOGY OPTIMIZATION

It is decided to not use the multi objective and only focus on the single objectives. The single objectives showed more converged results. The same objectives are considered as shown in Equation 4.16 and 4.15, although it would be desired to use the component temperatures of the SSB as an objective. This however requires to add the entire three-dimensional model of the lean E-box to the optimization. Resulting in a dramatic increase in computation time. Therefore it is decided to stick to the previously mentioned objectives.

Multiple values for the constraints are considered, the results are compared and a performance measurement is done. The performance is measured by converting the optimization result to a three-dimensional design, which is imported in the FEM model. The temperature is evaluated at the measurement points discussed in chapter 3.1. These are compared with the temperatures evaluated at the same points for the FEM model with constant water temperature. This gives an indication of the performance with respect to the most ideal situation.

In Figure 5.3 and 5.4 the results for the different constraints are shown. For the pressure drop minimization with a constraint of  $\Gamma_c \leq 293.5 \text{ K}$  the results are almost completely red. This is because the constraint is too strict; the solver can not find a good solution for this constraint. For the temperature minimization the results are less converged than the pressure drop minimization. One reason for this can be that it takes more iterations for the temperature minimization to converge. All optimizations are stopped at 100 iterations, if the solver needs more iterations for the temperature minimization to converge we find less converged results.

Because the temperature minimization shows less converged results it is decided to continue with the results from the pressure drop minimization, from which only the converged results are compared with the ideal situation. The average of the differences in temperature for all measurement points is taken, and plotted in Figure 5.5. The design with the lowest average difference is the best performing. Which is for  $\Gamma_c \leq 293.75 \text{ K}$  and  $V = 0.7$ . Note that a lower  $\Gamma_c$  does not mean a better performance, this has to do with the locations of the measured components.

The design that corresponds with  $V = 0.7$  and  $\Gamma_c \leq 293.75 \text{ K}$  is shown in Figure 5.6, together with the velocity field and the temperature field.

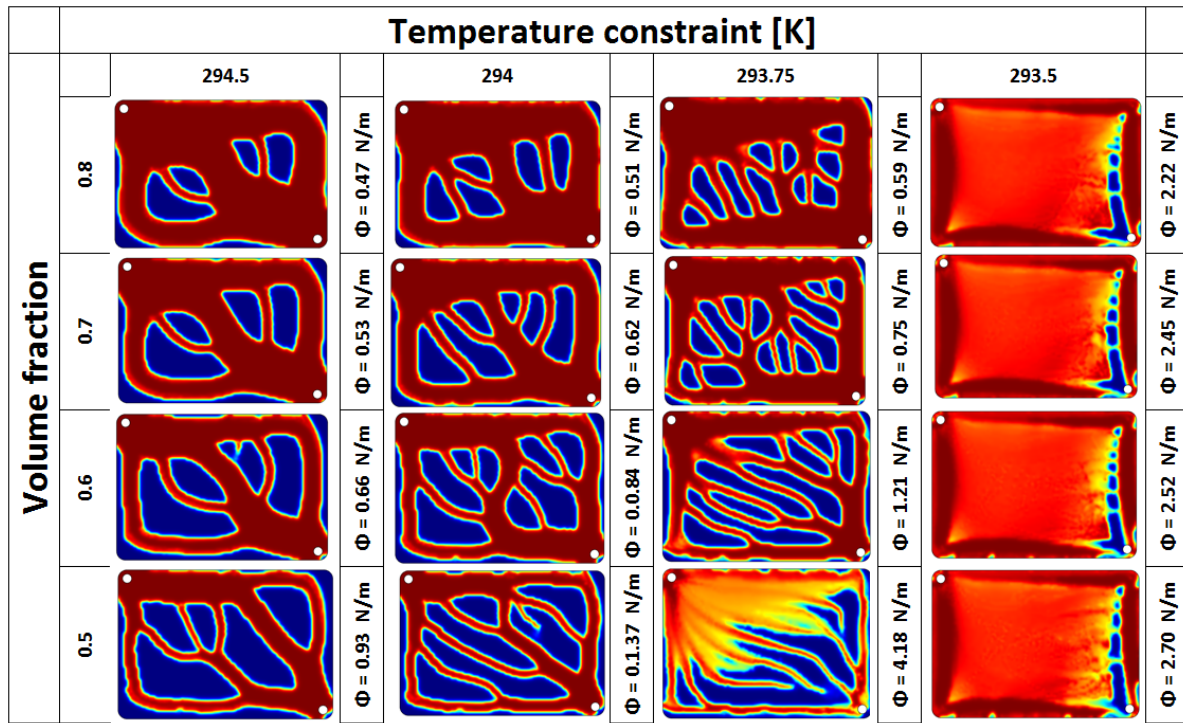


Figure 5.3: Comparison overview of the results from the pressure drop minimization. The volume fraction is shown on the vertical axis and the temperature constraint is shown on the horizontal axis. On the right side of the results the value for the pressure drop objective is shown.

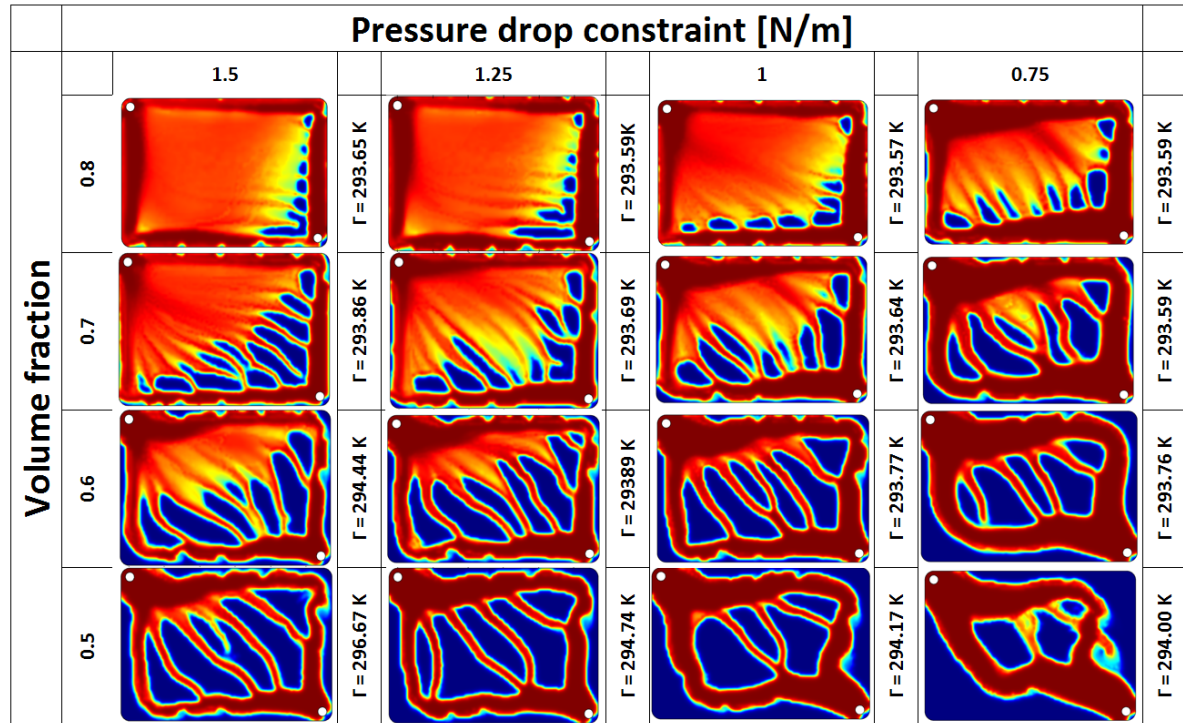


Figure 5.4: Comparison overview of the results from the temperature minimization. The volume fraction is shown on the vertical axis and the pressure drop constraint is shown on the horizontal axis. On the right side of the results the value for the temperature objective is shown.

5

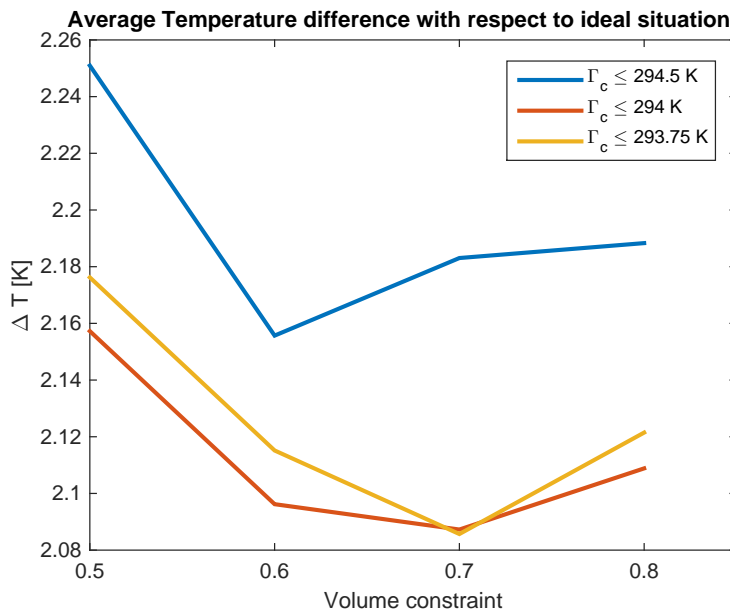


Figure 5.5: A comparison between the performance of the results from the pressure drop minimization. The average temperature difference between the ideal case and the optimized design is shown on the vertical axis. The used volume fraction is shown on the horizontal axis. A lower  $\Delta T$  means a better performance.

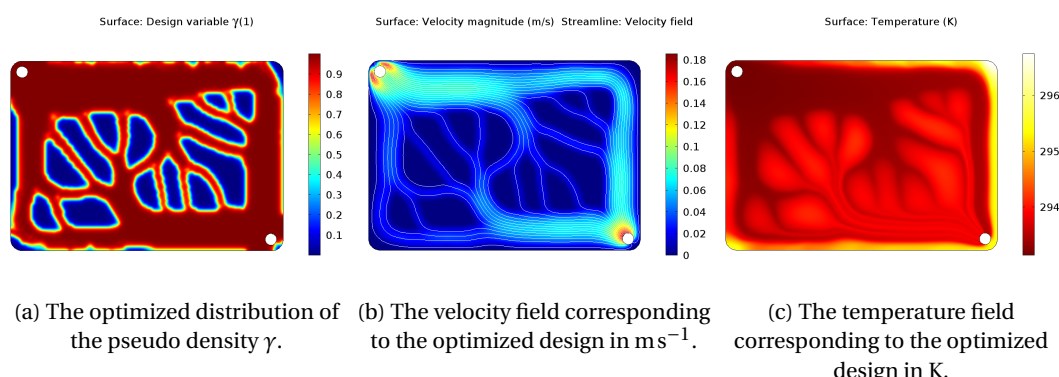


Figure 5.6: The optimized layout for the pressure drop minimization with a volume constraint of  $V = 0.7$  and a temperature constraint of  $\Gamma_c = 293.75 \text{ K}$ . Together with the corresponding velocity field and the temperature field.

### 5.3. VARIATION OF THE WATER INLET AND OUTLET

It is not so straight forward to implement the inlet and outlet position as a design variable in the topology optimization. Therefore it is decided to only evaluate some combinations and comment on the performance. For these evaluations it is assumed that the best performing constraint values found in the previous section are also optimal for the different input and output positions.

The results from the different optimizations are shown in Figure 5.7, in each result the considered inlet (green) and outlet (red) is indicated. In Table 5.1 the  $\Delta T_{\text{ideal}}$  column shows the performance with respect to the ideal situation. The table also shows a different performance measurement;  $\Delta T_{\text{baseline}}$  gives a performance measurement with respect to the baseline design considering the same inlet and outlet positions. With the baseline design being the open water channel as used in the prototype of the lean E-box.

In this research we aim to give a validation of a performance increase by doing a topology optimization. For the validation  $\Delta T_{\text{baseline}}$  is important, since we can not measure the ideal situation. Also comparing measurements for a baseline and an optimized design with different inlet and outlet positions gives no good indication of the performance increase by the optimization. This makes  $\Delta T_{\text{baseline}}$  the best performance measurement to decide which design is manufactured.

5

No baseline performance measurement is done for design  $D_7$  and  $D_8$ . The inlet and outlet positions of these designs are placed in such manner that the baseline design would show a very bad performance. Therefore  $\Delta T_{\text{baseline}}$  would not give a fair indication.

Design  $D_2$  shows the best performance with respect to the ideal situation, and therefore is considered the 'optimal' design. However design  $D_5$  shows the biggest performance increase with respect to the corresponding baseline design. Overall the performance increases are rather small. To increase the chances of measuring the performance increase it is decided to manufacture design  $D_5$ . The performance with respect to the baseline design is the value that we can measure, the relation to the ideal situation is not measurable.

Table 5.1: The performances of the optimized design for different inlet and outlet positions.

| Design | $\Delta T_{\text{ideal}}$ [K] | $\Delta T_{\text{baseline}}$ [K] |
|--------|-------------------------------|----------------------------------|
| $D_1$  | 2.086                         | -0.224                           |
| $D_2$  | 1.920                         | -0.208                           |
| $D_3$  | 1.984                         | -0.222                           |
| $D_4$  | 2.043                         | -0.075                           |
| $D_5$  | 2.267                         | -0.249                           |
| $D_6$  | 2.089                         | -0.240                           |
| $D_7$  | 2.654                         | [ $-$ ]                          |
| $D_8$  | 2.577                         | [ $-$ ]                          |

### 5.4. THE PROTOTYPE AND PERFORMANCE MEASUREMENTS

The prototype of design  $D_5$  is manufactured by assuming a uniform thickness of the channels. The channels are sealed by a see through plate. This way the flow can be seen during the measurements. The prototype is shown in Figure 5.8.

For the measurements the same measurement setup is used as described in section 3.1. The measurement procedure is mostly the same, however for this measurement only one connection configuration is used and only one flow rate; 12 bolts and  $0.11 \text{ min}^{-1}$ . Also the gap filler pad is not used for this measurement. The measurement will be done for the baseline and the optimized coolplate.

To compare the performance of the optimized design, the temperature difference between the optimized and the baseline design is taken. These values are compared with the predicted performance increase. The measurement is repeated multiple times to check if the performance is consistent. In figures 5.9, 5.10, 5.11 and 5.12 four measurement results are shown together with the FEM results. On the horizontal axis the ther-

5

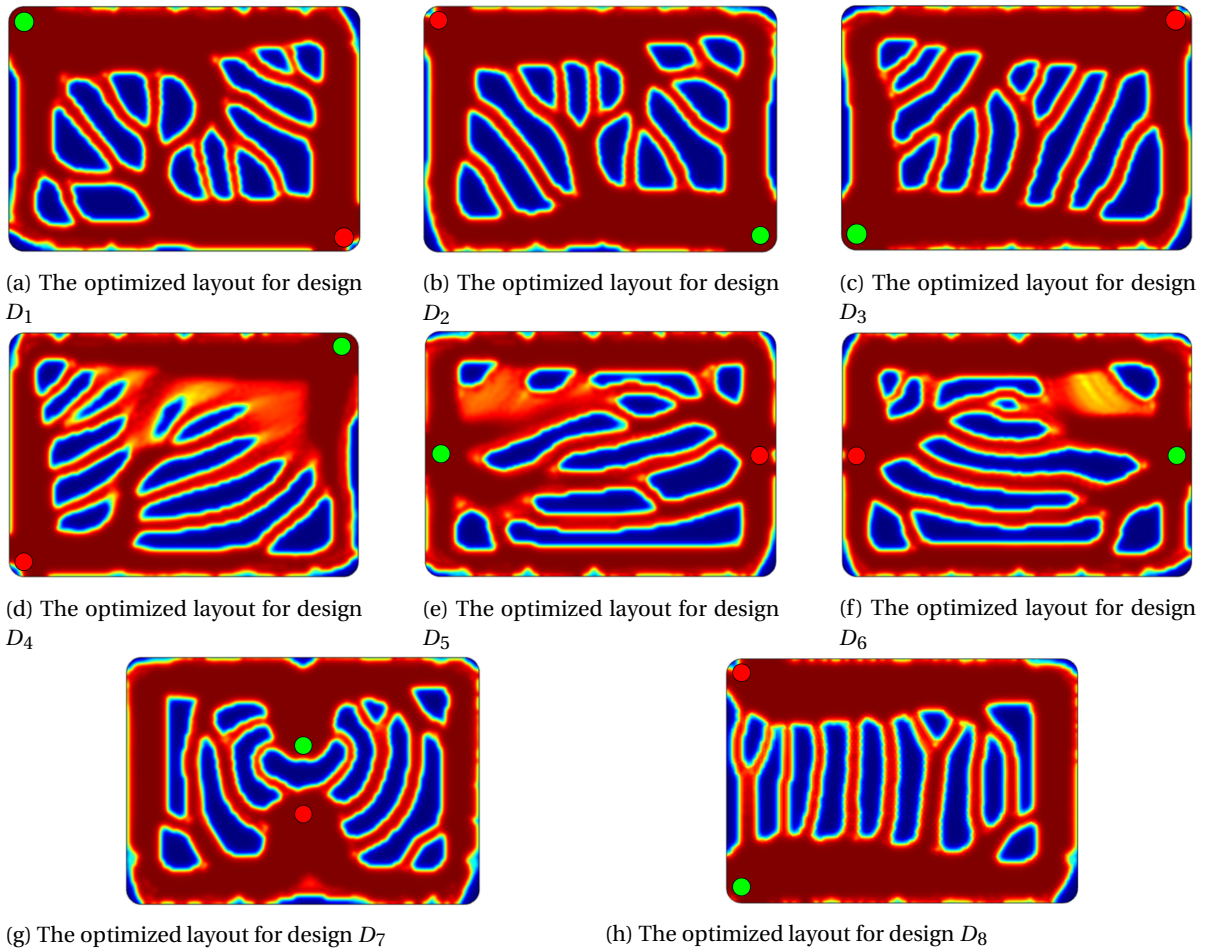


Figure 5.7: The designs yielded by the topology optimization for the different input and output positions. The images show the distribution of the pseudo density  $\gamma$ , red means  $\gamma = 1$  that corresponds with water and the blue corresponds with  $\gamma = 0$  that corresponds with steel. All the results are for the same objective and constraints. The inlet is indicated with a green circle and the outlet with a red circle.

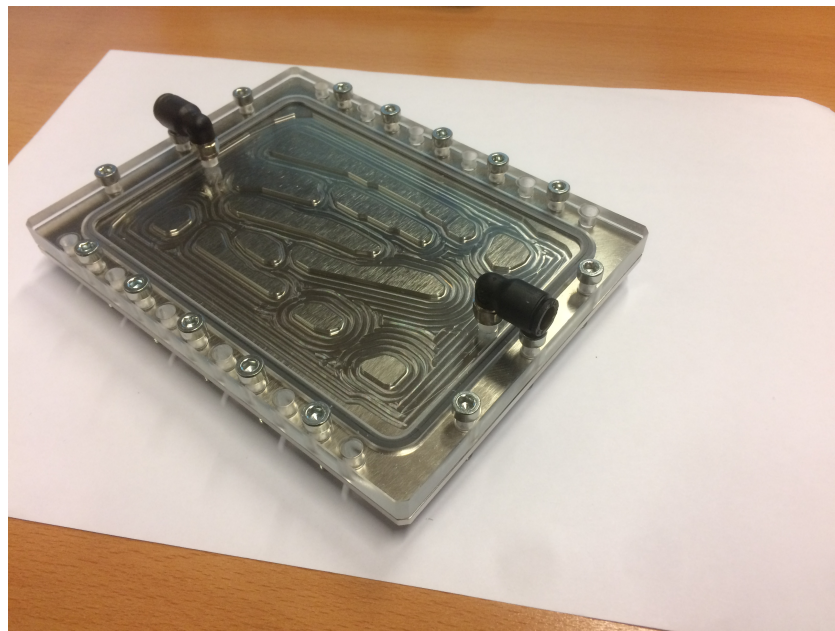


Figure 5.8: The assembled prototype of the optimized design. Through the clear top part the optimized cooling channels are seen.

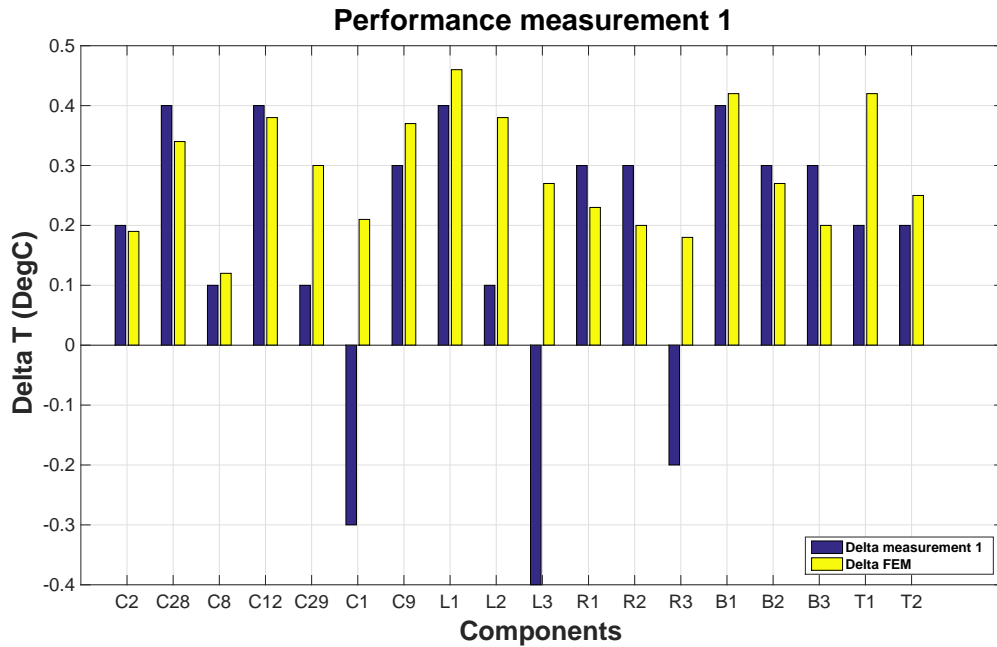


Figure 5.9: The temperature difference for each measurement point between the baseline design and the optimized design from the first measurement. The measured difference and the difference from the FEM model are shown. All results are for a flow of approximately  $0.1 \text{ lmin}^{-1}$

mocouple positions are shown, these correspond with the ones stated in Table A.1 and Figure 3.3. On the vertical axis the temperature difference between the baseline and the optimized coolplate are shown, hence a positive value means an increase in performance.

When we look at the results found for the different measurements we see that for each measurement different results are found. Measurement 1 shows a good match with the FEM results. But measurement 2 shows no match at all, for measurement 2 the optimized design performance worse than the baseline design. Measurement 3 shows a slightly better match and measurement 4 shows a higher performance increase than predicted.

A likely cause for the different results found is that the order of magnitude of the performance increase is within the measurement error. The measurement equipment displays the temperature in one digit after the decimal. This is the same order of magnitude as the predicted performance increase. This makes it error sensitive.

The biggest measurement error is however found for the amount of flow. As discussed in chapter 3.1 the thermal control unit that is used does not have a flow regulation option. So the amount of flow is measured manually. A human error is made with ease and thus an error in the amount of flow is likely. A small error in the amount of flow will result in a deviation of the temperature difference, which is illustrated in Figure 3.6. Also the measurements are done two times; for the baseline and the optimized coolplate. This means that the measurement error is found twice, which doubles the total error.

## 5.5. THE INFLUENCE OF THE STOKES FLOW ASSUMPTION

The biggest assumption in the fluid dynamics is that the inertial forces are much smaller than the viscous forces. Which allows the use of stokes flow instead of the full Navier-Stokes flow. The mathematical difference between Stokes flow and Navier-Stokes flow is the addition of the first term in the following equation:

$$\rho(\mathbf{u} \cdot \nabla \mathbf{u}) - \mu \nabla^2 \mathbf{u} = -\nabla p + \mathbf{f}$$

Where  $\rho$  is the material density,  $\mathbf{u}$  is the velocity vector,  $\mu$  is the dynamic viscosity,  $p$  is the pressure and  $\mathbf{f}$  is the force vector.

5

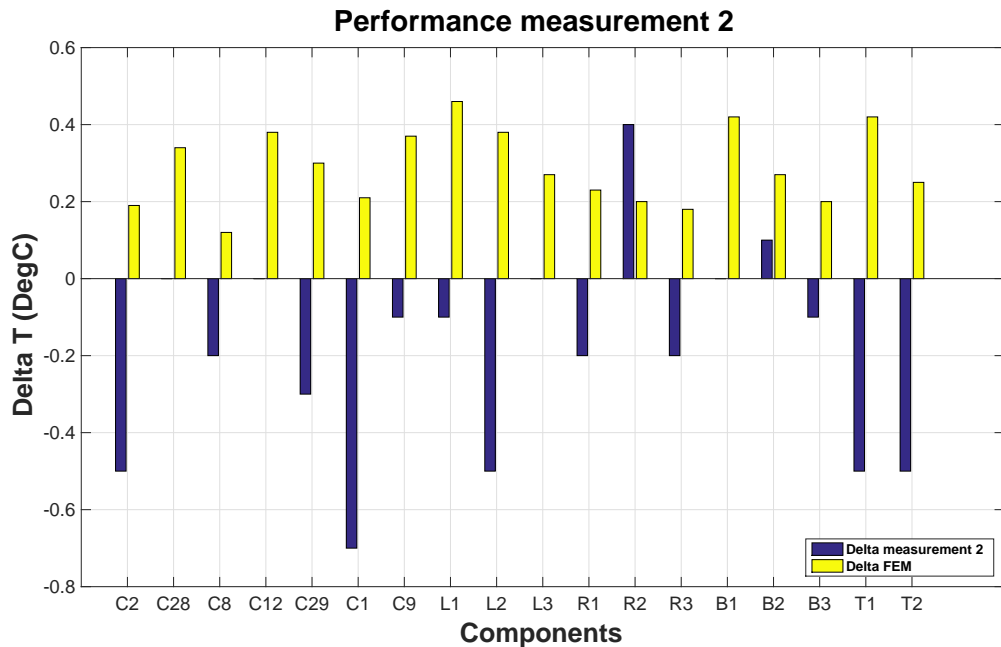


Figure 5.10: The temperature difference for each measurement point between the baseline design and the optimized design from the second measurement. The measured difference and the difference from the FEM model are shown. All results are for a flow of approximately  $0.1 \text{ lmin}^{-1}$

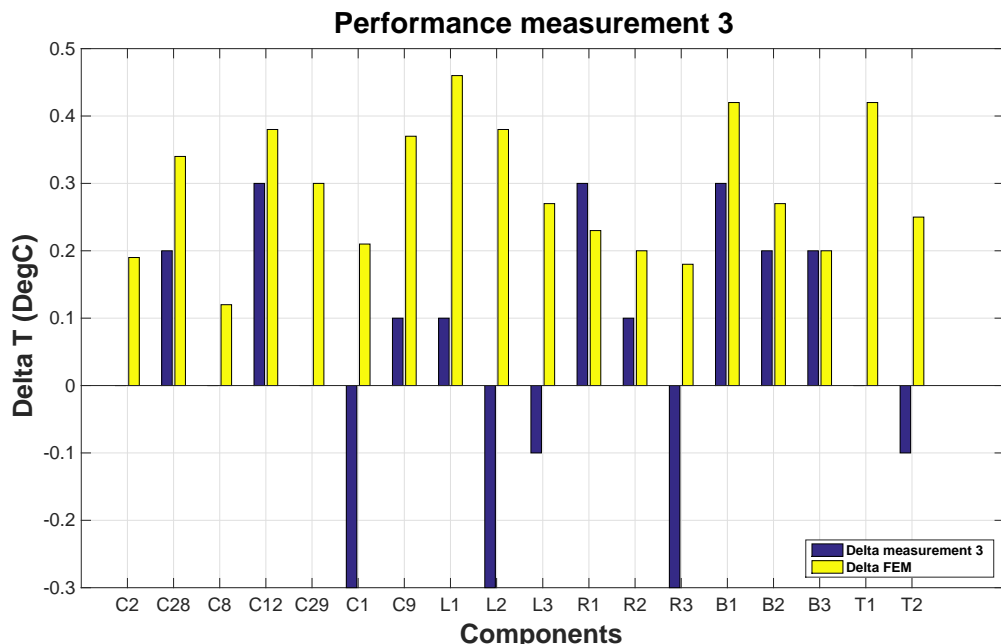


Figure 5.11: The temperature difference for each measurement point between the baseline design and the optimized design from the third measurement. The measured difference and the difference from the FEM model are shown. All results are for a flow of approximately  $0.1 \text{ lmin}^{-1}$

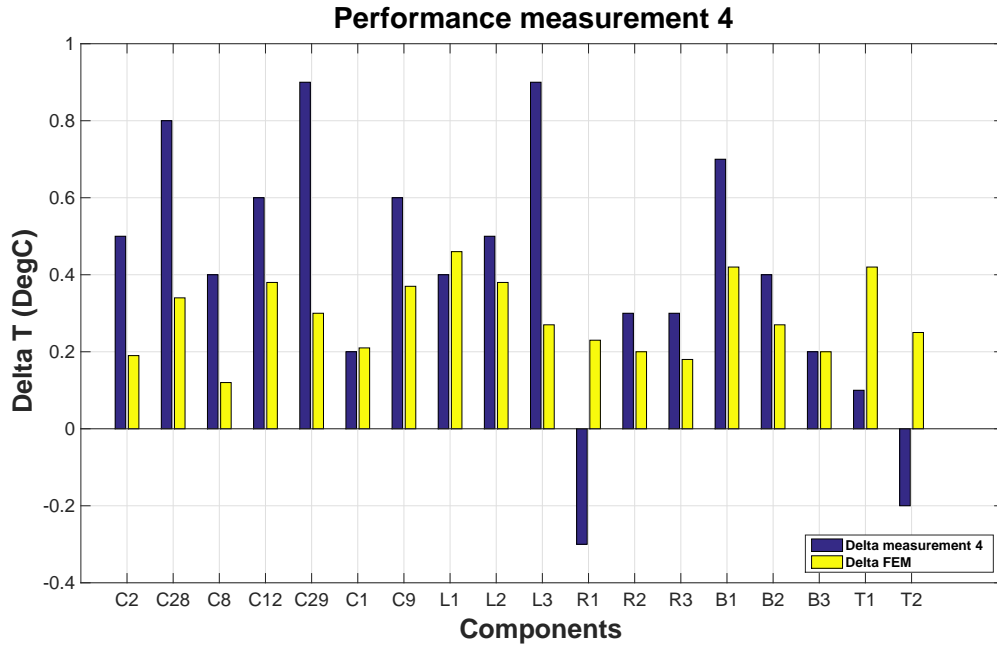


Figure 5.12: The temperature difference for each measurement point between the baseline design and the optimized design from the fourth measurement. The measured difference and the difference from the FEM model are shown. All results are for a flow of approximately  $0.11\text{min}^{-1}$

An attempt to do the optimization with the Navier-Stokes equation is made, but without success. The solver had a lot of trouble finding converged solutions. After a few iterations the solver got stuck and failed to find a better solution, while the solution was far from converged. One of the possible reasons can be that the material density is also in the extra term added for the Navier-Stokes equations. The material density is now in both the heat transfer and the fluid dynamics. This can be an issue for the solver. Another potential cause can be the Reynolds number that comes into play for the Navier-Stokes equations. For high Reynolds numbers Comsol is not able to solve the flow equations. Although this error occurred sometimes it can not be the cause of the solver getting stuck, because Comsol gives an error when the high Reynolds occurs. And when the solver is stuck it does not give an error.

Because no useful results are found with the Navier-Stokes equations but we still want to have an indication of the influence of the Stokes flow assumption, a different comparison is proposed. The flow result from the optimization is compared with a two-dimensional flow model and with a three-dimensional flow model. This means that the result is first converted to a new design where the solid areas are not modeled with the porous media flow but converted to void areas. Next a two-dimensional and a three-dimensional FEM model are made based on the new design. This also gives a good indication between the difference of two-dimensional and three-dimensional flow. For the two-dimensional model the fluid dynamics are modeled with the Stokes flow assumption and without. In Figure 5.13 four velocity field plots are shown. Figure 5.13a shows the velocity field of the topology optimization with the porous media formulation. Figure 5.13b and 5.13c show respectively the two-dimensional model with Stokes flow and with Navier-Stokes flow. And finally Figure 5.13d shows the velocity field of the three-dimensional model with Navier-Stokes flow.

The topology optimization flow and the two-dimensional Stokes flow are on the physics level identical, so it is expected to find the same result. The only difference is that the porous media formulation is removed. The obtained velocity field confirms that the porous media formulation yields the same result as a fully discrete model; the results are almost identical. We then see that for the two-dimensional Navier-Stokes thinner velocity lines are shown and a less evenly distributed flow. This is also what we expect since the inertia forces give momentum to the flow; which causes the thinner velocity lines. But we see that the two-dimensional Navier-Stokes shows not that much resemblance with the three-dimensional Navier-Stokes. This has every-

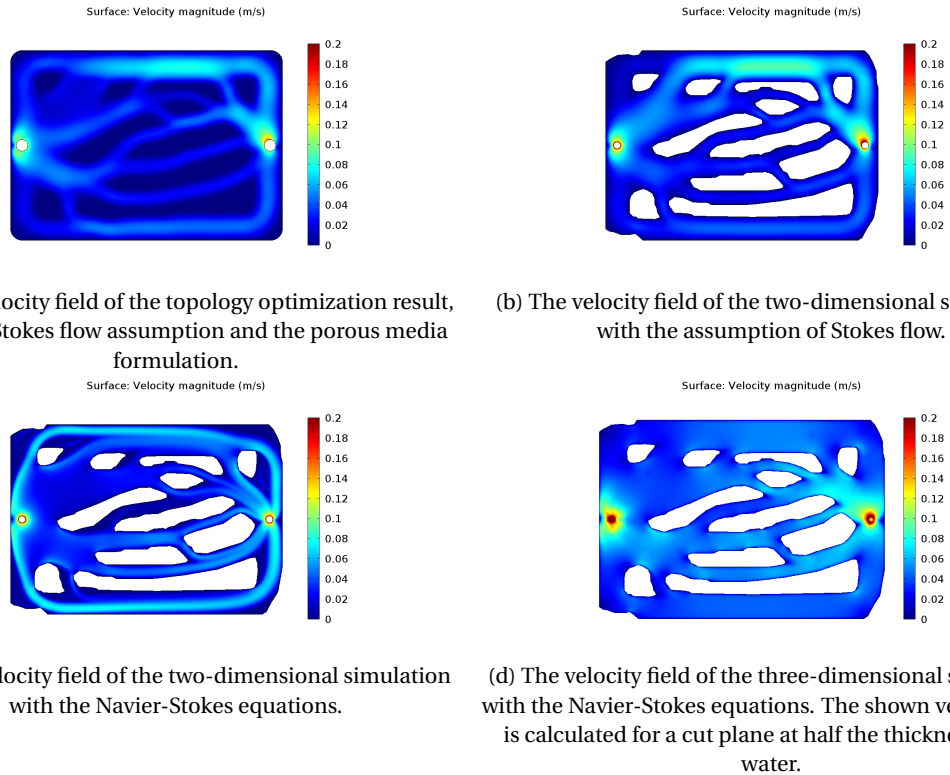


Figure 5.13: The velocity fields of different flow models.

thing to do with the modeling of the thickness in the two-dimensional model. For two-dimensional flow an infinite thickness is assumed. But the three-dimensional model has a thickness of 1 mm. The 1 mm thickness is for the total domain the smallest feature size, i.e. no channels with a thickness smaller than 1 mm are present. This has a large impact on the flow profile, the no slip boundary condition state that the velocity is equal to zero at the boundary. A parabolic velocity profile between two boundaries describes the velocity of the fluid. What this means is that in the two-dimensional case the parabolic velocity profile is described by the width of the channels, which is clearly seen in plots. But for the two-dimensional model the parabolic velocity profile is defined by the plate thickness. Which results in a more evenly distributed velocity profile in plane. Because of this assumption, the more detailed flow equations show less accurate results for the two-dimensional model.

## 5.6. CONCLUSION

*Can we apply a multiphysics topology optimization, describing heat transfer and fluid dynamics, for an actual design load case using a commercially available package?*

This chapter describes the implementation of the topology optimization for the lean E-box concept. Different constraint values are used during the optimization and a set of constraints yielding the best result is presented. The optimization yielded useful and converged results, therefore a concluding answer is given to the research question.

*What is the effect of a low Reynolds number assumption on the topology optimization result and on the flow profile?*

For the fluid dynamics it is assumed that the inertial forces are much smaller than the viscous forces, which allows for a simpler flow equation. The effect of this assumption is studied by comparing the velocity field of four different modeling approaches of the optimized design, where it is assumed that the three-dimensional model governed by the Navier-Stokes equations describes the actual field. Because the two-dimensional fields show both not that much resemblance with the actual field no conclusion can be made on whether the simplified flow equations show less good results. The effect on the flow profile can however be seen, the Navier-Stokes governed model shows thinner lines with higher velocities, also distribution of the water is dif-

ferent.

*What is the influence of varying the inlet and outlet positions of the water flow on the result found for the topology optimization, and the performance of it?*

The performance increase by the different inlet and outlet positions is in the same order of magnitude as the increase by the optimization. This is shown by comparing different combinations of inlet and outlet positions. A design is presented with the overall optimal design, together with a design that shows the highest performance increase with respect to the baseline design. The different designs show that the optimizer yield different results when the inlet and outlet positions is changed.

*Is the predicted performance increase by the topology optimization also seen in an experimental measurement setup?*

An experimental measurement setup is presented, which is used to measure the predicted performance increase. Unfortunately the measurements showed no consistent results. The desired performance increase is in the same order of magnitude as the measurement error. The performance increase could therefore not be verified with the measurement setup.

*What is the added value of the topology optimization for the cooling channels of the lean E-box, and does it weight up to the time investment required for the optimization?*

If we assume that the presented performance increase, although it could not be measured, is in reality also seen. It is still a marginal increase. Combined with the already good thermal behavior of the baseline design, this leads to the conclusion that the added value of the topology optimization for the lean E-box cooling layout is negligible.



# 6

## CONCLUSION

In this thesis a new solution to cool electronic circuit boards in a vacuum environment is presented. The thermal behavior is predicted by a Finite Element analysis and verified by a measurement setup, from which we concluded that the thermal specifications are all satisfied.

An optimized design of the cool plate is also presented, which is acquired by a topology optimization of the cooling channels. It is shown that a commercial Finite Element package can be used to optimize a design using heat transfer and fluid dynamics. The performance increase by the optimization was for this load case however too small to be measured by an experimental setup.

By showing that it is possible to do a complex topology optimization with a commercial package for an industrial load case, the gap of public companies adding topology optimization to their standard design toolkit is shortened.

### 6.1. RECOMMENDATIONS

Although the lean E-box concept showed promising results, there are still some uncertainties. Especially with regards to life time issues. I would recommend first of all repeating the temperature measurements but in a vacuum environment and doing a functionality test with the potted SSB, to check if the SSB still functions well. Then I would recommend to start doing life time measurements. If we assume that these tests show no negative results, is the lean E-box in my opinion the preferred design. As mentioned there are some disadvantages of the design, but I think that the advantages are more significant than the disadvantages.

From an optimization point of view, I would recommend doing a new research project that aims to implement the full Navier-Stokes equations combined with heat transfer for either a three-dimensional design domain or a two-dimensional domain modeled with a constant thickness. The infinite thickness assumption in the two-dimensional model caused the velocity field to be significantly different than the assumed actual field from the three-dimensional model.

A second interesting research project is to implement the inlet and outlet positions as a design variable. We concluded that the positions have a large impact on the performance, therefore it would be interesting to see an optimization with them added as design variables.

For the lean E-box the topology optimization happened to add no significant value. The main reason for this is that the baseline design already shows results that are well within spec. Also the allowed flow specifications are not critical. For design cases where the baseline design shows either results that are not within spec or are critically close to the spec, the topology optimization will add much more value. I would recommend doing a similar project as this research but for a much more critical design case. This will showcase the power of topology optimization for a practical design much better.

The final recommendation is to start using the developed optimization model to find initial design for various industrial design cases. Since the optimization problem is already set up and the model is working, the time required to setup the optimization is relatively small.

# BIBLIOGRAPHY

## REFERENCES

- [1] ASML Company History. <https://www.asml.com/company/history/en/s277?rid=51985>. Accessed: 2015-08-25.
- [2] COMSOL Multiphysics reference manual V5.1.
- [3] A. Gersborg-Hansen, M. P. Bendsoe, O. Sigmund. 2006. Topology optimization of heat conduction problems using the finite volume method. *Struct. Multidisc Optim.*
- [4] A. Gersborg-Hansen, O. Sigmund, R. B. Haber. 2005. Topology optimization of channel flow problems. *Struct. Multidisc Optim.*
- [5] Albin K. J. Hasselstrom, U. Eskil Nilsson. 2012. *Thermal contact conductance in bolted joints*. M.Phil. thesis, Chalmers University of Technology.
- [6] B. S. Lazarov, O. Sigmund. 2011. Filters in topology optimization based on Helmholtz-type differential equations. *International Journal For Numerical Methods in Engineering*.
- [7] Bendsoe, M. P., & Kikuchi, N. 1988. Generating optimal topologies in structural design using a homogenization method. *Computer methods in applied mechanics and engineering*.
- [8] Bendsoe, M.P. 1989. Optimal shape design as a material distribution problem. *Structural Optimization*.
- [9] Box, Sjef. *GID An engineering aestimation for the thermal contact conductance*. Confidential ASML document.
- [10] ChunGang Zhuang, ZhenHue Xiong, Han Ding. 2007. A level set method for topology optimization of heat conduction problem under multiple load cases. *Comput. Methods Appl. Mech. Engrg.*
- [11] C.V. Madhusudana, G.P. Peterson, L.S. Fletcher. 1990. The Effect of Nonuniform Interfacial Pressures on the Heat Transfer in Bolted and Riveted Joints. *Journal of energy resources technology*.
- [12] Dede, Ercan M. 2009. Multiphysics Topology Optimization of Heat Transfer and Fluid Flow Systems. In: *Excerpt form the Proceeding of the COMSOL Conference 2009 Boston*.
- [13] Evgrafov, A. 2005. Topology optimization of slightly compressible fluids. *Journal of applied mathematics and mechanics*.
- [14] Fernlund, I. 1961. *A method to calculate the pressure between bolted or riveted plates*. Chalmers University of Technology.
- [15] G. Allaire, F. Jouve, A. Toader. 2004. Structural optimization using sensitivity analysis and a level-set method. *Journal of Computational Physics*.
- [16] James K. Guest, Jean H. Prevost. 2006. Topology optimization of creeping fluidflows using a Darcy-Stokes finite element. *International journal for numerical methods in engineering*.
- [17] Kentaro Yaji, Takayuki Yamada, Seji Kubo Kazuhiro Izui Shinji Nishiwaki. 2014. A topology optimization method for a coupled thermal-fluid problem using level set boundary expressions. *International Journal of Heat and Mass Transfer*.
- [18] Koga, Adriano A. 2013. Development of heat sink device by using topology optimization. *International Journal of Heat and Mass Transfer*.
- [19] Lohan, Danny J, Dede, Ercan M, & Allison, James T. 2016. Topology Optimization Formulations for Circuit Board Heat Spreader Design. In: *2016 AIAA Aviation and Aeronautics Forum and Exposition*.

- [20] M. M. Yovanovich, J. R. Culham, P. Teertstra. 1997. Calculating interface resistance. *Article3*.
- [21] M. P. Bendsoe, O. Sigmund. 2000. *Topology Optimization: Theory, Methods and Applications*. Springer.
- [22] Madhusudana, C. V. 1996. *Thermal contact conductance*. Springer International Publishing.
- [23] Marcia B. H. Mantelli, Fernando H. Milanez, Eliete N. Pereira. 2010. Statical model for pressure distribution of bolted joints. *Journal of thermophysics and heat transfer*.
- [24] Mikic, B.B. 1974. Thermal Contact Conductance; theoretical considerations. *International Journal of Heat and Mass Transfer*.
- [25] Mills, A.F. 2014. *Basic heat and mass transfer*. Pearson.
- [26] Niels Aage, Thomas H. Poulsen, Allen Gersborg-Hansen Ole Sigmund. 2008. Topology optimization of large scale Stokes flow problems. *Struct. Multidisc Optim.*
- [27] O.M. Querin, V. Young. 2000. Computational efficiency and validation of bi-directional evolutionary structural optimization. *Computational methods for applied mechanical engineering*.
- [28] S. Osher, J.A. Sethian. 1988. Front propagating with curvature dependent speed: algorithms based on Hamilton Jacobi formualtions. *Journal of Computational Physics*.
- [29] Sayed A. Nassar, Antoine Abboud. 2009. An Improved Stiffness Model for Bolted Joints. *Journal of Mechanical design*.
- [30] Scholten, T. C. 2016. D000509738-00-3DRC-001. Internal ASML Document.
- [31] Sigmund, O. 2007. Morphology-based black and white filter for topology optimization. *Struct. Multidisc Optim.*
- [32] Sigmund, Ole. 2011. On the usefulness of non-gradient approaches in topology optimization. *Struct. Multidisc Optim.*
- [33] Svanberg, Krister. 1987. The method of moving asymptotes - A new method for structural optimization. *International journal for numerical methods in engineering*.
- [34] T. Borrrell, J. Petersson. 2003. Topology optimization of fluids in Stokes flow. *International Journal For Numerical Methods in Fluids*.
- [35] T. Gao, W. H. Zhang, J. H. Zhu Y. J. Xu D. H. Bassir. 2008. Topology optimization of heat conduction problems involving design-dependant heat load effect. *Finite Elements in Analysis and Design*.
- [36] V. W. Antonetti, T. D. Whittle, R. E. Simons. 1993. An approximate thermal Contact conductance correlation. *Journal of electronic packaging*.
- [37] Xian-Bao Duan, Yi-Chen Ma, Rui Zhang. 2008. Shape-topology optimization for Navier-Stokes problem using variational level set method. *Applied Mathematics and Computation*.
- [38] Xiaoping Qian, Ercan M. Dede. 2016. Topology Optimization of a coupled Thermal-Fluid System under a tangential Thermal Gradient Constraint. *Structural and Multidisciplinary Optimization*.
- [39] X.Y. Yang, Y.M. Xia, G. P. Steven. 1999a. Topology optimziation for frequency using an evolutionary method. *Journal for structural engineering*.
- [40] X.Y. Yang, Y.M. Xia, G.P. Steven. 1999b. Bidirectional evolutionary method for stiffness optimization. *AIAAJ*.
- [41] Y.M. Xie, G.P. Steven. 1997. *Evolutionary Strucutal Optimization*. Springer.
- [42] Yoon, Gil Ho. 2010. Topological design of heat dissipating structure with forced convective heat transfer. *Journal of mechanical science and technology*.
- [43] Yuxin Wang, H.G. Beom, Haipeng Jia Song Lin Bo Liu. 2011. Evolutionary level set method for structural topology optimization. *Computers and Structures*.

# A

## COMPONENTS

In Table A.1 the specifications for each component on the SSB are shown. The first column states the component name. The second column how many of the corresponding component are present on the SSB. The third column states the power dissipation for a single component, while the fourth column shows the total power dissipation of the specific component. Column five to seven show the junction resistances and the final column shows the maximum allowed temperature.

## A

Table A.1: Component information of the SSB.

| <b>Component</b> | <b>Number of components</b> | <b>Per Unit</b> | <b>Subtotal</b> | $R_{ja}$<br>[°CW <sup>-1</sup> ] | $R_{jc}$<br>[°CW <sup>-1</sup> ] | $R_{jb}$<br>[°CW <sup>-1</sup> ] | $T_{j\_max}$ |
|------------------|-----------------------------|-----------------|-----------------|----------------------------------|----------------------------------|----------------------------------|--------------|
|                  |                             | $P_{max}[W]$    | $P_{max}[W]$    |                                  |                                  |                                  |              |
| C1               | 30                          | 0.193           | 5.801           | 70                               |                                  | 21                               | 110          |
| C2               | 1                           | 2.600           | 2.600           | 12.3                             | 0.13                             | 3.4                              | 55           |
| C3               | 1                           | 0.87            | 0.87            |                                  |                                  | 40                               | 110          |
| C4               | 1                           | 0.773           | 0.773           |                                  |                                  | 40                               | 110          |
| C5               | 1                           | 0.743           | 0.743           |                                  | 11                               | 11                               | 110          |
| C6               | 1                           | 0.685           | 0.685           |                                  |                                  | 40                               | 110          |
| C7               | 1                           | 0.527           | 0.527           | 45                               | 10                               | 0                                | 110          |
| C8               | 1                           | 0.525           | 0.525           |                                  |                                  |                                  | 60           |
| C9               | 1                           | 0.417           | 0.417           |                                  | 11                               | 11                               | 110          |
| C10              | 1                           | 0.365           | 0.365           |                                  | 11                               | 11                               | 110          |
| C11              | 1                           | 0.292           | 0.292           |                                  | 11                               | 11                               | 110          |
| C12              | 1                           | 0.256           | 0.256           |                                  |                                  |                                  | 70           |
| C13              | 12                          | 0.019           | 0.225           | 130                              | 43                               | 83                               | 110          |
| C14              | 30                          | 0.007           | 0.220           | 190                              | 44                               |                                  | 110          |
| C15              | 1                           | 0.206           | 0.206           |                                  |                                  |                                  | 105          |
| C16              | 6                           | 0.032           | 0.193           |                                  |                                  | 50                               | 60           |
| C17              | 1                           | 0.149           | 0.149           |                                  |                                  | 28                               | 75           |
| C18              | 30                          | 0.004           | 0.131           | 200                              | 44                               | 110                              | 75           |
| C19              | 1                           | 0.128           | 0.128           |                                  | 11                               | 11                               | 110          |
| C20              | 30                          | 0.004           | 0.120           | 190                              | 44                               |                                  | 110          |
| C21              | 12                          | 0.013           | 0.116           |                                  |                                  |                                  | 70           |
| C22              | 1                           | 0.116           | 0.116           |                                  |                                  |                                  | 105          |
| C23              | 1                           | 0.113           | 0.113           |                                  |                                  |                                  | 60           |
| C24              | 1                           | 0.109           | 0.109           |                                  |                                  |                                  | 105          |
| C25              | 8                           | 0.013           | 0.107           |                                  |                                  | 50                               | 75           |
| C26              | 10                          | 0.010           | 0.100           | 83                               |                                  |                                  | 75           |
| C27              | 1                           | 0.086           | 0.086           |                                  |                                  | 25                               | 110          |
| C28              | 1                           | 0.086           | 0.086           |                                  |                                  |                                  | 55           |
| C29              | 1                           | 0.064           | 0.064           |                                  |                                  |                                  | 60           |
| C30              | 1                           | 0.059           | 0.059           |                                  |                                  |                                  | 105          |
| C31              | 1                           | 0.050           | 0.050           |                                  | 80                               |                                  | 75           |
| C32              | 1                           | 0.049           | 0.049           |                                  | 11                               | 11                               | 110          |
| C33              | 1                           | 0.021           | 0.021           |                                  |                                  |                                  | 60           |
| C34              | 30                          | 0.000           | 0.013           |                                  |                                  | 83                               | 110          |
| C35              | 12                          | 0.000           | 0.005           | 90                               | 0                                | 60                               | 110          |
| C36              | 1                           | 0.005           | 0.005           |                                  | 11                               | 11                               | 110          |
| C37              | 1                           | 0.004           | 0.004           |                                  |                                  |                                  | 105          |
| C38              | 1                           | 0.004           | 0.004           |                                  | 11                               | 11                               | 110          |
| C39              | 1                           | 0.002           | 0.002           |                                  | 11                               | 11                               | 110          |
| C40              | 1                           | 0.002           | 0.002           |                                  | 11                               | 11                               | 110          |
| C41              | 1                           | 0.001           | 0.001           |                                  | 11                               | 11                               | 110          |
| C42              | 1                           | 0.000           | 0.000           |                                  | 11                               | 11                               | 110          |

# B

## JUNCTION RESISTANCE

A junction resistance is the thermal resistance that describes the behavior of the temperature from the junction to the outside of an electrical component. Junction resistances are used to simplify the modeling of the components of the SSB. Instead of creating a detailed model of the component, the component is modeled as a rectangular block. On the surfaces of the block a thermal resistance is modeled.

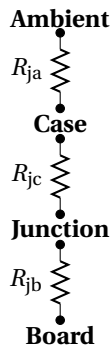


Figure B.1: Schematic illustration of the junction resistances of the components on the PCA. The two thermal paths are from the junction to the board and from the junction to the ambient.

The thermal behavior of each component is described by three junction resistances; ambient resistance, case resistance and the board resistance. In Figure B.1 the three different resistances are shown schematically. From the junction of the components there are two thermal paths. One from the junction to the board, this is most of the times via the connection pins. And from the junction through the case and to the ambient. This is through the housing of the component.

The values of the junction resistances are most of the times supplied by the manufacturer of the component. For the SSB the junction resistances of most components are available.

### B.1. IMPLEMENTATION IN THE FEM MODEL

The junction resistances are given in  $\text{KW}^{-1}$ . Unfortunately there is no function in Comsol to directly add a thermal resistance. There is however a function called 'thin layer'. With this function one can add properties to a surface that resembles a thin layer of material. An option within the thin layer function is a resistive layer with input variable  $R_s$  in  $\text{Km}^2\text{W}^{-1}$ . So to get the junction resistances in the correct units we must multiply with the area of the component. This should yield the correct values for the junction resistances. This can be tested with a simple hand calculation of a steady state thermal conduction problem.

Let us take a simple two part beam as shown in Figure B.2. At the intersection of the beam there is an additional thermal resistance  $R_{th}$ . We find the temperature  $T_1$  at the heat load is described by[25]:

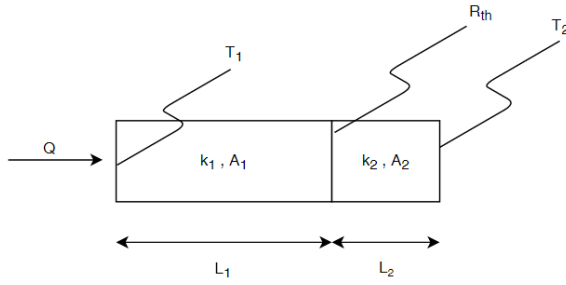
**B**

Figure B.2: Arbitrary illustration of a simple thermal resistance problem. This problem is used to verify the implementation method in COMSOL. The problem consists of two materials with properties  $\{k, A, L\}$ . An extra thermal resistance is present at the interface of the two materials. The heat load  $Q$  and the temperature  $T_2$  are known and  $T_1$  is the unknown variable.

$$T_1 = Q \left( \frac{L_1}{k_1 A_1} + \frac{L_2}{k_2 A_2} + R_{th} \right) + T_2 \quad (\text{B.1})$$

Where  $Q$  is the heat load,  $k$  is the thermal conductivity,  $L$  is the length,  $A$  is the cross sectional area,  $T$  is the temperature and  $R_{th}$  is the thermal resistance.

For some arbitrary values, shown in Table B.1, a temperature of 540 °C is found for  $T_1$ . If we now build a similar model in Comsol and use the thin layer function to add the thermal resistance we find the same result, as shown in Figure B.3. This verifies that the thin layer function yields the correct result and that we can add all the thermal resistances with the thin layer function.

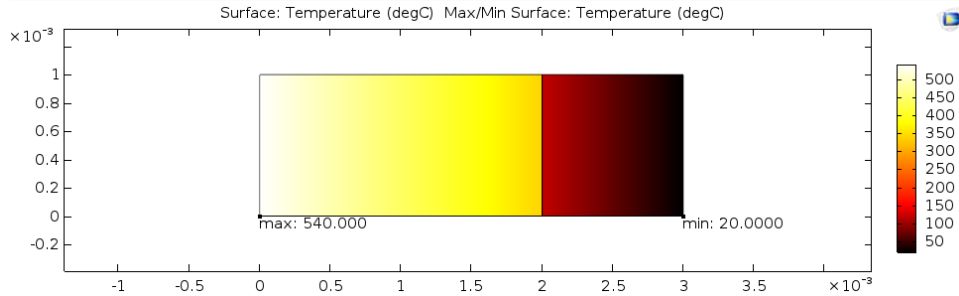


Figure B.3: The result of the implementation of the problem shown in Figure B.2 in Comsol. The image shows the temperature field of the two materials. The minimum and maximum temperature are also shown, the minimum temperature is the boundary temperature  $T_2$  from Figure B.2.

Table B.1: Arbitrary values for simple thermal resistance calculation.

| Variable | Value                            |
|----------|----------------------------------|
| $Q$      | 10 W                             |
| $k_1$    | $100 \text{ W m}^{-1} \text{ K}$ |
| $k_2$    | $100 \text{ W m}^{-1} \text{ K}$ |
| $A_1$    | $1 \text{ mm}^2$                 |
| $A_2$    | $1 \text{ mm}^2$                 |
| $L_1$    | 2 mm                             |
| $L_2$    | 1 mm                             |
| $T_2$    | 20 °C                            |
| $R_{th}$ | $22 \text{ KW}^{-1}$             |

# C

## DESIGN DECISIONS OF THE LEAN E-BOX

This appendix functions as an extension of section 2.5. The design aspects of the concept design will be discussed in more detail. This will be done by covering three main design aspects:

- The design of the housing
- The design of the cooling
- The fabrication and manufacturing of the concept

In each dedicated section the important decision making points will be discussed. Not all design related decisions are mentioned because the focus of this research is on the feasibility of the design. The decisions mentioned in this chapter are the most important ones. They are however kept out of the main report to give a more overall reading experience.

### C.0.1. THE DESIGN OF THE HOUSING

A main criterion for the housing is that it must be completely closed. The potting can not be in contact with the vacuum. This is because the potting is considered 'dirty', i.e. it has bad outgassing properties. Outgassing is an important property for materials in the vacuum environment. Outgassing is simply said the release of gas that is trapped inside the material. The released gas can decrease the performance of the machine.

So the lean E-box must be completely closed, but if the housing is literally completely closed the SSB can not be connected to a power supply. The SSB has on one side two big connectors. The connectors have multiple input/output entries. For the SSB to work, the connector has to be plugged into its counterpart. This means that the design must be such that the SSB connectors can be attached to the counterpart on the wafer-stage.

We solved this by keeping the connectors outside the housing. Behind the connectors a cover plate is attached to the PCB material of the SSB. The cover plate is used to close the housing. Behind the connectors, a small area of PCB material is present that can be used as a connection area for the cover plate. This area is however so small that the risk of damaging a component is likely. Therefore it is decided to extend the PCB material of the SSB by 7 mm. A small redesign of the SSB must already be done because the connectors will be used directly in the vacuum. The extension of the PCB material is a small addition during this redesign. In Figure C.1 a picture of the SSB connectors is shown, in the picture a red line is drawn; the red line indicates the location of the cover plate in the non extended case. This gives an indication of how close the cover plate is to the components.

It is however not sure that the connection of the cover plate in the non extended design will actually damage the components. Additional research must be done to check this. This is however out of the scope of this project. The extended design removes the uncertainty of damaging the components. That is why it is implemented in the final design. Another advantage is that the cover plate will be a flat plate instead of a 'corner' shaped plate.

C

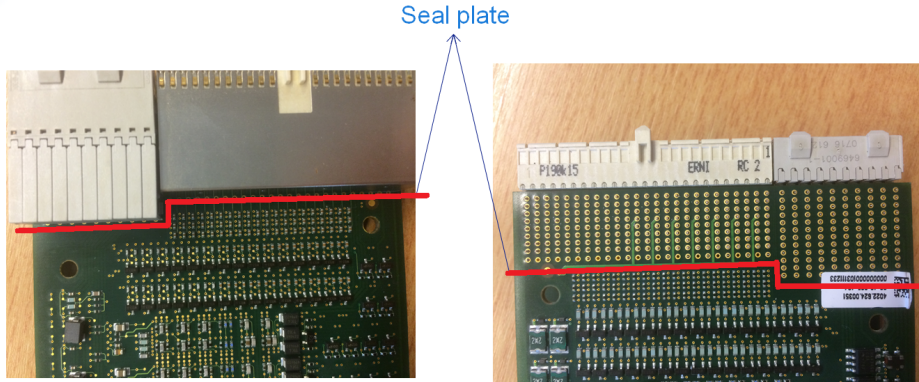


Figure C.1: Picture of both the top and bottom side of the SSB with a red line that represents the cover plate. From the picture it can be seen that the cover plate will be very close to the components.

### C.0.2. THE DESIGN OF THE COOLING

On first hand the most logical decision seems to be to implement the water cooling in the housing of the lean E-box. This was also the first design iteration. This however brings some complications with regards to serviceability. Because the complete lean E-box becomes a spare part, the complete lean E-box must be replaced if a defect occurs. This means that, if the water cooling is implemented in the housing, the cooling channels must be drained during service. Also the risk of leaking water during service arises. For this reason it was decided to make a separate cool plate. And connect the lean E-box to the cool plate with a bolt connection.

It is decided to use one cool plate to cool the lean E-box. The cool plate will be located on the side where the most heat dissipating components are located. In an early iteration two cool plates are considered. One cool plate gives however sufficient cooling. The second cool plate will however result in a lower average outside temperature. If in the detail design phase issues arise with a high outside temperature the consideration of a second cool plate can be done.

This leads to a design with only a single cool plate that is connected via a bolted connection to the lean E-box. There is however an addition phenomena that arises because of the external cool plate. That is the concept of a thermal contact resistance. This is a thermal resistance that arises for heat transfer through two surfaces in contact. In Figure C.2 the concept of thermal contact resistance is depicted. The thermal contact resistance is, for this research, determined by the model of Yovanovich [20] :

$$h_c = 35.3 k_s R_a^{-0.6} \left( \frac{P}{H_c} \right)^{0.95} \quad (\text{C.1})$$

where  $h_c$  thermal contact heat transfer coefficient [ $\text{Wm}^{-2} \text{K}^{-1}$ ]

$k_s$  harmonic mean thermal conductivity of the interface [ $\text{Wm}^{-1} \text{K}^{-1}$ ]

$R_a$  effective surface roughness [m]

$P$  apparent contact pressure [Pa]

$H_c$  surface micro hardness of the softer contacting solid [Pa]

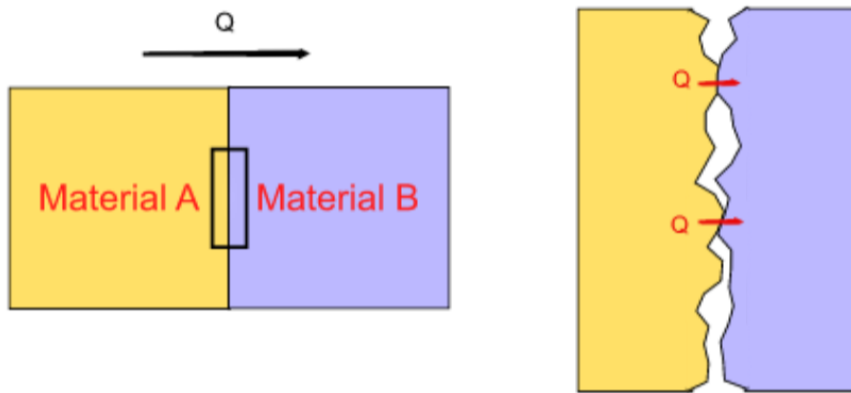
Where  $k_s$  and  $R_a$  are defined as:

$$k_s = \frac{2k_A k_B}{k_A + k_B} \quad (\text{C.2})$$

$$R_a = \sqrt{R_{aA}^2 + R_{aB}^2} \quad (\text{C.3})$$

Where the subscripts 'A' and 'B' mean that the properties are respectively from material A and material B. With  $k_{\{A,B\}}$  being the thermal conductivity and  $R_{a\{A,B\}}$  the surface roughness.

From equation C.1 we can conclude that the thermal contact resistance is dependent on the contact pressure, which is directly related to the bolt connection. According to the models described by Fernlund and Nassar [14] [29] is the pressure field around a bolt highly depended on the radial distance from the bolt. The pressure field drops to negligible values in the order of millimeters away from the bolt. See Appendix D for a derivation of the thermal contact resistance and the pressure field around the bolts for the lean E-box.



C

Figure C.2: Schematic illustration of the working principles of the contact resistance. The left image is a macroscopic view of two arbitrary materials, the two materials are connected at the interface in the middle. An arbitrary heat load goes through the material from left to right. On the right side of the image a microscopic view of the two materials is shown. It is shown that the two materials are not completely flat, because of this the heat load can only transfer through a small area.

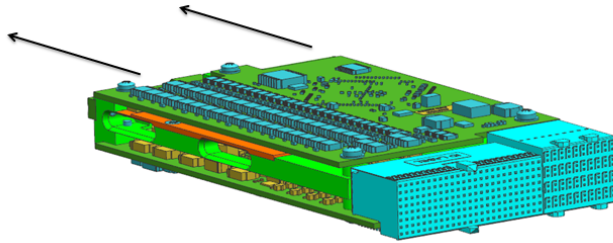
Since it is not possible to use bolts in the middle of the cool plate, only on the outside. It is according to the theory supplied by Fernlund not possible to achieve thermal conductivity in the middle of the cool plate, if we assume that the negligible pressure results in zero conductivity. One way to solve this issue is with the use of a thermal gap filler pad. This is a pad that is specially designed for filling the gaps, illustrated in Figure C.2, between two thermal surfaces. The results from the FEM model will have to determine whether the use of a thermal gap filler pad is necessary.

The design of the cool plate will consist of two parts, one part where the cooling channels are milled out off and the other part is just a flat plate. The plate will be attached on top of the cooling channels via a welded connection. The layout of the cooling channels is kept very basic. This layout will be optimized with the topology optimization. Therefore it is decided to not spent much time on the design of the cooling channels. The material used for the cool plate is stainless steel. The decision to use stainless steel is made because it gives good properties against corrosion and it is easy to weld. The downfall is a moderate thermal conductivity.

### C.0.3. THE FABRICATION AND ASSEMBLY OF THE CONCEPT

The final aspect of the design process that will be discussed is the method of fabrication and the assembly of the design. The dimensions, as mentioned before, of the SSB are 150 mm by 80 mm by 20 mm. This means that the inside volume of the housing atleast needs to be the same. We decided in section C.0.1 to attach a cover plate to the SSB and keep the connectors outside the lean E-box. This means that the SSB needs to be inserted in the housing in the direction of the long side, see Figure C.3.

For manufacturing this means that a hole of 80 mm by 20 mm needs to be milled with a depth of 150 mm. This is however not possible with conventional milling machines. Especially not for a relative thin wall thickness. There is a general milling rule of thumb that describes the minimum wall thickness for a certain depth. For aluminum this is 1:10, i.e. for every 10 mm of depth the wall thickness must be 1 mm. This means that the wall thickness must be atleast 15 mm. This is approximately the same thickness as the E-box, so this is not an option.



C

Figure C.3: CAD model of the SSB with two indications arrows. The arrows indicate the direction in which the SSB is inserted inside the lean E-box.

To circumvent the milling problem the housing is split up in two pieces. In Figure C.4 the two pieces are illustrated. The milling depth is, as seen in the figure, for this configuration much shorter. This way the wall thicknesses can be kept relatively thin. This however adds an additional assembly step, the two parts need to be attached together. This can be done in many different ways, however for this research only two ways are looked into:

- A weld connection
- A glue connection

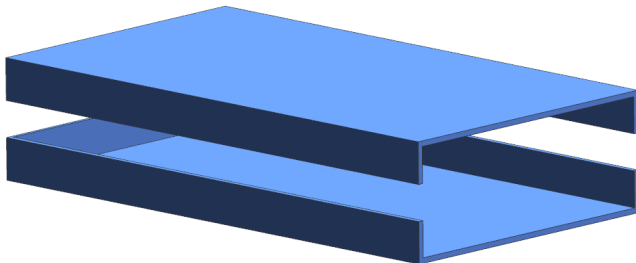


Figure C.4: An illustration of a simplified CAD model of the two piece housing. The figure gives an indication of how the housing is split in two pieces to make the design meet the specification of the milling machine.

The use of a glue connection is, compared to welding, cheaper and easier. A downfall is however the higher outgassing properties. The strength of a weld connection is also stronger than that of a glue connection, this however is not relevant for this application. The housing will be filled with potting, this also gives a strong connection between the two housing parts. To make a decision on whether to use welding or glue, a comparison between the increase in outgassing and the decrease in price of glue compared to welding is made. In consultation with a Cost Engineer at ASML the conclusion was made that welding is roughly two times as expensive as gluing. To compare the outgassing difference two outgassing overviews are made, one for a glued solution and one for a welded solution. In this overview also the connection between the cover plate and the housing is taken as either welded or glued.

The total outgassing properties for the welded and glued solution are respectively shown in Figure C.6 and C.5. Note that the specs are derived from the outgassing spec of the E-box. This means that the spec is for the three lean E-boxes combined. Only an indication of the outgassing for the SSB lean E-box can be made, no indication can be made for the other two PCA's. Therefore we assumed that the outgassing of the other two lean E-boxes is the same as that for the SSB lean E-box.

From the figures one can see that the outgassing of  $C_{45}H_{100}$  and  $C_{100}H_{200}$  for both the welded and the glued solution is within spec. The outgassing of  $H_2O$  however is for both solutions out of spec. The main reason

for the high H<sub>2</sub>O outgassing is the PCB material. This is the part where the connectors are connected on, everything above the red line in Figure C.1. The glue however has a very small influence on the outgassing and is not the reason for being out of spec. Because the influence is really small and the use of glue is twice as cheap it is decided to go with the glued solution.

A possible solution for high H<sub>2</sub>O outgassing is to use a different PCB material. The PCB material on the SSB is standard PCB material. There are however materials with a lower outgassing. Another solution is to reconsider the outgassing spec. Compared with the total waferstage outgassing budget, the lean E-box only does 0.076 % of the total budget.

C

| Glued concept         |          |  |                    |                 |                    |  |                    |                  |             |                                |  |
|-----------------------|----------|--|--------------------|-----------------|--------------------|--|--------------------|------------------|-------------|--------------------------------|--|
| Material distribution |          | Outgassing (mBar.l/s.cm <sup>2</sup> ) |                    |                 |                    | Outgassing (mBar.l/s.cm <sup>2</sup> ) |                    |                  |             | Outgassing percentage of total |  |
| Material              | Area     | H <sub>2</sub> O                       | CxHx 45-100        | CxHx 100-200    | H <sub>2</sub> O   | CxHx 45-100                            | CxHx 100-200       | H <sub>2</sub> O | CxHx 45-100 | CxHx 100-200                   |  |
| Titanium grade 5      | 378.3058 | 2E-10                                  | 2E-12              | 1.54E-13        | 7.56612E-08        | 7.56612E-10                            | 5.82591E-11        | 1%               | 6%          | 6%                             |  |
| LCP                   | 82.28707 | 7.23E-09                               | 1.74E-11           | 7.84E-12        | 5.94936E-07        | 1.4318E-09                             | 6.45131E-10        | 5%               | 11%         | 65%                            |  |
| Araldite 2030         | 0.74104  | 1.54E-06                               | 7.371E-09          | 6.24E-11        | 1.13913E-06        | 5.46221E-09                            | 4.62409E-11        | 10%              | 41%         | 5%                             |  |
| FR4                   | 36.32608 | 2E-07                                  | 1.5E-10            | 6E-12           | 7.26522E-06        | 5.44891E-09                            | 2.17956E-10        | 61%              | 41%         | 22%                            |  |
| Viton O-ring          | 1.481684 | 5.00E-07                               | 2.00E-10           | 1.50E-11        | 7.40842E-07        | 2.96337E-10                            | 2.22253E-11        | 6%               | 2%          | 2%                             |  |
| Coupling leak         | 2        | 1.00E-06                               | 0.00E+00           | 0.00E+00        | 0.000002           | 0                                      | 0                  | 17%              | 0%          | 0%                             |  |
|                       |          |  | <b>1.18158E-05</b> |                 | <b>1.33959E-08</b> |  | <b>9.89812E-10</b> | 100%             | 100%        | 100%                           |  |
|                       |          |  | Total 3x lean Ebox | 3.54E-05        | 4.02E-08           | 2.97E-09                               |                    |                  |             |                                |  |
|                       |          |  | Spec               | <b>1.10E-05</b> | <b>5.12E-08</b>    | <b>5.12E-09</b>                        |                    |                  |             |                                |  |
|                       |          |  | Delta              | -2.44E-05       | 1.10E-08           | 2.15E-09                               |                    |                  |             |                                |  |
|                       |          |  |                    | 322.25%         | 78.49%             | 58.00%                                 |                    |                  |             |                                |  |
|                       |          |  | Total WS budget    | <b>4.30E-02</b> | <b>1.30E-03</b>    | <b>8.80E-05</b>                        |                    |                  |             |                                |  |
|                       |          |  | Percentage         | 0.0824%         | 0.0031%            | 0.0034%                                |                    |                  |             |                                |  |

Figure C.5: Outgassing overview of the glued concept design

| Welded concept        |          |  |                    |                 |                   |  |                    |                  |             |                                |  |
|-----------------------|----------|--|--------------------|-----------------|-------------------|--|--------------------|------------------|-------------|--------------------------------|--|
| Material distribution |          | Outgassing (mBar.l/s.cm <sup>2</sup> ) |                    |                 |                   | Outgassing (mBar.l/s.cm <sup>2</sup> ) |                    |                  |             | Outgassing percentage of total |  |
| Material              | Area     | H <sub>2</sub> O                       | CxHx 45-100        | CxHx 100-200    | H <sub>2</sub> O  | CxHx 45-100                            | CxHx 100-200       | H <sub>2</sub> O | CxHx 45-100 | CxHx 100-200                   |  |
| Titanium grade 5      | 378.3058 | 2E-10                                  | 2E-12              | 1.54E-13        | 7.56612E-08       | 7.56612E-10                            | 5.82591E-11        | 1%               | 8%          | 6%                             |  |
| LCP                   | 82.28707 | 7.23E-09                               | 1.74E-11           | 7.84E-12        | 5.94936E-07       | 1.4318E-09                             | 6.45131E-10        | 5%               | 16%         | 68%                            |  |
| Araldite 2030         | 0.1632   | 1.54E-06                               | 7.371E-09          | 6.24E-11        | 2.50871E-07       | 1.20295E-09                            | 1.01837E-11        | 2%               | 13%         | 1%                             |  |
| FR4                   | 36.32608 | 2E-07                                  | 1.5E-10            | 6E-12           | 7.26522E-06       | 5.44891E-09                            | 2.17956E-10        | 66%              | 60%         | 23%                            |  |
| Viton O-ring          | 1.481684 | 5.00E-07                               | 2.00E-10           | 1.50E-11        | 7.40842E-07       | 2.96337E-10                            | 2.22253E-11        | 7%               | 3%          | 2%                             |  |
| Coupling leak         | 2        | 1.00E-06                               | 0.00E+00           | 0.00E+00        | 0.000002          | 0                                      | 0                  | 18%              | 0%          | 0%                             |  |
|                       |          |  | <b>1.09275E-05</b> |                 | <b>9.1366E-09</b> |  | <b>9.53755E-10</b> | 100%             | 100%        | 100%                           |  |
|                       |          |  | Total 3x lean Ebox | 3.28E-05        | 2.74E-08          | 2.86E-09                               |                    |                  |             |                                |  |
|                       |          |  | Spec               | <b>1.10E-05</b> | <b>5.12E-08</b>   | <b>5.12E-09</b>                        |                    |                  |             |                                |  |
|                       |          |  | Delta              | -2.18E-05       | 2.38E-08          | 2.26E-09                               |                    |                  |             |                                |  |
|                       |          |  |                    | 298.02%         | 53.53%            | 55.88%                                 |                    |                  |             |                                |  |
|                       |          |  | Total WS budget    | <b>4.30E-02</b> | <b>1.30E-03</b>   | <b>8.80E-05</b>                        |                    |                  |             |                                |  |
|                       |          |  | Percentage         | 0.0762%         | 0.0021%           | 0.0033%                                |                    |                  |             |                                |  |

Figure C.6: Outgassing overview of the welded concept design



# D

## THERMAL CONTACT MODEL

This appendix will discuss the derivation of the thermal contact resistance for both the vacuum case and for the atmospheric case. The first thing to determine is if the deformation of the roughness peaks is elastic or plastic deformation. This will have a large effect on the thermal contact conductance; elastic deformation has a much lower thermal contact conductance than plastic deformation. To check if the deformation is plastic or elastic the following parameter is proposed by Mikic [24]:

$$\gamma = \frac{H_c}{E' \Delta a'} \quad (\text{D.1})$$

With  $H_c$  being the surface micro hardness of the softer contacting solid,  $E'$  the effective modulus of elasticity and  $\Delta a'$  the effective mean of absolute slope of surface profile. For  $\gamma > 3$  the deformation is fully elastic and for  $\gamma < 0.33$  the deformation is fully plastic. ASML listed the values of  $\gamma$  for different material combinations and surface roughness's[9]. For aluminum and stainless steel combination that is used for the lean E-box and the cool plate  $\gamma = 0.11$ , this means we have plastic deformation.

The equation proposed by Yovanovich [20] is used to calculate the plastic contact conductance, this formulation is similar to the one proposed by Mikic [24].

$$h_c = 1.25 k_s \frac{m'}{\sigma'} \left( \frac{P}{H_c} \right)^{0.95} \quad (\text{D.2})$$

Where  $h_c$  is the thermal contact heat transfer coefficient,  $k_s$  is the harmonic mean thermal conductivity of the interface,  $m'$  is the effective mean of absolute slope of surface profile,  $\sigma'$  is the equivalent RMS surface roughness,  $P$  is the apparent contact pressure and  $H_c$  is the micro hardness of the softer contacting solid.

The parameters used in equation D.2 are however not engineering standards and therefore hard to interp for a specific material. We can however make some assumptions to make the equation more practical. If we assume a Gaussian surface distribution we can, according to Antonetti [36], approximate:

$$m' \approx 1.25 \Delta a \quad (\text{D.3})$$

and

$$\sigma' \approx 1.25 R_a \quad (\text{D.4})$$

Where  $\Delta a$  is the effective mean absolute slope defined as:

$$\Delta q = \frac{1}{L} \int_0^L \left| \frac{dz}{dx} \right| dx \quad (\text{D.5})$$

In most cases there is however no value for both  $m'$  and  $\Delta q$  known and therefore we can estimate according

to Antonetti the following relation:

$$\Delta q = 0.171 R_a^{0.402} \quad (\text{D.6})$$

Where  $R_a$  is the surface roughness; which is more commonly known. With the above mentioned relation we can rewrite equation D.2 to:

$$h_c = 35.3 k_s R_a^{-0.6} \left( \frac{P}{H_c} \right)^{0.95} \quad (\text{D.7})$$

Where  $k_s$ ,  $R_a$  and  $E$  are defined as:

$$k_s = \frac{2k_A k_B}{k_A + k_B} \quad (\text{D.8})$$

$$E = \frac{1}{\frac{1-v_A^2}{E_A} + \frac{1-v_B^2}{E_B}} \quad (\text{D.9})$$

$$R_a = \sqrt{R_{aA}^2 + R_{aB}^2} \quad (\text{D.10})$$

The apparent contact pressure  $P$  is assumed to be constant over the whole surface in this equation. However in the case of the lean E-box  $P$  is depended on the bolted connection. We can assume  $P = \frac{F}{A}$ , where  $F$  is the axial force of a single bolt and  $A$  is the contact surface area. This is however not very accurate; the pressure field around a bolts drops to negligible values within a couple of millimeters as described in several papers [14][29][23][11]. Therefore we can not assume that the axial bolt force is uniform over the surface. The model described by Fernlund [14] states a conical stress distribution extending from the bolt head. This model is shown in Figure D.1. The radius of the stress model is given by:

$$x = \frac{d_s}{2} + z \tan \alpha \quad (\text{D.11})$$

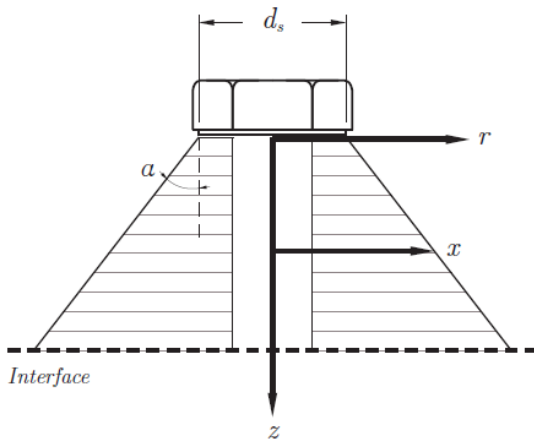


Figure D.1: Illustration of the pressure cone model introduced by Fernlund [14], illustration by Hasselstrom [5]. The model states a cone shaped pressure distribution as function of the lateral distance,  $z$ , from the bolt head.

Where  $d_s$  is the head diameter of the bolt,  $\alpha$  is the angle of the cone and  $z$  is the axial distance. From this model we see that it is better to put the interface further away from the bolt head, since it increases the pressure area. The pressure distribution can be determined with the following relation:

$$P(r, z) = A' r^4 + B' r^3 + C' r^2 + D' r + E \quad (\text{D.12})$$

Table D.1: Parameters used for the pressure field calculation

| Parameter | Value |
|-----------|-------|
| $d_s$     | 7 mm  |
| $z$       | 8 mm  |
| $\alpha$  | 45°   |
| $F$       | 738 N |
| $d$       | 4 mm  |

where

$$A'(z) = \frac{\frac{15}{\pi} \left(\frac{2}{d}\right)^6 F}{-\left(\frac{2x}{d}\right)^6 + 2\left(\frac{2x}{d}\right)^5 + 5\left(\frac{2x}{d}\right)^4 - 20\left(\frac{2x}{d}\right)^3 + 25\left(\frac{2x}{d}\right)^2 - 14\left(\frac{2x}{d}\right) + 3} \quad (\text{D.13})$$

$$B'(z) = -\left(\frac{4}{3}\right)\left(\frac{4x}{d} + 1\right)\left(\frac{d}{2}\right)A' \quad (\text{D.14})$$

$$C'(z) = 2\left(\frac{2x}{d}\right)\left(\frac{2x}{d} + 2\right)\left(\frac{d}{2}\right)^2 A' \quad (\text{D.15})$$

$$D'(z) = -2x^2 d A' \quad (\text{D.16})$$

$$E'(z) = -\left(\frac{1}{3}\right)\left(\frac{2x}{d}\right)^3\left(\frac{2x}{d} - 4\right)\left(\frac{d}{2}\right)^4 A' \quad (\text{D.17})$$

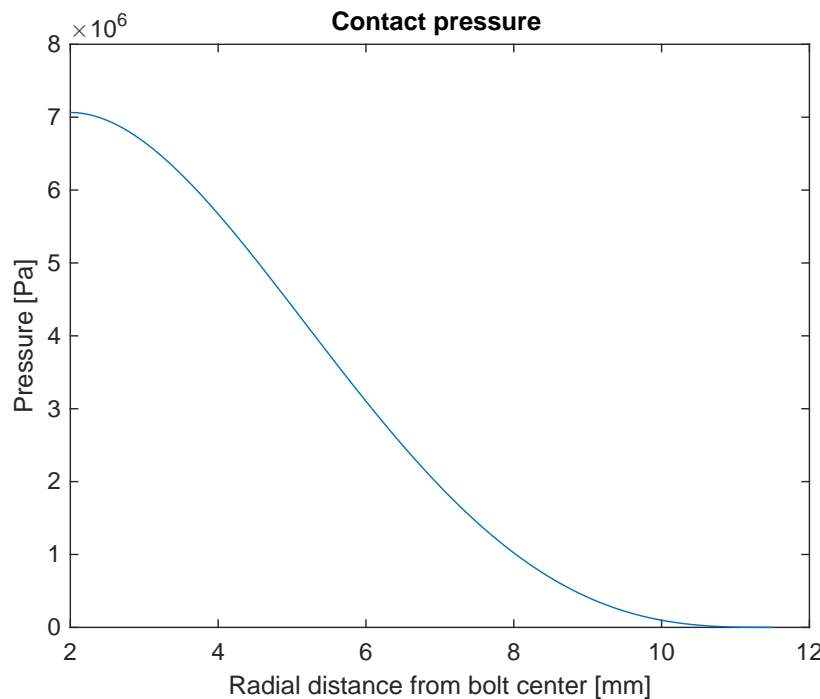


Figure D.2: The pressure as function of the radial distance from the bolt center. The pressure goes to zero at a distance of approximately 20 mm

We can now use the derived pressure field and implement it in equation D.7. To simplify the implementation in the FEM model; a uniform pressure is taken on the calculated area around the bolt. For this the average pressure on the area is taken,  $P_{\text{avg}} = 2.833 \times 10^6 \text{ Pa}$ . If we calculate the thermal contact conductance we find  $h_c = 8.629 \times 10^3 \text{ Wm}^{-2} \text{ K}^{-1}$ . This is only on the area around the bolt. The remaining area is assumed to have  $h_c = 0$ .

There is however an additional thermal conductance; the gas gap conductance. This is the thermal conductance via the gas that is present between the roughness peaks. For the vacuum environment there is off course no gas in the environment, so also no gas between the roughness peaks. The gas gap conductance is therefore zero in vacuum. For the atmospheric load case of the lean E-box there is however a gas gap conductance. The general equation for the gas gap conductance is given by Madhusudana [22]:

$$h_g = \frac{k_g}{\delta + g_1 + g_2} \quad (\text{D.18})$$

Where  $h_g$  is the heat transfer coefficient of the gas gap,  $k_g$  is the thermal conductivity of the gas,  $\delta$  is the mean thickness of the gas gap and  $g_1, g_2$  are the temperature jump distances at side 1 and 2. For certain values of the non-dimensional Knudsen number the general equation can be simplified. For  $Kn < 0.01$   $g_1$  and  $g_2$  can be neglected. And for  $Kn > 10$  the mean thickness  $\delta$  can be neglected.  $Kn$  is given by:

$$Kn = \frac{\lambda}{\delta} \quad (\text{D.19})$$

Where  $\lambda$  is the mean free path of the gas molecules given by:

$$\lambda = \frac{kT}{\pi p d^2 \sqrt{2}} \quad (\text{D.20})$$

with  $k$  being the Boltzmann constant,  $T$  the temperature,  $p$  the gas pressure and  $d$  the molecule diameter. The mean thickness of the gas gap is given by:

$$\delta = 1.91 R_a \left( \frac{P}{H_c} \right)^{-0.097} \quad (\text{D.21})$$

If we assume atmospheric pressure and a temperature of  $23^\circ$  and use the average pressure calculated earlier we find  $Kn = 0.0075$ . This is for the area around the bolts. In the remaining areas there is also a gas gap conductance, we however assumed that the contact pressure there is neglectable. If we look at the equation for the free path of the molecules we see that the equation yields an infinite result if we take  $P = 0$ . Therefore we assumed that the pressure on the non bolted area is the pressure applied by the weight of the cool plate. If we calculate the Knudsen number for this pressure we find  $Kn = 0.0033$ . This means for both cases we can neglect  $g_1$  and  $g_2$ .

The gas gap conductance can now be calculated with:

$$h_g = \frac{k_g}{\delta} \quad (\text{D.22})$$

We find for the area around the bolts  $h_g = 3.35 \times 10^3 \text{ Wm}^{-2} \text{ K}^{-1}$  and for the remaining area  $h_g = 1.46 \times 10^3 \text{ Wm}^{-2} \text{ K}^{-1}$ .

# E

## MEASUREMENTS

### E.1. POWER DISSIPATION BEFORE POTTING

The power dissipation of the SSB before potting is particularly interesting as a reference measurement. Comparing it with the dissipation after potting can give an indication if the potting affects the performance of the SSB. It also is a validation that the SSB actually works before it is potted.

The power dissipation of component C2, Table A.1, depends on the temperature of the component. The direct relation is not known, therefore it was not implemented in the FEM model. The temperature dependency can be used to compare this measurement with the potted dissipation; by measuring the relation between temperature and power dissipation.

#### E.1.1. MEASUREMENT SETUP

To measure the power dissipation of the SSB the same measurement setup as discussed in chapter 3.1 is used. The power dissipation is measured via a power supply. The power supply displays the input voltage and the current drawn by the system. With the voltage and the current the power dissipation can be calculated by using the electrical power law:

$$P = VI \quad (\text{E.1})$$

Where  $V$  is the voltage and  $I$  is the current. Not all power is dissipated by the SSB, the resistors also dissipate power. To correct for this dissipation Ohm's law is used to calculate the power dissipated by the resistors:

$$P = \frac{V^2}{R} \quad (\text{E.2})$$

Where  $R$  is the resistance. We can now correct the total power by subtracting the power of the resistors:

$$P_{\text{ssb}} = P_{\text{total}} - P_{\text{resistors}} = V_{\text{total}}I - \frac{V_{\text{out1}}^2}{R_1} - \frac{V_{\text{out2}}^2}{R_2} - \frac{V_{\text{out3}}^2}{R_3} \quad (\text{E.3})$$

The resistances and the output voltages will be measured with a multimeter.

#### E.1.2. MEASUREMENT PROCEDURE

After the power is turned on, the current drawn by the SSB and the measured temperature is written down. When a temperature of 30 °C is reached, again the measured values are written down. After this for every 5 °C increase in temperature a measurement is done. This is repeated until a maximum temperature of 45 °C, which is 10 °C below the maximum allowed junction temperature. A 10 °C margin is taken because the thermocouple measures the outside temperature and not the junction temperature. The power dissipation is calculated by using equation E.3.

### E.1.3. RESULTS

The results are shown in Table E.1. For each 5 °C a 0.1A increase in current is seen. A power dissipation of approximately 14 W at 45 °C is found. The maximum dissipation was given as 16 W. This means that there is an offset of 2 W between the actual and the theoretical value. There is no temperature given for the 16 W, it may be that the 16 W is for a higher temperature. Also the components only have maximum dissipation in the worst manufacturing conditions. The chance that all components have this is rather slim.

Table E.1: The measurement results from the power dissipation test before potting. The temperature and the current are shown. For the temperature and power dissipation plot see Figure E.1.

| Temperature [°C] | Current [A] | V <sub>out1</sub> [V] | V <sub>out2</sub> [V] | V <sub>out3</sub> [V] | R <sub>1</sub> [Ω] | R <sub>2</sub> [Ω] | R <sub>3</sub> [Ω] |
|------------------|-------------|-----------------------|-----------------------|-----------------------|--------------------|--------------------|--------------------|
| 27.5             | 1.15        | 4.806                 | 7.985                 | 7.911                 | 6.8                | 10                 | 13.3               |
| 30               | 1.16        | 4.797                 | 7.975                 | 7.911                 | 6.8                | 10                 | 13.3               |
| 35               | 1.17        | 4.743                 | 7.925                 | 7.911                 | 6.8                | 10                 | 13.3               |
| 40               | 1.18        | 4.74                  | 7.905                 | 7.921                 | 6.8                | 10                 | 13.3               |
| 45               | 1.19        | 4.74                  | 7.885                 | 7.911                 | 6.8                | 10                 | 13.3               |

E

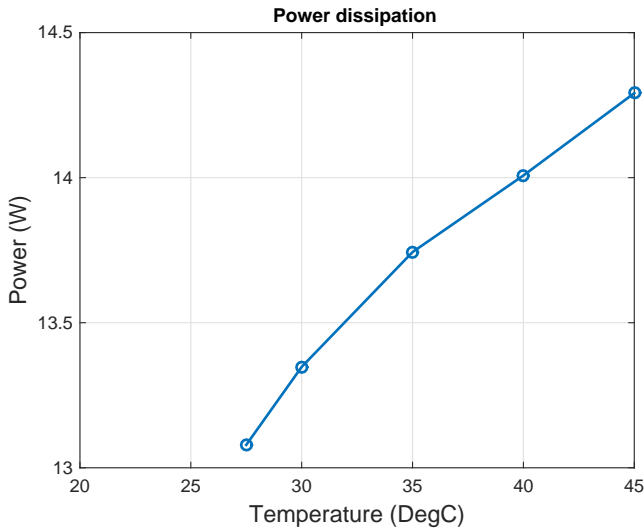


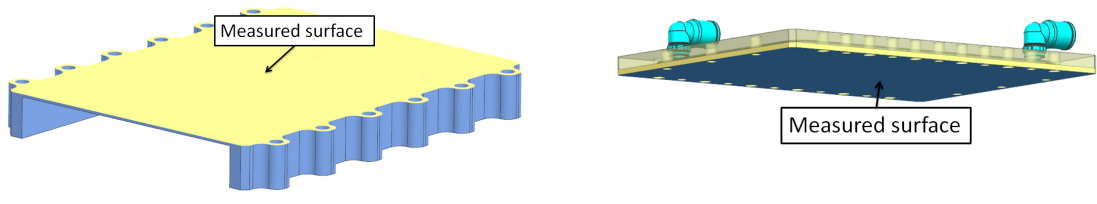
Figure E.1: The power dissipation of the SSB before potting against the temperature. The results show a linear relation of the dissipation and the temperature.

## E.2. SURFACE FLATNESS BEFORE POTTING

The second measurement is the surface flatness measurement, which is important for the thermal contact between the lean E-box and the cool plate. In the worst case, the surface will have a bowl like shape where the lowest point is in the middle. If this is the case there is no way to obtain contact in the middle of the surface without post machining or using a gap filler; the bolts can not provide pressure in the middle, only on the edges. This can be a reason for an offset between the test results and the FEM model. The measurements can be used to predict or exclude this potential offset.

A known property of the potting is that it will shrink while curing. The shrinkage of the potting can have a negative effect on the surface flatness. Therefore the flatness is measured before and after potting.

For the measurement before potting three surfaces are measured; both the top and bottom side of the lean E-box and the bottom side of the cool plate. See Figure E.2 for an illustration of the sides that will be measured.



(a) An illustration to show which side of the lean E-box housing is measured. The yellow side in the image is the surface that will be measured.

(b) An illustration to show which side of the cool plate is measured. The blue side in the image is the surface that will be measured.

Figure E.2: The sides that will be measured for the surface flatness measurement.

### E.2.1. MEASUREMENT SETUP

The surface flatness measurements will be done with the Mitutoyo Euro-C-A574, a Coordinate Measurement Machine. First a reference plane is created by measuring three points. The surface will then be measured by choosing certain measurement points in the xy-plane. At each point the z-coordinate is measured. The surface flatness is defined by the maximum height difference between the highest and lowest point seen from the reference plane.

The chosen measurement points will be 10 mm apart. This will create 10 points in x-direction and 13 in y-direction, which results in a total of 130 points.

### E.2.2. MEASUREMENT PROCEDURE

The measurements will be outsourced to the ASML modelshop. The modelshop personnel has the expertise to perform the measurements. They will provide a list with all the measurement points and a final value for the surface flatness.

### E.2.3. RESULTS

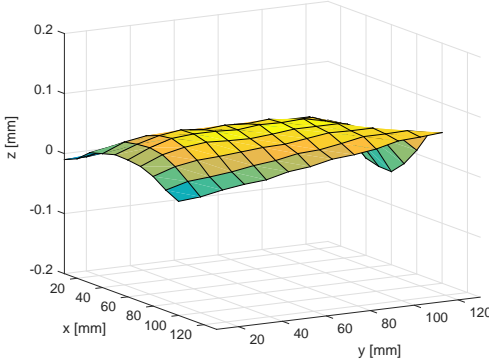
The surface flatnesses are shown in Table E.2 and the surface plots in Figure E.3. The plots give a good indication of what the surface looks like. For the housing the maximum height is seen in the middle. And the lowest point is seen on the far right. The far right resembles the open side of the housing, i.e. the side where the SSB is inserted in the housing. This shape is favorable for the lean E-box application; the bolt pressure will flatten out the surface.

The shape of the surface of the coolplate is shown in the lower part of the figure. The shape is somewhat similar to that of the lean E-box housing. The maximum is located in the middle of the surface. And a minimum in the bottom left corner. This, just like the housing surface, is a good shape for the application.

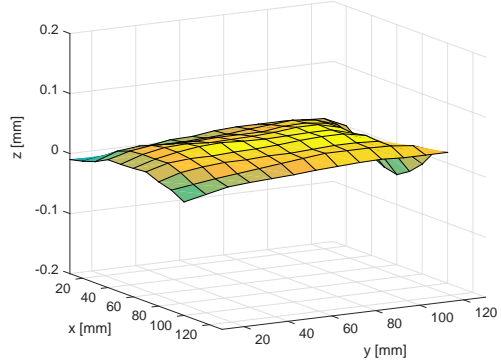
Table E.2: The surface flatness results from the flatness measurement.

| Surface              | Flatness          |
|----------------------|-------------------|
| Lean E-box housing 1 | 89 $\mu\text{m}$  |
| Lean E-box housing 2 | 106 $\mu\text{m}$ |
| Coolplate            | 124 $\mu\text{m}$ |

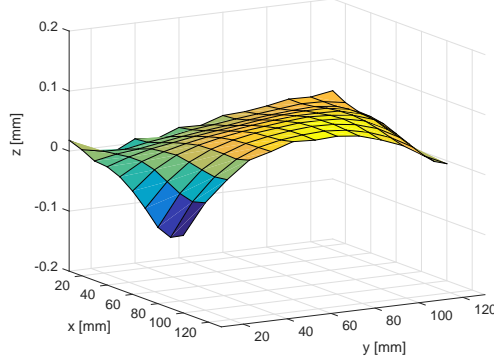
E



(a) The surface flatness of the first half of the housing.



(b) The surface flatness of the second half of the housing.



(c) The surface flatness of the cool plate.

Figure E.3: The results from the surface flatness measurement. The two plots on the top are the results from the lean E-box and the bottom is the result from the cool plate.

### E.3. POWER DISSIPATION AFTER POTTING

By measuring the power dissipation of the potted SSB, a first indication of the performance can be given. In theory the power dissipation should be the same before and after potting. The dissipation comparison is however not sufficient to draw a conclusion on the performance, the full functionality measurements must be done. No sufficient time is available to do these measurements. Therefore it is decided to only do the power dissipation measurements. If the power dissipations are the same it is an indication, but no conclusion, that the potting does not affect the electrical performance. If the results however show a major difference it is a good indication that the potting does. One reason for a performance reduction can be that due to the shrinkage of the potting components are damaged.

#### E.3.1. MEASUREMENT SETUP

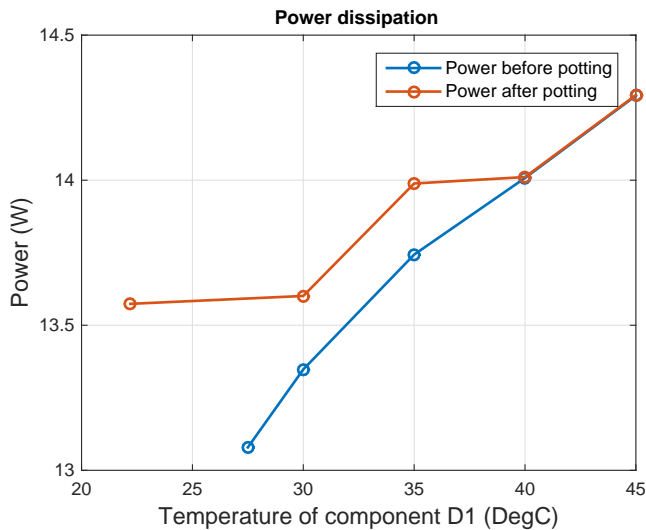
The same measurement setup is repeated as described in section E.1.1. Instead of just the SSB the complete potted lean E-box is plugged into the Q-tool.

### E.3.2. MEASUREMENT PROCEDURE

The exact same measurement procedure is repeated as described in section E.1.2.

### E.3.3. RESULTS

The results are shown in Figure E.4. The figure shows both the results of the potted and non-potted SSB. It is seen that for lower temperatures the dissipation of the potted SSB is slightly higher. But from 40 °C the two graphs are almost identical. The slight offset between the two graphs can be because of measurement errors. The results however look similar. This means that by looking at the power dissipation the conclusion can be made that the potting does not influence the electrical performance of the SSB. As mentioned before this is an indication and by no means a final conclusion on the performance.



E

Figure E.4: The measurement results of the power dissipation measurement. The blue line shows the power dissipation before potting and the red line shows the power dissipation after potting.

## E.4. SURFACE FLATNESS AFTER POTTING

The surface flatness measurement is repeated with the potted lean E-box. The result is compared with the surface flatness of the lean E-box before it is potted. This will give information about the effect of the potting shrinkage on the surface flatness.

### E.4.1. MEASUREMENT SETUP

The same measurement setup is repeated as mentioned in section E.2.1.

### E.4.2. MEASUREMENT PROCEDURE

The same procedure is repeated as mentioned in section E.2.2.

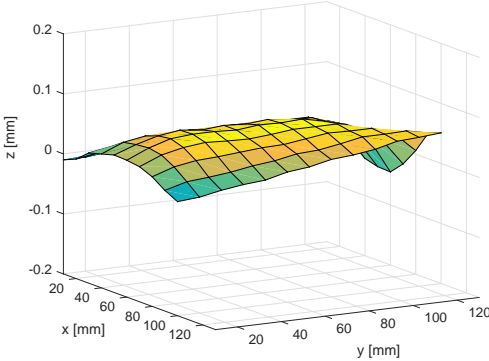
### E.4.3. RESULTS

The surface flatness of the potted lean E-box is 210 µm, which is about twice as much compared with the non-potted surface. In Figure E.5 both surfaces are shown, together with the difference between the two. The comparison between the two results shows that the influence of the potting is quite significant. In the middle of the potted surface a minimum is found, while in the non-potted case there is a maximum. In the potted case the maximum is in the back right corner. For the non-potted case that same corner is around the zero line. The minimum of the both surfaces is at the same location, however for the potted lean E-box it is about twice as low.

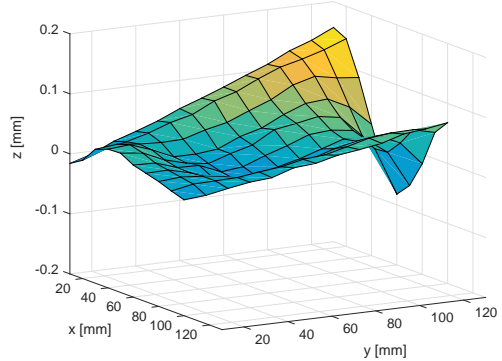
We can conclude that the potting has quite a large influence on the surface flatness of the lean E-box. The shape has become less favorable, however the coolplate still has a favorable surface, which will compensate

the less favorable surface to some extend. Because the temperature measurements are done in an atmospheric environment the surface will probably not result in large deviations from the FEM. If the measurements are however repeated in a vacuum the surface flatness becomes more important, a more detailed FEM model may be required.

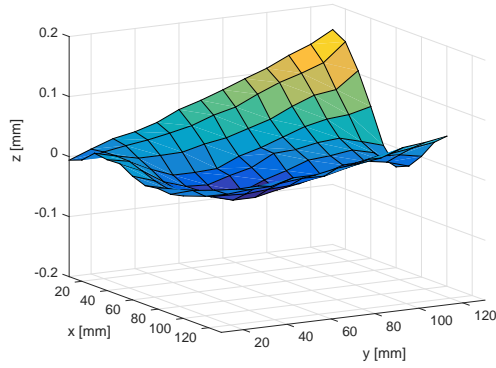
E



(a) The surface flatness of the first half of the housing before the lean E-box is potted.



(b) The surface flatness of the first half of the housing after the lean E-box is potted.



(c) The difference between the surface flatness before potting and after potting.

Figure E.5: The results of the surface flatness measurement. The top left image shows the surface of the non-potted housing and the top right image shows the surface of the potted housing. The bottom image is the difference between the two surfaces.

# F

## SENSITIVITY ANALYSIS

The sensitivity analysis is used to determine the change in  $\gamma$ . The derivative of the objective function with respect to the design variables is calculated. The derivative of the objective function determines the amount of change in  $\gamma$  per iteration.

Comsol uses the adjoint method to determine the sensitivities. The general form of the system of equations can be written in the form of a linear system of equations:

$$\mathbf{K}(\chi)\mathbf{u} - \mathbf{b}(\chi) = \mathbf{0} \quad (\text{F1})$$

First we differentiate with respect to  $\chi$ :

$$\frac{\partial}{\partial \chi}(\mathbf{K}(\chi)\mathbf{u} - \mathbf{b}(\chi)) = \mathbf{0} \quad (\text{F2})$$

If we expand the equation we end up with:

$$\frac{\partial \mathbf{K}(\chi)}{\partial \chi} \mathbf{u} + \mathbf{K}(\chi) \frac{\partial \mathbf{u}}{\partial \chi} = \frac{\partial \mathbf{b}(\chi)}{\partial \chi} \quad (\text{F3})$$

If we re-arrange for  $\frac{\partial \mathbf{u}}{\partial \chi}$  we find:

$$\frac{\partial \mathbf{u}}{\partial \chi} = \mathbf{K}^{-1}(\chi) \left( \frac{\partial \mathbf{b}(\chi)}{\partial \chi} - \frac{\partial \mathbf{K}(\chi)}{\partial \chi} \mathbf{u} \right) \quad (\text{F4})$$

For an arbitrary objective function  $f$  the derivative is found by:

$$\frac{\partial f}{\partial \chi} = \frac{\partial f}{\partial \mathbf{u}} \frac{\partial \mathbf{u}}{\partial \chi} \quad (\text{F5})$$



# G

## PDE FILTER

Filters in topology optimization remove the mesh dependency and the checkerboard problems that may occur. A density filter forces a certain radius around an element to have the same pseudo density. This removes the mesh dependency; for smaller meshes more elements fall within the preset radius. It also removes the checkerboard problem. For more on filters in topology optimization see the work of Sigmund [31].

The specific density filter that is implemented in Comsol is a partial differential equation (PDE) filter. More specific a Helmholtz-type PDE [6]:

$$-r^2 \nabla^2 \gamma_f + \gamma_f = \gamma \quad (\text{G.1})$$

With homogeneous Neumann boundary conditions:

$$\frac{\partial \gamma_f}{\partial n} = 0 \quad (\text{G.2})$$

Where  $r$  is the filter radius,  $\gamma_f$  is the filtered pseudo density and  $\gamma$  is the unfiltered pseudo density.



# H

## TOPOLOGY OPTIMIZATION OF THE VACUUM LOAD CASE

If the lean E-box concept were to be implemented in the lithography machine of ASML; the environment will be in a vacuum. The vacuum environment not only has an influence on the thermal performance, but also on the optimization results. The heat load of the lean E-box in vacuum is significantly different than the heat load of the lean E-box in an atmosphere. This has an impact on the results yielded by the optimization.

The topology optimization is also done for the vacuum heat load. For this optimization three inlet and outlet positions are considered; design  $D_2$ , design  $D_5$  and design  $D_8$ . Design  $D_2$  is chosen because it showed the best overall performance, design  $D_5$  is the design that is manufactured into a prototype and design  $D_8$  is chosen because of the shape of the heat load. The heat load shows almost no load in the middle of the area. Design  $D_8$  is chosen to see if the solver gives a result with only channels on the outside that go forward and back again over the design domain.

In Figure H.1 the optimized designs of the three design cases are shown. The results look rather different than the results of the atmospheric case; fewer smaller channels are formed and more emphasis is on the outside of the design domain. Which is exactly as expected when considering the distribution of the vacuum heat load.

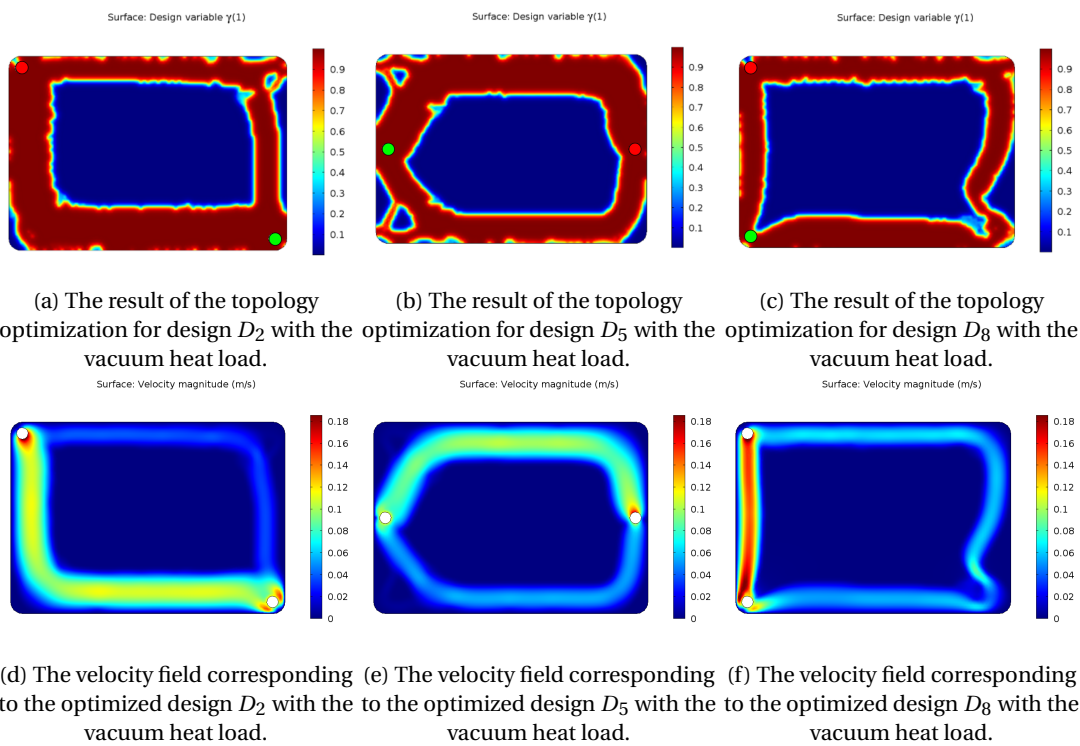


Figure H.1: The optimized results for the different design cases for the vacuum load case.